UNIVERSITÀ DEGLI STUDI DI TRENTO

Doctoral School in Civil, Environmental and Mechanical Engineering

Topic 1. Civil and Environmental Engineering

Giulia Rossi

Mechanics and numerical simulations of Dry Granular Flows driven by gravity

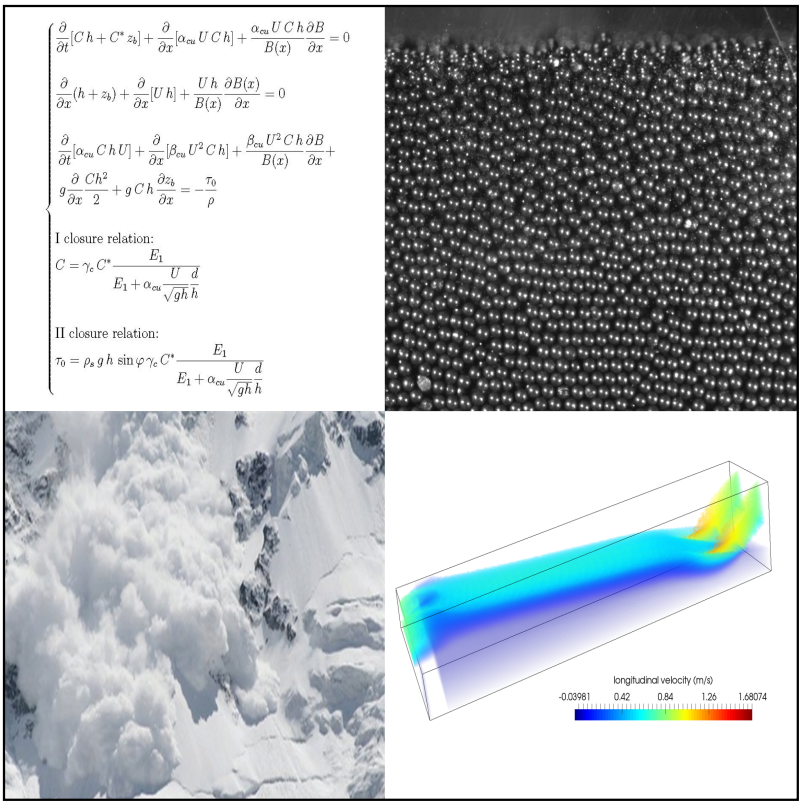

2017 - Doctoral thesis

The gravitational granular flows (e.g. debris flows or snow avalanches) are catastrophic and destructive phenomena affecting many areas in the world, and especially the mountain areas of Europe. Proper design criteria are required in order to improve protection structures and prevention strategies. Due to their complex nature, these phenomena present many aspects still unsolved in the research field.

This research addresses some aspects of the mechanics of dry granular flows: a 1D depth integrated model has been developed, based on a two phase approach. The system of equations consists of three partial differential equations, derived from the mass balances for the solid and fluid phase and from the momentum balance for the solid phase, and two rheological relations determined through experimental tests and particle numerical simulations.

The experimental investigation hes been conducted in a laboratory channel, by recording through high speed cameras the motion of polystyrene spherical particles. Within this research, it has been developed an ad hoc optical method to analyze and process the images recorded, with the aim of defining the main flow characteristics.

From a numerical point of view, a path conservative finite volume scheme has been adopted to solve the system of equations previously described: the numerical solution is compared to the experimental results for different configurations, in order to verify the effectiveness of the model.

Giulia Rossi, has a Master Degree in Civil Engineering at Politecnico di Torino and she has been PhD student (XXX cycle) at the University of Trento in Environmental Engineering.
The passion for mountains has lead her to occupy herself with avalanches and debris flows: after the Master Degree, she conducted a stage at "ARPA Piemonte" about avalanches risk management and statistical models to assess the snow height registered by "in situ" instrumentation in mountain areas. During the PhD period, her research was focused on environmental granular flows. The main topics tackled are the dynamic impact of debris flows against different types of structures (experimental investigations are carried out in order to develop rational design criteria) and the definition of a mathematical and numerical model for avalanches (two-phase approach: fluid and solid components).

UNIVERSITY OF TRENTO - Italy
Department of Civil, Environmental
and Mechanical Engineering

Doctoral School in Civil, Environmental and Mechanical Engineering
Topic 1. Civil and Environmental Engineering - XXX cycle 2015/2017

Doctoral Thesis - March 2017

Giulia Rossi

Mechanics and numerical simulations of Dry Granular Flows driven by gravity

Supervisors
Prof. Aronne Armanini - University of Trento
Prof. Michael Dumbser - University of Trento

Credits of the cover image: Giulia Rossi

University of Trento
Doctoral School in Civil, Environmental and Mechanical Engineering
http://web.unitn.it/en/dricam
Via Mesiano 77, I-38123 Trento
Tel. +39 0461 282670 / 2611 - *dicamphd@unitn.it*

Contents

List of Figures

Introduction

Granular materials are ensembles of discrete particles, whose behavior may be assimilated to a gas or liquid or to a solid, according as they are agitated or at rest. Their complex characteristics lead to classify granular media as a new form of material, which stands in between the solid, liquid and gas states (Jaeger et al., 1996).
Furthermore, flows of granular material involve many natural phenomena (e.g snow avalanches, rock avalanches, debris flows or pyroclastic flows) but also industrial applications (e.g. food or pharmaceutical industries). This wide presence of such type of flows in nature and industry, makes this topic of great interest for researchers. In particular, natural geophysical flows are among the most dangerous and destructive phenomena present in nature and in the last decades their frequency of occurrence has increased, making necessary a better prediction of these phenomena, in order to define a proper hazard mapping, defense strategies and protection measures..
Even in the industrial field a deeper knowledge of this topic is fundamental, in order to treat the material appropriately: it is still lacking a proper rheological frame and a 3D modeling of the phenomenon.

The thesis addresses some crucial aspects of dry granular flows, starting from the analysis of the theories usually applied to study this phenomena, passing through different experimental investigations and finally defining a 1D depth integrated mathematical model.
The granular flows have been studied since the '50s (Bagnold, 1954): subsequently the most innovative approach has been the application of the kinetic theory of gases adapted to the macroscopic case of granular material. This analogy between the dense gases and the granular flows has allowed the researchers to better understand the kinematic and dynamic peculiarities of this type of flow. Anyway, this approach is not able to exhaustively understand the granular flows, since some aspects can not be explained through this approach (e.g. frictional regime with prolonged contacts). We will deepen some hypothesis of the kinetic theory trying to understand the consequences on the conservation equations.

Since is still lacking a mathematical modeling able to reproduce all the motion characteristics, usually depth integrated models are applied. In this work a 1D depth integrated model will be derive to overcome some limitations of the existing model. In particular we consider the mobile bed condition, taking into account the bed erosion through the use of separate mass balance equation for the solid phase and the interstitial fluid. The system of equations needs two closure relations, derived from kinetic theory, that account for the frictional regime, through a modulating function f_0 that allows the coexistence of the two regimes. Then the relations will be calibrated through the experimental investigation and through some molecular dynamics simulations.
The experimental data are analyzed by a new optical method, developed within the thesis, in order to have accurate enough measurements of the flow features (e.g concentration and velocity profiles). The method is based on the binarization of the images recorded during the experiments: through the binarization the particles are individuated and the concentration may be computed. Regarding the velocity, the optical flow approach is used, by adopting the good features to track method.
Finally, a numerical solution based on a path conservative finite volume scheme is presented: the numerical results will be compared to the experimental data, showing a quite good agreement.

Chapter 1

Mechanics of granular flows: state of the art

Granular flows are ensembles of many solid particles, whose interstices are occupied by a fluid (water or air). They may be recognized in nature as gravitational granular flows (e.g. debris flows, snow avalanches or rock avalanches), but are often involved in industrial processes too (e.g. pharmaceutical field or food industries).
The mechanics of granular flows is a quite recent research topic. Granular flows are two phase systems; they are an ensemble of solid particles and a fluid (water or air). For this reason they behave both like a solid and like a fluid: one of the main characteristics of a dry granular material is the angle of repose. If the material is posed on a surface inclined less than this angle, the granular phase is at rest as a solid body, while when the angle increases the material flows like a liquid (Jaeger et al., 1996). Therefore, the transition between the fluid and solid behaviors may correspond to the transition between rapid flows and quasi-static flows (Campbell, 1990).
An other important parameter of a granular material is the concentration, that is the ratio between the grains volume and the bulk volume: there is a critical value called *packing fraction*, which corresponds to all the particles are at rest. The initial packing fraction and the local concentration influence the motion of the granular flow, in particular the flow rate (Aguirre et al., 2014).
The local concentration may vary because of the formation of stress chains (Lois et al., 2006; Dantu, 1968), which are a peculiar aspect of the granular material. Due to these force chains, the material becomes more rigid and stiff: this effect is called *jamming*. One of the more evident examples is the formation of arches at the opening of a hopper

filled with granular material, depending on the hopper angle (To et al., 2001). The particles forming the granular material tend to form arches and to propagate the forces to the sidewall, while at the arches center the pressure assumes a minimum value. This was shown through many experimental investigation (Vanel et al., 1999; Brockbank et al., 1997). Furthermore, the non-uniformity of the particles size is a very crucial aspect: in the industrial application one of the main problems is the segregation effect, due to the presence of particles of many different sizes. Many author tackled the problem, considering binary mixtures (Jenkins and Mancini, 1987; Shen, 1984) and for distributions of particle sizes (Shen and Hopkins, 1988), but the segregation effect is a still open issue. The before mentioned aspects are only some of the main features of the granular flows: they are very complex phenomena and the study of their mechanics and dynamics is still open. They are characterized by different motion regimes, linked to the concentration of the granular material and the type of contact among particles. In the following, the different regimes will be desbribed accurately and the main theories developed in the past years will be presented.

1.1 Collisional regime

The collisional regime occurs at low concentration (usually < 0.3) and for this reason its behavior is characterized by instantaneous and binary collisions among particles and high deformation rates. It is a *gas-like* behavior: the grains are dispersed in the fluid (air or water) and each particle moves almost independently from the others. The only interactions among particles are instantaneous collisions.

1.1.1 Bagnold's theory

Bagnold (Bagnold, 1954) conduced the first study regarding the granular flows: he used a cylindrical rheometer to observe the behavior of dispersed spherical particles in Newtonian fluids of varying viscosity. The grains density was balanced with respect to the fluid density, in order to have no differential forces due to radial acceleration (difference of densities $<< 0.001$). It is worth noting that, for this reason, the gravity is not present in his experiments: they describe the interaction between the particles, but not the real mechanics of a granular flow driven by gravity. He defined a *linear concentration* λ:

$$\lambda = d/s \tag{1.1.1}$$

where d is the particles diameter and s the mean distance between the adjacent particles. He supposed that different behaviors took place for different values of λ.
The central concept was the **dispersive pressure** generated by the contact forces between particles during collisions: different layers of particles move at different velocities. According to the difference of velocity between two adjacent layers and to the value of the linear concentration, a certain pressure between the grains of the two layers should exist:

$$p^g = \alpha_i \rho_s \cos\alpha_i \lambda f(\lambda) \left(\frac{dU}{dy}\right)^2 d^2 \tag{1.1.2}$$

where α_i is the angle of inclination between the grains during the collision, ρ_s the grain density, $\dfrac{dU}{dy}$ the velocity gradient. The tangential stresses are then proportional to the normal stresses through a Coulombian relation, based on the friction angle of the material.
The results of his experiments underlined the presence of two regions: the *grain-inertia region* and the *macro-viscous region*.
The first one is characterized by high speeds, and both the tangential stresses τ and the normal stresses p become proportional to $\left(\dfrac{dU}{dy}\right)^2$; furthermore, for $\lambda < 12$ the ratio between τ and p assumes a constant value (that means it does not depend on the concentration), while for $\lambda > 12$ the ratio depends on λ. The grain inertia regime correspond to the collisional regime.
At lower speeds the collisions are prolonged, and we are in the second regime: both τ and p become proportional to $\dfrac{dU}{dy}$.
Bagnold in order to relate the two regimes, defined a dimensionless number, then called "Bagnold number", which is the ratio between the inertia stress and the viscous stress:

$$Ba = \frac{\lambda^2 \rho_s d^2 \left(\frac{dU}{dy}\right)^2}{\lambda^{\frac{3}{2}} \eta \left(\frac{dU}{dy}\right)} \tag{1.1.3}$$

For value of $Ba > 450$, the collisional regime is predominant, for value of $Ba < 40$ the macro-viscous behavior is predominant and in between there are transitional regimes.
The Bagnold's theory has two main limitations:

1. it hasn't a *state equation* for the granular phase;

2. for high speed and $\lambda > 12$, the ratio between τ and p is constant; that is that in a uniform channel flow the concentration must be constant in the case of mixtures of water and sediments (Armanini, 2015), and this is not ever realistic. In the case of dry granular flows, the concentration is undetermined; this does not imply that it is constant.

1.1.2 Kinetic theories

Kinetic theories were developed in order to overcome the limitations of Bagnold's theory. The basal concept is the analogy of granular flows with gases: the particles are assimilates to molecules of a gas and the pressure rises from the collisions among particle as in gases rises from collisions among molecules (Jenkins and Savage, 1983).
The kinetic theory have been developed under the following hypotheses:

- spherical particles;
- monodisperse system;
- frictionless particles;
- constant coefficient of restitution;
- instantaneous collisions;
- binary collisions;
- molecular chaos and isotropy

The analogy with the thermodynamic temperature in a gas at a molecular level, is represented by the kinetic energy associated to the translational velocity fluctuations of the granular particles: the particle velocity fluctuation is defined as $u' = u - U$, where u is the instantaneous velocity and U the mean transport velocity (that is the ensemble average: $U =< u >$). The representative parameter of this concept is the *granular temperature*, associated to the particle velocity fluctuation $T =< u'^2 > /3$, such that $3T/2$ is the specific kinetic energy of the translational velocity fluctuations.
The relevant information in this approach are not the position and velocity of the particles at each time, but the ***distribution function***, that is what percentage of the particles is in a certain part of the container and what percentage has velocities within a certain range at each instant. The single-particle velocity distribution function depends on the position

r and the instantaneous velocity u. Usually it is assumed a Maxwellian distribution:

$$f^{(1)}(\mathbf{r},\mathbf{u},t) = \frac{n}{(2\pi T)^{\frac{3}{2}}} exp\left(-\frac{(\mathbf{u}- < \mathbf{u'} >)^2}{2T}\right) \tag{1.1.4}$$

where T is the ***granular temperature***.
In particular the ***ensemble average*** of any single-particle property ψ is:

$$< \psi >= \frac{1}{n}\int_{-\infty}^{+\infty} \psi f^{(1)}(\mathbf{r},\mathbf{u},t)d\mathbf{u} \tag{1.1.5}$$

where n is the number of particles.
However the particles interact with each other, then it is important to define a ***pair distribution function***, which is the probability to find a pair of particles within the range of positions r_1 and $r_1+\delta r_1$, r_2 and $r_2+\delta r_2$, with velocities within the range u_1 and $u_1+\delta u_1$, u_2 and $u_2+\delta u_2$.

$$f^{(2)}(\mathbf{u}_1,\mathbf{r}_1;\mathbf{u}_2,\mathbf{r}_2;t) = g(\mathbf{r}_1,\mathbf{r}_2)f^{(1)}(\mathbf{r}_1,\mathbf{u}_1,t)f^{(1)}(\mathbf{r}_2,\mathbf{u}_2,t) \tag{1.1.6}$$

where the first term on the right side is the "*normalized* pair distribution function"; it's the spatial arrangement of the pairs of particles.
The next fundamental step is to define the conservation equations: the kinetic theories are based on the *Boltzmann equation*. It's general formulation is the following:

$$\frac{\partial f}{\partial t} + \frac{\partial \mathbf{r}}{\partial t}\frac{\partial f}{\partial \mathbf{r}} + \frac{\partial \mathbf{u}}{\partial t}\frac{\partial f}{\partial \mathbf{u}} = \frac{\partial f}{\partial t} + \mathbf{u}\frac{\partial f}{\partial \mathbf{r}} + \frac{\mathbf{F}}{m}\frac{\partial f}{\partial \mathbf{u}} = 0 \tag{1.1.7}$$

However this equation means that the particle density remain constant (the variation of the distribution function is zero): but since there are collisions, they are discontinuities, the trajectories are not continuous and the distribution function varies. For this reason we have to add a further term which considers the collisional forces; so we obtain the following form:

$$\frac{\partial f}{\partial t} + \mathbf{u}\frac{\partial f}{\partial \mathbf{r}} + \frac{\mathbf{F}}{m}\frac{\partial f}{\partial \mathbf{u}} = \left(\frac{\partial f}{\partial t}\right)_{coll} \tag{1.1.8}$$

Equation (1.1.8) is the *collisional Boltzmann equation*.
Afterwards, by substituting the mass m, the momentum mc and the kinetic energy $\frac{1}{2}m\mathbf{u}^2$ to the general property ψ in the Enskog's equation of change (derived by the boltzman equation multiplying by the propereti Ψ and integrating on all the velocity (Reif, 1965))results to be:

$$\frac{\partial}{\partial t}(n < \Psi >) + \frac{\partial}{\partial \mathbf{r}}(n < \mathbf{u}\Psi >) - n\left(\frac{D\Psi}{Dt}\right) = \Phi_c \tag{1.1.9}$$

where

$$\phi_c = -\nabla\Theta + \chi \tag{1.1.10}$$

and Θ is the collisional transfer contribution and χ is the "source-like" collisional contribution, we can obtain the usual hydrodynamic equations (Huang, 1928):

- $\psi = m$

$$\frac{d\rho}{dt} = -\rho\nabla\cdot\mathbf{u} \tag{1.1.11}$$

- $\psi = mc$

$$\rho\frac{d\mathbf{u}}{dt} = \rho\mathbf{F} - \nabla\cdot\mathbf{p} \tag{1.1.12}$$

- $\psi = \frac{1}{2}mc^2$

$$\frac{3}{2}\rho\frac{dT}{dt} = -\mathbf{p} : \nabla\mathbf{u} - \nabla\cdot\mathbf{q} - \gamma \tag{1.1.13}$$

In particular **F** are the body forces per unit mass, **p** is the stress tensor, **q** the flux of fluctuation energy and $\gamma = \chi\left(\frac{1}{2}mu^2\right)$ is the collisional rate of dissipation per unit volume.
Both the stress tensor and the flux of fluctuation energy are made up of two contributions: the kinetic part (due to the fluctuation velocity) and the collisional part (due to collisions among particles), as is shown in equations (1.1.14) and (1.1.15).

$$\mathbf{p} = \rho < (\mathbf{u}-\mathbf{U})^2 > +\Theta m(\mathbf{u}-\mathbf{U}) \tag{1.1.14}$$

$$\mathbf{q} = \frac{1}{2}\rho < (\mathbf{u}-\mathbf{U})^3 > \Theta\left(\frac{1}{2}m(\mathbf{u}-\mathbf{U})^2\right) \tag{1.1.15}$$

where U is the averaged velocity.
Enskog (Chapman and Cowling, 1970) managed to extend these formulations to dense granular flows (concentration up to 0.4). He introduced a *pair correlation function* in the two-particle distribution function, in order to increase the collision frequency though a parameter that takes into account the spatial correlations. It does not mean that multiple contacts or long lasting contact are considered, only the collision rate is increased. In the literature, many expression for g_0 have been developed. In the following we consider one of the most diffused, due to Lun & Savage (Lun and Savage, 1986):

$$g_0 = \frac{1}{\left(1-\frac{C}{C^*}\right)^{2.5C^*}} \tag{1.1.16}$$

where C is the concentration of the granular media and C^* the packing fraction.
Another important parameter introduced to apply the kinetic theories of gases to granular flows is the coefficient of restitution e_n. the collisions among particles are no more perfectly elastic, as it was for molecules. If we consider the velocities of two particles before a collision ($\mathbf{u}_1^{post}$ and $\mathbf{u}_2^{post}$) and after the collision ($\mathbf{u}_1^{pre}$ and $\mathbf{u}_2^{pre}$), the collision is described by the following relation:

$$(\mathbf{u}_1^{post} - \mathbf{u}_2^{post}) \cdot \mathbf{n} = -e_n(\mathbf{u}_1^{pre} - \mathbf{u}_2^{pre}) \cdot \mathbf{n} \tag{1.1.17}$$

where e_n is the coefficient of restitution and **n** the unit vector orientated from the center of particle 1 to the center of particle 2. This relation is contained in the computation of the collisional term in Eq. (1.1.10).
These are the basis of all kinetic theories; then the many existing approaches (Jenkins and Richman, 1986; Lun et al., 1984; Savage and Jeffrey, 1981; Jenkins and Hanes, 1998) differ in the form of the distribution function or usually in the *constitutive relations*, that make **p**, **q** and γ depend on other properties like ∇u, ρ, T and all the parameters of the system.
The assumptions on which the kinetic theory have been developed are quite strictly, so that the theory is no more valid for higher concentration or in presence of different types of interaction among particles, such as prolonged contacts due for example to a lower coefficient of restitution. For this reason, some authors developed extended kinetic theories for *dense* granular flow (Lun and Savage, 1987; Jenkins, 2007).

1.2 Frictional regime

The second type of regime existing in granular flow dynamics is the frictional regime: it is characterized by long lasting contact among particles and collisions among more than two particles. It occurs for higher concentrations near the packing value (> 0.4), where the shear rates are very low.
In this regimes, forces are transmitted through chains of grains, among which dominate normal stresses and tangential stresses due to the friction.
Therefore, this regimes takes place in the lower part of a free surface flow, where the concentration is higher (Armanini et al., 2005). Anyway, Armanini et al. (2009) experimentally observed that the regime prevails at lower distance from the bed, but coexist with the collisional regime. In particular, there is an *intermittency* between the two.

There are many models (Savage and Hutter, 1989; Pudasaini, 2012; Pitman and Le, 2005b) intended to represent this regime in literature. Usually they are based on soil mechanics (visco-plasticity theories) or on the assumption of a Coulombian scheme (shear independent behavior, which does not take into account the collisional and kinetic nature of the solid phase). The dynamics of granular media is simply analyzed as a series of sliding layers, among which a friction force develops (Roux and Radjai, 1998).

1.3 Intermediate regime

In the reality, granular media presents both the frictional and the collisional regime. We may say that they are characterized by an *intermediate* regime, in which granular material flows like a liquid and there is not a sharp distinction between the two mechanisms of motion.
Savage (Savage, 1984) tried to take into account both the regimes, considering in the constitutive relations a rate dependent and a rate independent contributions. He combines the Coulmbian frictional regime with the kinetic theories. Also Aranson and Tsimring (Aranson and Tsimring, 2002) tried to reproduce the two regimes, introducing a parameter function of the order of particles.
However these methods are valid if there is a sharp distinction between the two regimes, and do not represent their intermittency.

1.3.1 MiDi model

One recent approach to represent the intermediate regime of dense granular flows is the μ(I) model (Ancey and Evesque, 2000; Jop et al., 2006). Their study is based on a dimensionless parameter I, called *Inertial number*:

$$I = \frac{\dot{\gamma}\, d}{\sqrt{P/\rho_s}} \tag{1.3.1}$$

where $\dot{\gamma}$ is the shear rate, d the particle diameter, P the confining pressure. This parameter, which is often referred to as the square root of the Savage number, represents the ratio between a macroscopic deformation scale ($1/\dot{\gamma}$) and an inertial time scale ($\sqrt{d^2\rho_s/P}$).
Considering that:

$$\tau = \mu(I)\, P \tag{1.3.2}$$

the coefficient $\mu(I)$ has been determined by several different experimental analysis (MiDi, 2004). The shape of this factor is the following:

$$\mu(I) = \mu_s + \frac{\mu_2 - \mu_s}{I_0/I + 1} \tag{1.3.3}$$

where μ_s and μ_2 are the tangent respectively of the static angle and the dynamic angle characterizing the flow; I_0 is a constant. This equation implies that the friction angle varies during the motion, between the quasi-static regime ($I \rightarrow 0$, $\mu(I) = \mu_S$) and the kinetic regime ($I >> I_0$, $\mu(I) = \mu_2$).
According to this rheology, the granular media starts to flow only if:

$$|\tau| > \mu_s P, \text{where} \quad |\tau| = \sqrt{\frac{1}{2}\tau_{ij}\tau_{ij}} \tag{1.3.4}$$

So that the yield criterion is similar to the Drucker-Prager criterion. It is worth to notice that, in this way, the granular media is studied as a visco-plastic fluid.
This approach has been widely applied for its simplicity to many applications.
Anyway, there are some aspects that may this model that limit its applicability in some cases. First of all, one of the main assumption behind the $\mu(I)$ rheology, is a negligible variation of the solid volume fraction (Jop et al., 2006). For this reason, this model could not be applied where the collisional regime is predominant and the fluctuation of the concentration is not negligible.Jop (2008) consider a linear variation of the volume fraction, but this solution is applicable only in a frictional regime .
Additionally, when fast collisions occurs, they lead to a rate-dependent wall stress and the Coulombian friction between the wall and the particles adopted by the model is no more valid.
Furthermore, the model fails to predict accurately the velocity profiles for shallow flows or flows influenced by boundaries, since it has been developed considering the flow uniform across the channel (Jop et al., 2006). Besides, the local rate-dependent friction law needs the introduction of an additional length scale, in order to take into account non-local effects.
Finally, it is worth to notice that the model is based on the assumption of two constant angles (static and dynamic). Regarding the dynamic angle, in a collisional regime it is not a constant as assumed in the model but is a characteristic depending on the flow conditions and not a material property.

1.3.2 Heuristic model

Another model, based on the Savage number I_s, is that proposed by Armanini et al. (2014). They consider the Savage number as the ratio between the shear independent stresses and the shear dependent ones. This model assumes the coexistence and intermittency of the collisional and frictional regime. The first is reproduced by kinetic theories, while the second through a specific formulation as follows:

$$\tau^{fric} = p^g \Phi^{fric} \frac{I_{s0}}{I_s + I_{s0}} \tag{1.3.5}$$

where p^g is the granular pressure, Φ^{fric} in the friction angle of the material and I_{s0} is a parameter depending on the material properties. Regarding the pressure frictional component, it reads:

$$p^{fric} = p^g \frac{I_{s0}}{I_s + I_{s0}} \tag{1.3.6}$$

where p^{fric} is assumed to be the difference between the total pressure p^g and the collisional component p^{coll}. Definitly, the collisional pressure is derived as follows:

$$p^{coll} = p^g - p^{fric} \tag{1.3.7}$$

This model has been validated for two-phase flows with water as interstitial fluid and permanent and uniform flow conditions.

Chapter 2

Observations on the application of kinetic theories to granular flows

Kinetic theories are based on the *Boltzmann equation*, which expresses the conservation laws for the properties of the flow. This equation is based on the average done over all the particles of the control volume. It is worth to notice that some hypothesis behind the kinetic theories do not hold for the granular case: *i)* the dimension of the particles are comparable to that of the control volume, so that the strong scale separation is lost, *ii)* the system is not ergodic as for gases (see Section 2.1), and the averaging process becomes crucial.
Contrary to gases, in granular flows, where the grain size is comparable to the dimension of the control volume, the velocity and the concentration of particles could be correlated, so that the averaged product of their fluctuating components in some cases would not be zero.

2.1 Scale separation and ergodicity

One of the fundamental hypothesis behind the kinetic theories is that the control volume analyzed is taken large enough to contain a very high number of particles (n $\rightarrow \infty$), but small enough so that compared to the macroscopic dimensions it may be considered a point (Huang, 1928). This implies a strong scale separation: the molecules are of an infinitesimal size, so that the scale associated to their mean free path is very much smaller than the scale at which gradients of physical properties occur. If we consider a gradient of the temperature in a gas, even if it is quite large as 200 K/cm, the difference of temperature between two adjacent

molecules is negligible (Goldhirsch, 2008). This is a very clear example of the strong scale separation, which implies that a *macroscopic* gradient does not influence what characterizes the *micro-scale*.
The choice of a control volume that respects these hypotheses is clearly not possible in granular flows, since the grain size scale is similar to that of the gradients. The dimension of the control volume becomes comparable to that of the particles and a sharp distinction between the micro- and macro-scale is not applicable.
One of the consequences of this aspect, is that the system is not ergodic, as it is for gases (Jaeger et al., 1996). The ergodicity property means that the average of a process variable made over time, over space and over the whole statistical ensemble coincides. Due to the lack of strong scale separation, the number of particles in the control volume is not so high to be considered constant, since a few particles may change significantly the concentration. This aspect and the presence of gradients at the particles size may differentiate the average, according as it is done over time, space or statistical ensemble. For this reason, the ergodicity, applicable in the case of gases, is no more a certain property in granular flows.

2.1.1 Main scales governing the phenomenon

In granular flows, we may consider the presence of different scales. The smallest length scale is that proportional to the particles diameter; it is currently analyzed through the Boltzmann equations, adopting the ensemble average and considering the particles small enough so that the control volume contains an infinite number of them. This approach is derived from the kinetic theories Jenkins and Savage (1983); Jenkins and Richman (1985); Lun (1991).
However, while for gases this is a realistic hypothesis, for granular flows, where the particles have a dimension comparable to that of the control volume, this scale turns into an intermediate scale. In fact, the hypotheses behind the Boltzmann procedure are no more true and the scale at which we need to average is greater than the microscopic level, but smaller than the scale related to the external boundaries. For this reason, we may expect that the process can be studied considering an intermediate scale, but the two scales most often are not easily separable.
In the following section, we analyze the consequences of this lack of scale separation.

2.1.2 Implications of the scale separation on the kinetic theories equations

Analyzing the definition of the number density (which represents the volume fraction concentration), we can say that $n = f(\mathbf{r}, t)$ (where *r* indicates the vector of the position), i.e. it doesn't depend on the velocity because by definition it is the integral over all the velocities of the distribution function:

$$n(\mathbf{r}, t) = \int f^{(1)}(\mathbf{r}, \mathbf{u}, t) d\mathbf{u} \tag{2.1.1}$$

Since the *ensemble average* of a general property of the granular gas is defined as follows:

$$< \psi >= \frac{1}{n} \int \psi f^{(1)}(\mathbf{r}, \mathbf{u}, t) d\mathbf{u} \tag{2.1.2}$$

we can conclude that if we have an ensemble average of a property multiplied by n, this one could be considered as a constant in the integral and so we obtain that:

$$\begin{aligned} < n\psi > &= \frac{1}{n} \int n\psi f^{(1)}(\mathbf{r}, \mathbf{u}, t) d\mathbf{u} = \\ &= \frac{n}{n} \int \psi f^{(1)}(\mathbf{r}, \mathbf{u}, t) d\mathbf{u} = \\ &= \int \psi f^{(1)}(\mathbf{r}, \mathbf{u}, t) d\mathbf{u} = n < \psi > \end{aligned} \tag{2.1.3}$$

This means that the ensemble average of the product of a property and the number density *n* is the same as the number density multiplied by the ensemble average of the property alone. Indeed, since n doesn't depend on **u**, it can be brought out of the integral.
In particular, equations (2.1.1), (2.1.2) and (2.1.3) are correct only in case of a strong scale separation, in which the concentration, represented by n, could be considered constant in more realizations; on the contrary in granular flows, this procedure is applicable only to a *single realization*, as pointed out by Goldhirsh (Goldhirsch, 2003). As outlined previously, the central concept is that granular flows are not *ergodic systems*, as the gases are, for the following reasons:

- In gases the number density n could be considered constant, since the number of particles tends to infinity and the concentration is not affected significantly by one particle more or less. On the contrary in granular flows, where we have a control volume whose dimensions are comparable to that of particles, one particle more or less may change significantly the value of n.

- The presence of gradients at the same scale of particles collisions may cause a non-homogeneous flow along the vertical axis (contrary to the longitudinal axis) so that one realization could be not representative of the whole process, regarding the vertical direction.

Following these arguments, we may say that the kinetic theories average process, based on the ensemble average, could be applied in first approximation to a single realization in granular flows field.
With *single realization* we refer to a small part of the measurement of the flow characteristics, corresponding to a time period small enough, so that the hypothesis of the kinetic theories can be considered applicable. In a single realization, the number density *n* is assumed to be constant and the two types of average still coincide with each other.

2.2 Averaging processes

From all the above considerations, it becomes clear the fundamental role of the averaging process. The approach adopted by the kinetic theories is statistical and a different way to compute the mean values of the variables may lead to important changes in the final system of equations. In this section, the types of average that could be applied are analyzed, trying to indicate the most appropriate for a granular flow composed by relatively large particles.

2.2.1 Phasic average and mass-weighted average in a single realization

In the literature two main types of average are mentioned as useful for the two-phase mechanics (Drew, 1983): the *phasic average* and the *mass-weighted average*, called *Favre average* (Favre, 1965).
The first is defined as follows:

$$\widetilde{\psi}^{(\beta)} = \frac{< X^{(\beta)}\psi >}{< X^{(\beta)} >} \tag{2.2.1}$$

where the brackets $<>$ indicates a general averaging process (over time, space or ensemble), β indicates the phase and ψ is a general variable of the process.
$X^{(\beta)}$ is the phase function, which is defined as:

$$X^{(\beta)}(\mathbf{x}, t) = \begin{cases} 1 & \textit{if } \mathbf{x} \textit{ is in phase } \beta \textit{ at time } t \\ 0 & \textit{otherwise} \end{cases} \tag{2.2.2}$$

The second type of average, called *mass-weighted average*, looks as follows:

$$\widehat{\psi}^{(\beta)} = \frac{< X^{(\beta)} \rho^{(\beta)} \psi >}{< X^{(\beta)} \, \rho^{(\beta)} >} \tag{2.2.3}$$

In this case, as suggested by the definition, the average of the variable ψ is weighted according to the density $\rho^{(\beta)}$ of the phase.

If we now consider the generic average $<>$ to be the ensemble average, done over the whole statistical ensemble of particles of a single realization as in the kinetic theories, we obtain two different results according to the methods previously mentioned.
Being N_p the number of particles of the realization, by applying the phasic average, we obtain the following form:

$$\widetilde{\psi} = \frac{1}{N_p} \sum_{1}^{N_p} \psi^{(i)} \tag{2.2.4}$$

where i is the i-th particle of the realization. In particular, if we consider the velocity $\mathbf{u}$ and the concentration c of the solid phase, we obtain:

$$\widetilde{\mathbf{u}} = \frac{1}{N_p} \sum_{i=1}^{N_p} \mathbf{u}^{(i)} \tag{2.2.5}$$

$$\widetilde{c} = \frac{1}{N_p} \sum_{i=1}^{N_p} c^{(i)} \tag{2.2.6}$$

Equation (2.2.5) is the phasic-ensemble average of the velocity and equation (2.2.6) is the phasic-ensemble average of the concentration.
Regarding the *Favre or mass-weighted average*, and still considering the ensemble average, we may write it as follows:

$$\widehat{\psi}^{(k)} = \frac{1}{N_p} \frac{\sum_{i=1}^{N_p} \rho \psi^{(i)}}{\widehat{\rho}} \tag{2.2.7}$$

where i the i-th particle and ρ represents the density of the granular phase, which, in term of concentration, is $\rho = c \, \rho_s$ with ρ_s the density of the particles, which is assumed constant. By considering again the velocity and the concentration, we obtain the following relation for the mass-averaged velocity:

$$\widehat{\mathbf{u}} = \frac{1}{N_p} \frac{\sum_{1}^{N_p} c^{(i)} \mathbf{u}^{(i)}}{\widetilde{c}} \tag{2.2.8}$$

where, obviously, $\widetilde{c} = \widehat{c}$.

For homogeneous fluid (like pure water), the final averaged values coincide; in the kinetic theories, the assumption of very small size of the particles and a constant concentration (number density *n*) make the two averages still coincident. However, for granular flows, these two assumptions are no more valid and the two averages may lead to different results.

2.2.2 Averaging process in case of more that one realization (longer time)

In cases in which the process is characterized by more than one realization, we need a further averaging procedure. Let us assume, by now, a phasic-average to define the average of a property in more than one realization:

$$\overline{\psi} = \frac{1}{R} \sum_{1}^{R} \widetilde{\psi}^{(k)} \tag{2.2.9}$$

where $\overline{\psi}$ is the phasic-average of a general property over all the realizations, $\widetilde{\psi}^{(k)}$ is the phasic-ensemble average of the single $k-th$ realization and R is the number of realizations on which we average.
We want to underline that in making these averages, we assume that the fluctuations with respect to the mean values of the single realization are governed by collisional mechanisms, related to the kinetic theories. On the other hand, in the case of several realizations, the fluctuations are related to macroscopic scales too (like the flow depth or the mean velocity of the flow).

2.3 Influence on the continuity equation

In the usual application of kinetic theories to granular flows, there is no distinction between a single realization and more than one realization: the ensemble average is applied assuming the same Boltzmann hypothesis of ergodicity of the system.
Starting from the above considerations, the effect of the averaging processes introduced in the previous sections, should be inserted into the mass, momentum and energy conservation equations.
However, by now, we want to focus our attention on the mass conservation equation, since it is rather simple, and allows us to check the validity of our considerations.

The mass conservation equation for a dry granular flow, that is derivable from the kinetic theories is written as in the following (Jenkins and

Savage, 1983; Jenkins and Richman, 1985):

$$\frac{\partial < nm >}{\partial t} + \frac{\partial < nmu_i >}{\partial x_i} = 0 \tag{2.3.1}$$

where n is the number density, m the mass of the single particle, $i = 1, 2, 3$ indicates the three coordinates.
Notice that we can write the equality $\rho^g = m_g c = n\, V_p\, m_g$, where ρ^g is the density referred to the granular phase, m_g is the mass of the granular particles, V_p the particle volume and c is the particles concentration. In the following we use $\rho^g = c\, \rho_s$ (V_p is constant, we may delete it from the equation), to be coherent with the fluid mechanics notation. Then, since m_g is a constant value, simplifying equation (2.3.1) we can rewrite:

$$\frac{\partial < c >}{\partial t} + \frac{\partial < cu_i >}{\partial x_i} = 0 \tag{2.3.2}$$

x indicates the longitudinal direction of the flow, while y stands for the normal to the flow direction. Considering a 2D statistically stationary and homogeneous flow in the longitudinal direction x , in which, however, we assume that the condition of homogeneity and stationarity is reached in a time interval of the same order of the time scale that governs the kinetic theories (that is, in a single realization), equation (2.3.1) reduces to:

$$\frac{\partial < cu_y >}{\partial y} = 0 \tag{2.3.3}$$

where y indicates the normal direction. This implies that $< u_y >$ is equal to zero along the entire depth; that is, no vertical component of the mean motion is present.
In the case of granular material, since the system is not ergodic, the average of a single realization is not the same of that of more realizations and the average procedure introduced by us must be applied. Consequently, Eq. (2.3.1) must be further averaged on all the realizations, that is:

$$\frac{1}{R} \sum_{k=1}^{R} \frac{\partial}{\partial y} (\widetilde{u}_y^{(k)} \widetilde{c}^{(k)}) = 0 \tag{2.3.4}$$

Afterwards, we express the variables averaged on a single realization $\widetilde{u}_y^{(k)}$ and $\widetilde{c}^{(k)}$ as the sum of a mean value and of a fluctuating portion, recalling the Reynolds decomposition:

$$\widetilde{u}_y = \overline{u}_y + u'_y, \qquad \widetilde{c} = \overline{c} + c', \tag{2.3.5}$$

where, by definition $\overline{u'_y} = \overline{c'} = 0$, and $\overline{u}_y$ and $\overline{c}$ are values averaged according to equation (2.2.9).
Inserting these terms in (2.3.4), we obtain the following equation:

$$\frac{\partial}{\partial y}(\overline{c}\,\overline{u}_y) + \frac{\partial}{\partial y}\overline{c'u'_y} = 0 \tag{2.3.6}$$

Equation (2.3.6) in the y-direction implies that $\overline{u}_y \neq 0$; then it follows that:

$$\overline{c}\,\overline{u}_y = -\overline{c'u'_y} \tag{2.3.7}$$

It is easy to prove that if we had adopted the mass average definition in the averaging processes Eq. (2.2.8), instead of eq. (2.3.6), we would have obtained the following equation:

$$\frac{\partial}{\partial y}(\overline{c}\,\widehat{u}_y) = 0 \tag{2.3.8}$$

from which, in this case, results that the mass averaged vertical component of the velocity is $\widehat{u}_y = 0$ along the intere flow depth.

From the experimental analysis (presented in Chapter 6), the vertical component of the velocity results to be different from zero. In particular it is about 4% of the longitudinal velocity component; for a maximum longitudinal velocity of about 0.9 m/s the vertical velocity profile is that reported in Fig. 2.1. This result seems to prove our previous consider-

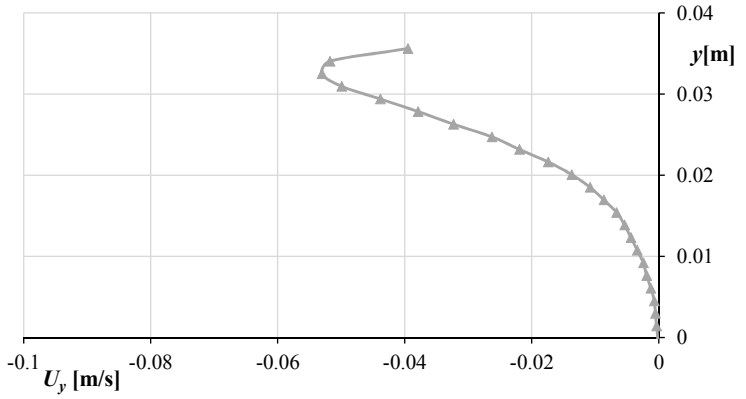

Figure 2.1: *Vertical velocity component*

ations; anyway further investigations are necessary to verify the possible presence of secondary circulations, which may cause themselves this component. Indeed, in our experiments (see Chapter 1.1.8), transversal gradients may be occur and lead to secondary circulations.

Chapter 3

Three-dimensional particle numerical simulations of a uniform channel flow of dry granular material

Particle numerical simulations have been performed to reproduce a uniform channel flow of dry granular material. The three-dimensional result have been analyzed in order to both verify the correspondence between the experiments and the numerical simulations and to obtain a complete 3D analysis of the flow motion.
Furthermore, this type of simulations allow us to investigate the influence of different parameter (e.g. the restitution coefficient e, solid phase density ρ_s or material friction coefficient) on the flow mechanics. These parameters are difficult to be changed in the laboratory investigations, due to the high costs and the difficulty to find materials with precise characteristics.

3.1 Molecular dynamics simulator: LAMMPS

A classical Molecular Dynamics simulator has been adopted: LAMMPS (Plimpton, 1995), which stands for *Large-scale Atomic Molecular Massively Parallel Simulator*. LAMMPS integrates Newton's equations of motion for collections of particles at different length and time scale (from the electrons scale to the coarse-grained and the continuum). Granular flow is composed by uniform spheres, as in the experimental tests. The

characteristics of the single particle motion and its interaction with the others is the output of the model.

Interaction model

The interactions among particles are reproduced through a traditional Hertzian-spring model, characterized by a spring in parallel with a dissipator. The deformation of the particles is accounted for.
Given a spatial overlap δ of the two particles i and j:

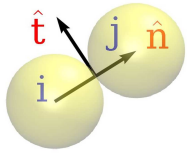

Figure 3.1: *Particle interaction scheme*

$$\delta = \delta_{\hat{n}}\hat{n} = [d - (R_i + R_j)] \tag{3.1.1}$$

where R_i and R_j are the radius of the two spheres, the tangential displacement is:

$$\delta_{\hat{t}} = \left| \int_{t_0}^{t} \dot{\delta}_{\hat{t}}(\tau)\, d\tau \right| \tag{3.1.2}$$

where $\dot{\delta}_{\hat{t}}$ is the relative tangential velocity $v_i - v_j$ and the interval $t - t_0$ is the collision time.
The contact force is expressed as:

$$\mathbf{f} = \mathbf{f}_{\hat{n}} + \mathbf{f}_{\hat{t}} \qquad \text{with} \qquad \mathbf{f}_{\hat{t}} \leq \mu \mathbf{f}_{\hat{n}} \tag{3.1.3}$$

Explicating the contact force:

$$\begin{aligned} \mathbf{f} = &\mathbf{f}_{\hat{n}} + \mathbf{f}_{\hat{t}} = \left(\sqrt{\delta_{\hat{n}} R^*} k'_{\hat{n}} \delta_{\hat{n}} - \sqrt{m^* \sqrt{\delta_{\hat{n}} R^*}} \gamma'_{\hat{n}} \dot{\delta}_{\hat{n}} \right) \hat{n} + \\ &\left(-\sqrt{\delta_{\hat{n}} R^*} k'_{\hat{n}} \delta_{\hat{n}} - \sqrt{m^* \sqrt{\delta_{\hat{n}} R^*}} \gamma'_{\hat{n}} \dot{\delta}_{\hat{n}} \right) \hat{t} \end{aligned} \tag{3.1.4}$$

In Eq.(3.1.4), the effective mass m^* and radius R^* are computed as $1/m^* = 1/m_i + 1/m_j$ and $1/R^* = 1/R_i + 1/R_j$. The other coeffi-

cients are computed as indicated in the following:

$$\begin{aligned} k'_{\hat{n}} &= \frac{4}{3}E^* \\ k'_{\hat{t}} &= 8G^* \\ \gamma'_{\hat{n}} &= 2\frac{\ln e}{\sqrt{\ln^2 e + \pi^2}}\sqrt{\frac{5}{3}E^*} \\ \gamma'_{\hat{n}} &= 2\frac{\ln e}{\sqrt{\ln^2 e + \pi^2}}\sqrt{\frac{20}{3}G^*} \end{aligned} \tag{3.1.5}$$

with e the coefficient of restitution, E^* and G^* the Young modulus and the shear modulus, computed as:

$$\begin{aligned} \frac{1}{E^*} &= \frac{1-\nu_i^2}{E_i} + \frac{1-\nu_j^2}{E_j} \\ \frac{1}{G^*} &= \frac{2(2-\nu_i^2)(1+\nu_i^2)}{E_i} + \frac{2(2-\nu_j^2)(1+\nu_j^2)}{E_j} \end{aligned} \tag{3.1.6}$$

where ν is the Poisson's ratio.

Geometry of the problem

The experiments reproduced by the particle numerical simulations are in statistically stationary and homogeneous flow conditions, in a rectangular channel. In these simulation the vertical axes is z, the longitudinal direction is y and the direction transversal to the channel is x.
The stationarity of the flow is obtained applying periodic boundary conditions along the y axis (Fig.3.2); a weir (green shape in Fig. 3.2) is used as a mathematical artifice to reach the equilibrium condition in a shorter channel length. Since the homogeneous flow conditions develops far from the boundaries, a sampling volume is considered, sufficiently far from boundaries (yellow box).

Simulation parameters

The parameter necessary to perform the simulations, are not straightforward to be determined. In the experimental test, the particles material is polystyrene (PS), while the channel is made of perspex (PMMA). The Young's modulus, the Poisson's ration and the other parameter have been chosen according to the literature suggestions about the type of material used in the experiments. Regarding the the friction coefficient between particles and wall (that is between PS and PMMA), it has been roughly

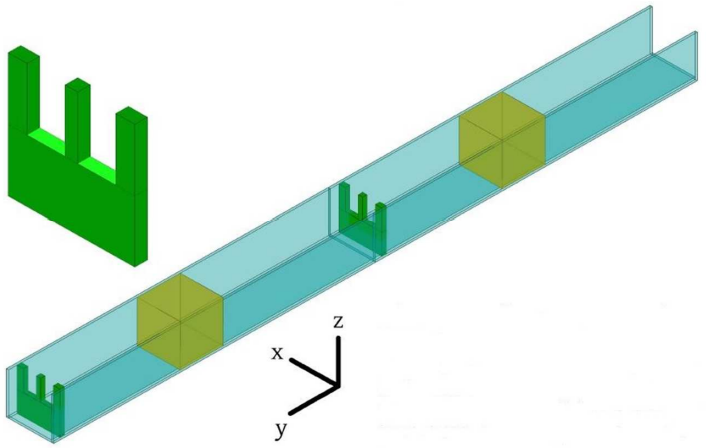

Figure 3.2: *Channel scheme*

estimated as the mean value of the PS-PS friction and the PMMA-PMMA friction. Finally, the rolling friction coefficient has been assumes to be null.

Simulation process

The first step of the simulation consist of an initialization process: the particles are placed randomly inside the channel (the ratio between the number of particle and the volume analyzed is about $N/V = 0.25$) under the gravity force along z, with an initial slope of the bed $\alpha = 0°$. Then the equation of motion are integrated, till the total kinetic energy is reasonably low, in order to reduce the computational time needed to reach the equilibrium. Then the gravity vector is tilted according to the desired angle of inclination, and again the equations of motion are integrated till the kinetic energy is constant enough.
At this point, the second step of the simulation: production of the data. Particles kinematics properties are collected for a time interval long enough to analyze the motion of the flow.

Output of simulations

The output of the simulations are all the characteristics of the single particle and of the interaction between every couple of particles.
The main features we are interested in are the velocity distribution in the three dimensions x, y and z, the concentration distribution in an entire

section of the channel. Thus allow to evaluate the gradients of the velocities and concentrations along the width of the channel and along the depth of the flow.
Finally, the results could be compared with the measurements done during the experimental test and verify the effectiveness of both the results.

3.1.1 Results of the simulations

In the following, a deep analysis of the simulations results is presented. In particular the analysis is aimed to understand the relation between the wall values of the variables of interest and their areal averaged value. This allow us to switch from the wall measurements done during the experimental tests to the corresponding areal averaged values. We adopted thre particles characteristics similar to those used for the experimental investigation:

- spherical particles, of diameter 0.00075 m
- particle-particle restitution coefficient 0.87
- particle-wall restitution coefficient 0.92
- particles density 1.03 Kg/m^3

Flow depth

The first aspect tackled through the particles simulations, is how the flow depth varies from to wall to the center of the channel.
An example of the flow depth transversal profile is reported in Fig. 3.3, together with the free surface and bed elevation profiles.
The flow depth is the difference between the free surface and the bed elevation, as it is clearly visible in the Figure. As we may expect, there is a gradient along the width of the channel: the flow depth has a minimum value at the wall and increases till the centerline to its maximum. Clearly, this behavior is due to the interaction between the particles and the wall. Furthermore, the gradient is stronger near the wall, while the flow depth seems to reach a more constant value in central part of the channel.

Velocity profiles

Regarding the velocities, both the distribution in the normal plane and in the transversal plane with respect to the direction of the flow have been investigated.
The velocity profile at the wall of the channel is of crucial interest, since

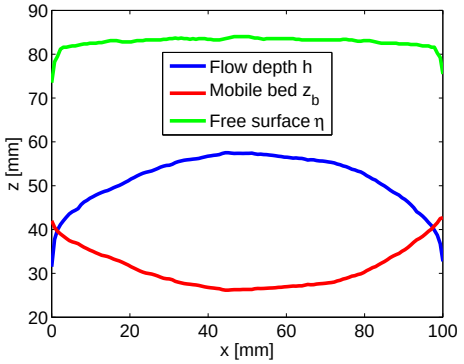

Figure 3.3: *Flow depth profile*

it is the only one comparable with the experimental analysis. An example is represented in Fig. 3.4. It is of great interest to compare this profile

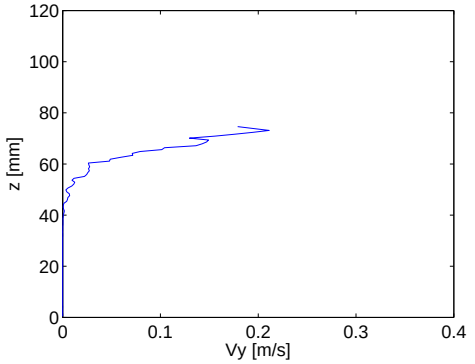

Figure 3.4: *Wall velocity profile*

with the velocity profile in the middle of the channel (comparison in Fig. 3.5); this allow us to see how the wall influences the velocity values and distribution. Firstly, it is clearly visible a difference in the height of the moving layer: the particles far from the wall move at lower distance from the bed, so that the flow depth is greater far from the wall (as observed in Fig. 3.3).
Secondly, the velocity at the centerline of the channel is higher reach higher values, as we can observe in Fig. 3.6 that shows the transversal velocity distribution. In particular, the longitudinal velocity is represented along the entire width of the channel, at different distances from the bed (Fig. 3.6). The difference between the wall velocity values and the velocity far from the wall in quite pronounced, in particular in the up-

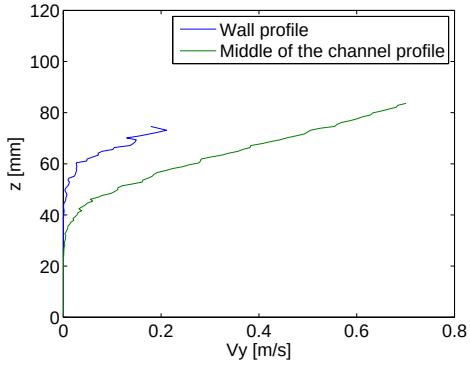

Figure 3.5: *Comparison between wall and middle of the channel profiles of the longitudinal velocity*

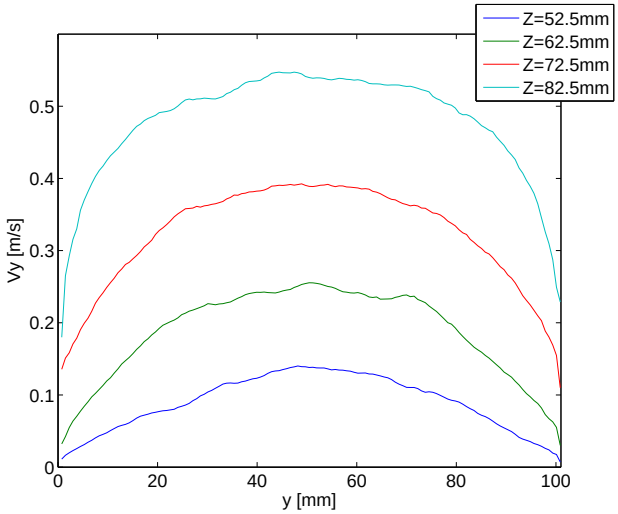

Figure 3.6: *Transversal velocity profiles*

per layers. In order to analyze if and where the wall influence becomes negligible, we have compared the velocity profile at different depth from the wall in Fig. 3.7: At a distance of about 40 particles diameter, the velocity profile is almost equal to the profile corresponding to the middle of the channel.

Concentration profiles

The analysis done for the velocity, has been reproduced for the concentration too.

The wall concentration has been compared with the profile at the middle of the channel in Fig. 3.8. It is worth to notice that during the molecular simulation, the concentration of the particle is computed in a volume of dimension d^3. It is the ratio between the total volume and the volume occupied by the particles; by definition it is a $3D$ concentration. This is the reason why the wall value is much lower then in the center of the channel: the presence of the wall affect the concentration making it much lower with respect to the centerline.
In order to understand when the wall effect expires, the concentration profiles has been compared at different distance from the wall, finding that at a distance of about 10 particle diameters the profile is almost equal the that far from the wall. We may conclude that the influence of the wall has much effect on the velocity than on the concentration.
Finally, the concentration at different distance from the bed is represented in Fig.3.10. On the free surface (light blue line) the concentration at the wall is lower, even if the wall effect is visible at every depth, with a steep decreasing of the concentration value on the left and right bounds. Furthermore, a central plateau is clearly visible at each depth; the difference is that going more in depth (lower z) the transition between the wall concentration and the plateau value is sharper.

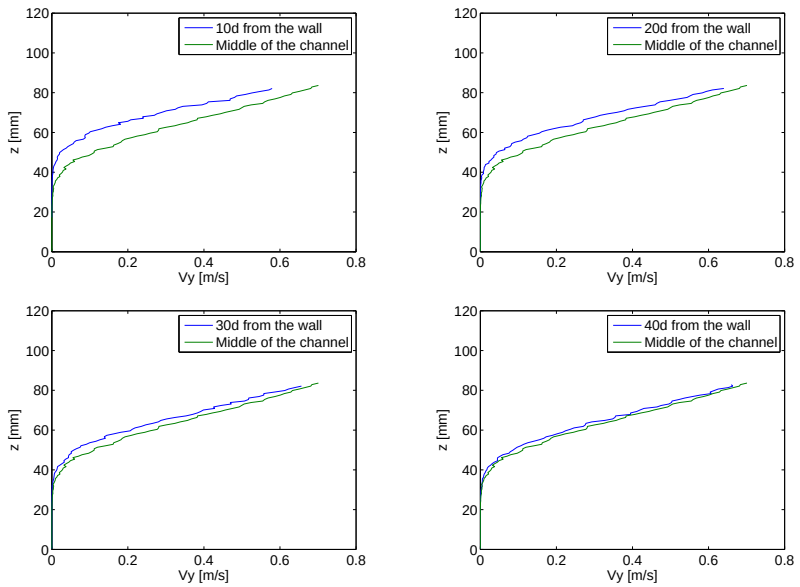

Figure 3.7: *Comparison of the velocity profile at different depth from the wall*

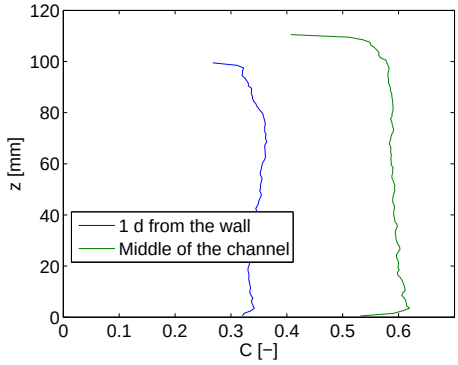

Figure 3.8: *Comparison between wall and middle of the channel profiles*

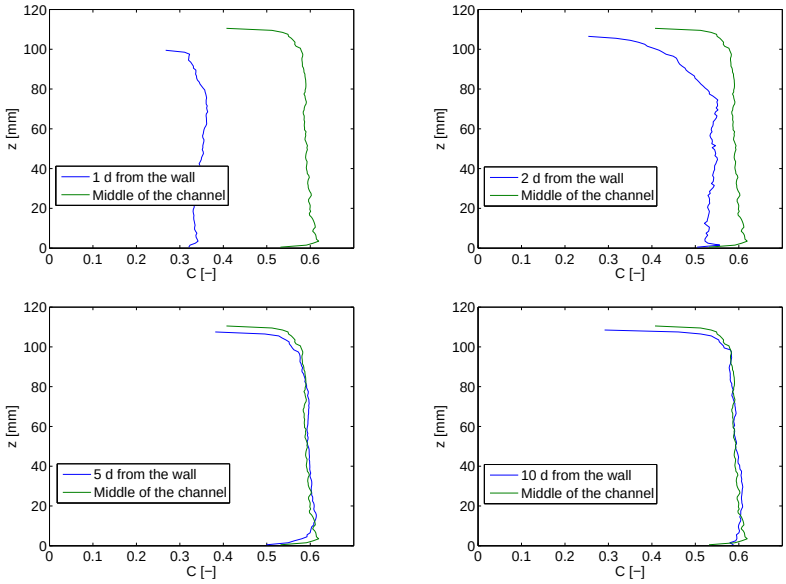

Figure 3.9: *Comparison of the concentration profile at different depth from the wall*

3.1.2 Wall and areal averaged values of the variables

In the experimental analysis presented in Chapter 6, the values measured of the flow depth, flow velocity and concentration of the solid phase are registered from the wall of a transparent channel. Anyway, in general when we are interested in modeling the flow, the values needed are the areal averaged values. For this reason, the molecular dynamics simulations have been used to define the ratio between the wall value and

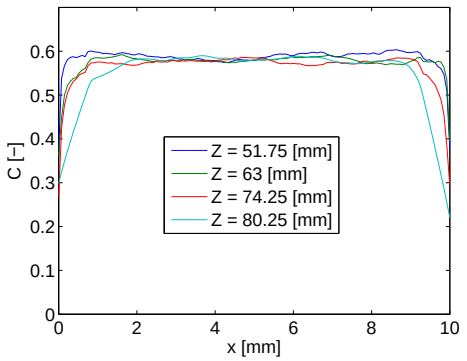

Figure 3.10: *Comparison between wall and middle of the channel profiles*

the areal averaged value of each variable of interest.
Regarding the average flow depth, we have chosen as starting point of the flow depth that corresponding to the 0.1% of the maximum velocity on the free surface. By apply this criterion along the entire width of the channel, the mean flow depth $\bar{h}$ on the entire area may be computed:

$$\bar{h} = \frac{\sum_{i=1}^{N_W} h_i}{N_W} \tag{3.1.7}$$

where N_w is the number of elements in which has been discretized the width of the channel, and h_i the corresponding flow depth.
Comparing the value of the flow depth averaged on the width of the channel with the wall value h_w, a coefficient r_h has been defined as:

$$r_h = \frac{\bar{h}}{h_w} \tag{3.1.8}$$

The coefficient r_h results to be about 1.35.
Regarding the areal averaged velocity, it is computed as:

$$U = \frac{\int_A u \, dA}{A} \tag{3.1.9}$$

where A is the area corresponding to the flowing particles, that we have considered from the height at which particles have a velocity equal to the 0.1% of the maximum velocity, as before.
The same procedure may be applied for the areal averaged concentration C:

$$C = \frac{\int_A c \, dA}{A} \tag{3.1.10}$$

By comparing the averaged value U and C just described with the corresponding wall values, these further two coefficients have been determined:

$$r_U = \frac{U}{U_w} \tag{3.1.11}$$

$$r_C = \frac{C}{C_w} \tag{3.1.12}$$

where U_w and C_w are the depth averaged velocity and concentration at the wall. The values for the coefficients are respectively about 1.45 and 1.15.

Chapter 4

1D depth integrated models for dry granular flows

Dry granular flows are characterized by a mixture of solid particles and an interstitial fluid, that is air. One of the most dangerous and scientifically interesting example of this type of flows are the dry snow avalanches: they are composed by particles of snow and ice immersed in air. Due to the complexity of the phenomenon, there are many issues still open regarding the modeling of such phenomena.

4.1 Mathematical model for dry granular flows

All the existing models for dry granular flows are based on the integration of the mass conservation and momentum conservation equations. They differ from each other in the definition of different closure relations or in the empirical source terms, used to reproduce the entrainment effect. The first attempt to model these phenomena goes back to the 50s (Voellmy, 1955; Salm, 1966, 1967): the Voellmy-Salm model for its simplicity and since it requires only few input parameters is very well-liked by practitioners. Anyway, it has some limitations: the flow is one-directional, has constant width, is a steady flow with constant mass (no entrainment is considered). These assumptions make the model over simplify the phenomena. Furthermore the pressure developed by the flow is not derivable from this model. For these reasons, the Voellmy-Salm model has been integrated and improved in AVAL-1D (Issler, 1998; Bartelt et al., 1999; Sartoris and Bartelt, 2000). In this model the main assumptions are (Christen et al., 2002):

a Flowing snow is modelled as a fluid continuum of mean constant flow density;

b The flow width is known;

c A clearly defined top flow surface exists;

d The flow height is the average flow height across the section;

e The vertical pressure distribution is hydrostatic;

g The avalanche mass is constant and no entrainment processes are modelled.

Since the model is based on the Voellmy-Salm rheology, the flow resistance is assumed to be concentrated at the base of the avalanche and is characterized by a dry-Coulomb type friction and a velocity squared (Chezy) friction. Tensile and compressive stresses are modeled through active and passive pressures, respectively. The parameters have been calibrated in Bartelt et al. (1999). The main difference introduced in the model AVAL-1D is that the flow is no more stationary.
In 2010 the SLF group (*WSL Institute for Snow and Avalanches Reserch SLF*) presented a new 2D model: RAMMS (Christen et al., 2010) solves the depth-averaged equations governing avalanche flow through a second-order numerical solution schemes. In this model, snow entrainment is considered and two different rheologies may be applied: again the standard Voellmy–Salm approach or a random kinetic energy (RKE) model (it accounts for the random kinetic energy and inelastic interaction among snow particles) (Buser and Bartelt, 2009). The entrainment is modeled by dividing the snow cover in different layers, each one with a certain density: the entrainment rate depends on the density of the layer itself and on the flow velocity. Definitely, the model is a fixed bed model and the entrainment is inserted artificially.
In literature there are other models, like that of the Norwegian *NIS* (Norem et al., 1987, 1989), which, contrary to AVAL-1D, consider a gradient of the longitudinal velocity along the flow depth and the active and passive pressure parameters do not exist, but are modeled through the friction slope. Furthermore Russian researchers too developed a depth-averaged continuum model for snow avalanches (Eglit, 1998): it differs from the AVAL-1D into two main aspects (Bartelt et al., 1999). Firstly, the friction law is different, since an upper limit has been introduced on the dry friction; secondly, even this model does not distinguish the active and passive regimes.
Finally, the Hutter and Savage model is widespread in the avalanche field (Savage and Hutter, 1991): the mass and momentum conservation equations, written in terms of curvilinear coordinates, are depth integrated

obtaining the evolution of the flow depth and of the depth averaged velocity. The constitutive relation describing the material behavior is assumed to be a Niohr-Coulomb criterion; the boundary condition at the bed is instead a Coulomb-type basal friction law. Furthermore, in this model the variations of the bulk density of the sliding mass is neglected, that is the average concentration of the flowing material is assumed constant. However this is not always true, in particular when the collisional regime prevails.

4.2 A new mathematical approach

In this section we present a new 1D depth integrated model, which is based on a two phase approach. It is characterized by at least three main innovative aspects:

- the equations needed to describe mathematically the two-phase flow are derived from the mass balance of the two phases (solid particles and fluid, that is air) and the momentum balance for the solid phase;

- it is a mobile bed model, accounting for erosion and deposition without any artificial formulation;

- the solid phase concentration is not considered constant, but it is assumed to be a function of the velocity of the flow and of the flow depth.

The model is derived starting from the hypotheses of non-stationary and non-homogeneous flow and applying, in these conditions, the mass and momentum balance. Fig. 4.1 and Fig. 4.2 show the scheme considered.
In the Figure, h is the flow depth, C the concentration, A the area of the transversal section, z_b the elevation of the mobile bed. Finally, α_{fs} and α_{z_b} are respectively the slope of the free surface and of the bed, that in case of dry granular flow do not always coincide.
In the following three partial differential equations necessary to describe the dynamics of this granular arrangement are presented.

4.3 Mass balances

The granular ensemble is inclined of an angle α_{zb} with respect to the horizontal and vertical plane (coordinates $x - z$). Furthermore, typically, the inclination of the static bed (α_{zb}) is different from that of the free

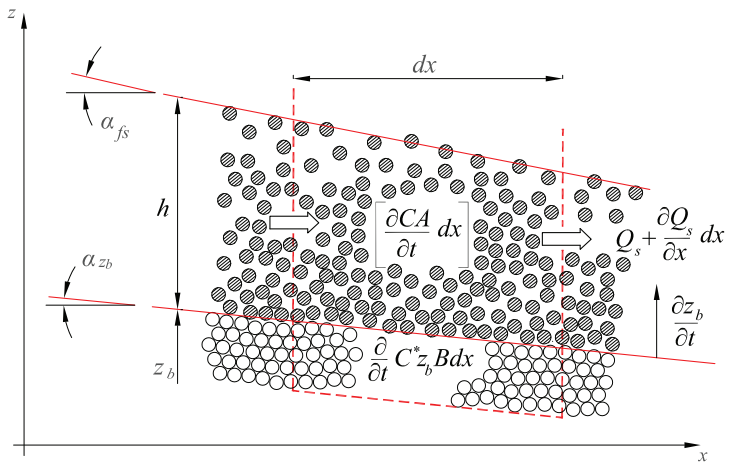

Figure 4.1: *Reference system for the mass balance*

surface (α_{fs}), since a dry granular flow assumes its own inclination with respect to the fixed bottom of the channel.
If the bed and the free surface are not parallel, there is an ambiguity in the definition of the average direction of the motion and consequently in the definition of the depth averaged velocity. For sake of simplicity, in the following we assume that the depth averaged velocity U is parallel to the bed; furthermore the control volume considered is of infinitesimal length so that the two slopes α_{zb} and α_{fs} may be considered equal to each other. In the computation of the forces in the next sections we will keep two different slopes, but only for exposition aim.
In the following, C stands for the depth averaged value of the concentration $c(y)$ of the flow.

4.3.1 Solid mass balance

Starting from the general formulation:

$$\frac{\partial}{\partial t}\iiint_{\forall_c} \rho\, d\forall + \iint_{\Sigma_c} \rho \mathbf{u}_x \cdot d\mathbf{A} = 0 \tag{4.3.1}$$

Considering the variation of the solid mass within the control volume (Fig. 4.1), we have that the first term is made up of the following two parts:

$$\frac{\partial}{\partial t}[\rho\, C\, h\, B\, dx] + \frac{\partial}{\partial t}[\rho\, C^*\, z_b\, B\, dx] \tag{4.3.2}$$

The second term of equation (4.3.1) may be written as:

$$\frac{\partial}{\partial x}[\alpha_{cu}\rho C\, U_x\, h\, B\, dx] \tag{4.3.3}$$

where α_{cu} is a correction coefficient raising from the integral of the product uc. It takes into account that the integral of the product is not the product of the single integrals.

$$\alpha_{cu} = \frac{\int\limits_h c\, u\, dy}{\int\limits_h c\, dy \int\limits_h u\, dy} \tag{4.3.4}$$

In conclusion, simplifying by dx and ρ, we obtain:

$$\frac{\partial}{\partial t}[C\, h\, B + \rho\, C^*\, z_b\, B] + \frac{\partial}{\partial x}[\alpha_{cu} C\, U_x\, h\, B\, dx] = 0 \tag{4.3.5}$$

where U_x is the x-component of the averaged velocity.
If U is the depth averaged velocity its horizontal component is:

$$U_x = U\, \cos\alpha_{z_b} \tag{4.3.6}$$

Finally, we may rewrite the solid mass balance in direction x as follows:

$$\frac{\partial}{\partial t}[C\, h\, B + \, C^*\, z_b\, B] + \frac{\partial}{\partial x}[\alpha_{cu} C\, U\, \cos\alpha_{z_b}\, h\, B\, dx] = 0 \tag{4.3.7}$$

4.3.2 Air mass balance

Similarly, for the air mass balance we obtain:

$$\frac{\partial}{\partial t}[(1-C)\, h\, B + (1-C^*)\, z_b\, B] + \frac{\partial}{\partial x}[(1-\alpha_{cu}C)\, U_{ax}\, h\, B] = 0 \tag{4.3.8}$$

Expressing the velocity in terms of the longitudinal velocity U:

$$\frac{\partial}{\partial t}[(1-C)\, h\, B + \, (1-C^*)\, z_b\, B] + \frac{\partial}{\partial x}[(1-\alpha_{cu}C)\, U_a\, \cos\alpha_{z_b}\, h\, B] = 0 \tag{4.3.9}$$

4.3.3 Total mass balance

Alternatively to the second mass balance, we may substitute the total momentum balance, making the *iso-kinetic hypothesis* $U_a = U$. This implies that the air velocity U_a is equal to the solid phase velocity U.

$$\frac{\partial}{\partial t}[h\, B + z_b\, B] + \frac{\partial}{\partial x}[U_x\, h\, B] = 0 \tag{4.3.10}$$

Considering again the total velocity in the longitudinal direction of the flow U, the equation reads:

$$\frac{\partial}{\partial t}[h\,B + z_b\,B] + \frac{\partial}{\partial x}[U\,\cos\alpha_{z_b}\,h\,B] = 0 \tag{4.3.11}$$

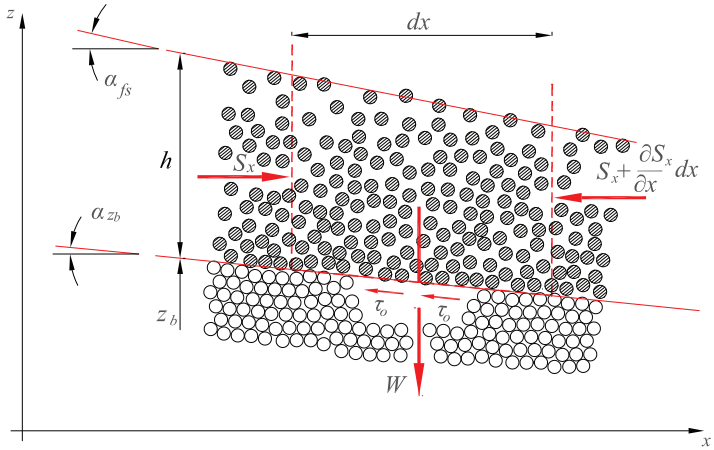

Figure 4.2: *Reference system for the momentum balance*

4.3.4 Momentum balance of the solid phase

Let's start with the general formulation:

$$\frac{\partial}{\partial t}\iiint_{\forall_c}\rho\,\mathbf{u}_x\,d\forall + \iint_{\Sigma_c}\rho\mathbf{u}_x(\mathbf{u}_x\cdot d\mathbf{A}) = \mathbf{F}_{e,x} \tag{4.3.12}$$

where F_e stands for the sum of the external forces, that is weight, surface forces, inter-phase forces (solid-air, e.g. drag force).
Starting from the first term of (4.3.12), with reference to Fig. 4.2, it may be written as follows:

$$\frac{\partial}{\partial t}[\alpha_{cu}\rho\,C\,U_x\,h\,B]dx \tag{4.3.13}$$

And as a function of the longitudinal velocity U:

$$\frac{\partial}{\partial t}[\alpha_{cu}\rho\,C\,U\,\cos\alpha_{z_b}\,h\,B]dx \tag{4.3.14}$$

The second term of equation (4.3.12) becomes:

$$\frac{\partial}{\partial x}[\rho\,C\,U_x\,U_x\,h\,B\,\beta_{cu}]dx \tag{4.3.15}$$

where β is a further correction coefficient raising from the integration of the product of the variables. As a function of the longitudinal velocity U, we may rewrite the second term of the momentum balance as:

$$\frac{\partial}{\partial x}[\rho\, C\, U^2 \cos^2 \alpha_{z_b}\, h\, B\, \beta_{cu}]dx \tag{4.3.16}$$

The last component of equation (4.3.12) are the external forces, here itemized:

- Weight: $G = \rho\, C\, h\, B\, dx$. However, the weight component is vertical and do not have any contribution in x-direction.
- Surface forces due to the static pressure. The distribution of pressure is hydrostatic along n; note that $\partial n/\partial z = \cos \alpha_{fs}$ (see Fig. 4.3). The exerted force is:

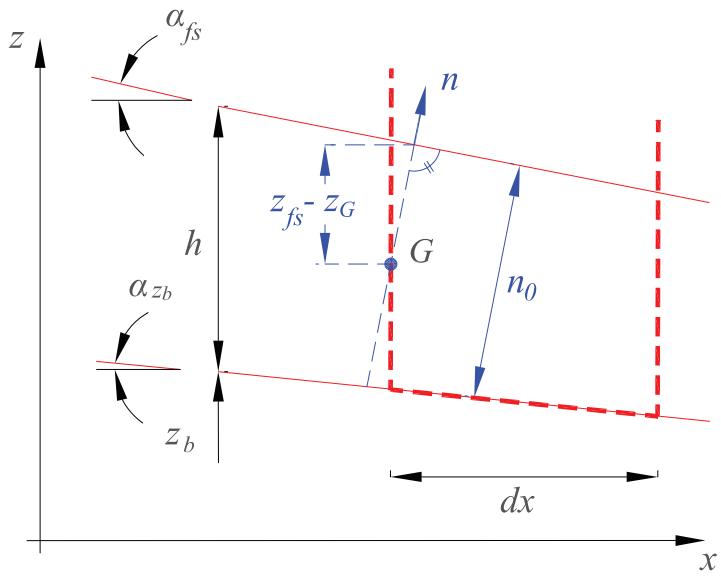

Figure 4.3: *Reference system for the computation of the hydrostatic pressure*

$$\frac{\partial}{\partial x}[B\, h\, p_G]dx \tag{4.3.17}$$

According to the *second Euler equation*, since the path lines can be considered almost parallel to each other (negligible curvature),

we may write along n:

$$\frac{\partial}{\partial n}[p + \rho\, g\, C\, z] = 0 \tag{4.3.18}$$

The pressure in the barycenter results to be:

$$p_G = p_{fs} + \rho\, g\, C\, (z_{fs} - z_{G)} = \rho\, g\, C\, \frac{h}{2} \cos^2 \alpha_{sl} \tag{4.3.19}$$

By substituting in Eq. (4.3.17):

$$\frac{\partial}{\partial x}[\rho\, g\, C\, B\, \frac{h^2}{2}\, \cos^2 \alpha_{fs}]dx \tag{4.3.20}$$

- Lateral forces (if $\dfrac{\partial B}{\partial x} \neq 0$). See Fig 4.4. It is exerted on a length of

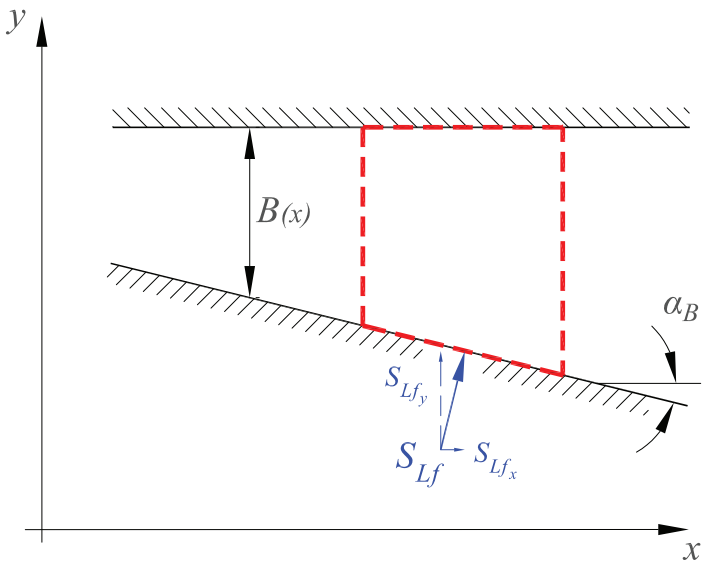

Figure 4.4: *Lateral forces scheme*

$dx/\cos\alpha_B$ (where α_B is the angle of deviation of the lateral wall) and the component along x is obtained multiplying by $\sin\alpha_B$.

$$\frac{1}{2}[\rho\, g\, C\, h^2\, \cos^2 \alpha_{fs}] \frac{dx}{\cos\alpha_B} \sin\alpha_B \tag{4.3.21}$$

The pressure in the barycenter is computed as explained before. Since:

$$\sin\alpha_B = \frac{\partial B}{\partial x} \cos\alpha_B \tag{4.3.22}$$

the final formulation is:

$$\frac{1}{2}[\rho\, g\, C\, h^2\, \cos^2 \alpha_{fs}]\, dx \frac{\partial B}{\partial x} \tag{4.3.23}$$

- Bed surface forces. We compute the pressure on the bed according to Eq. (4.3.18) and we obtain:

$$p_{z_b} = p_{fs} + \rho\, g\, C\, (z_{fs} - z_{z_b)} = \rho\, g\, C\, n_0 \cos \alpha_{fs} \tag{4.3.24}$$

Considering that $n_0 = h\, \cos \alpha_{fs}$ and assuming that $\alpha_{fs} \approx \alpha_{z_b}$ the pressure at the bed reads:

$$p_{z_b} = \rho\, g\, C\, h\, \cos^2 \alpha_{z_b} \tag{4.3.25}$$

The surface force at the bed is distributed on a length along x equal to $\dfrac{dx}{\cos \alpha_{zb}}$ (see Fig. 4.5), so that:

$$S_{z_b} = p_{z_b}\, B\, \frac{dx}{\cos \alpha_{z_b}} = \rho\, g\, C\, h\, B\, \cos^2 \alpha z_b \frac{dx}{\cos \alpha_{z_b}} = \rho\, g\, C\, h\, B\, dx \tag{4.3.26}$$

The scheme of the coordinates related to an inclined channel is represented in Fig. 4.5: Considering the component along x, we have to multiply by $\sin \alpha_{z_b}$:

$$S_{z_b,x} = \rho\, g\, C\, h\, B\, \cos^2 \alpha_{z_b} \frac{\partial z_b}{\partial x} \tag{4.3.27}$$

Indeed:

$$\sin \alpha_{z_b} = \frac{\partial z_b}{\partial x} \cos \alpha_{z_b} \tag{4.3.28}$$

- Bed friction. The component along x is:

$$\tau_{0,x} = \tau_0\, B\, dx\, \cos \alpha_{zb} \tag{4.3.29}$$

Finally, considering a constant width B of the channel, the momentum balance in the x-direction results to be:

$$\begin{aligned} &\frac{\partial}{\partial t}[\alpha_{cu}\, C\, U \cos \alpha_{z_b}\, h\, B] + \frac{\partial}{\partial x}[C\, U^2 \cos^2 \alpha_{z_b}\, h\, B\, \beta_{cu}] + \\ &\quad + B\, g \frac{\partial}{\partial x}[C\, \frac{h^2}{2}\, \cos^2 \alpha_{fs}] + g\, C\, h\, B\, \frac{\partial z_b}{\partial x} \cos^2 \alpha_{z_b} = -\frac{\tau_{0,x}\, B}{\rho} \end{aligned} \tag{4.3.30}$$

In order to close the system, we need two closure relations, that will be derived in the next Chapter 5.

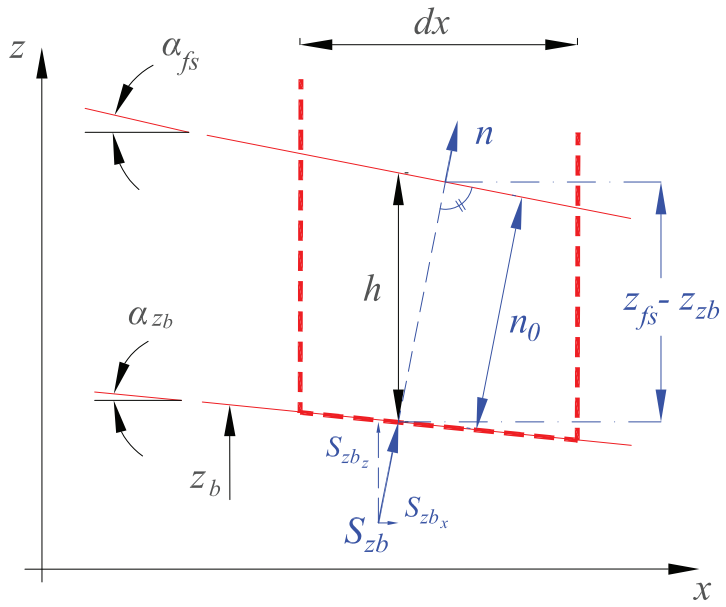

Figure 4.5: *Bed forces scheme*

4.4 Eigenvalues of the system

The eigenvalues of the mathematical model have been analyzed, in order to verify that the system is hyperbolic and that three real and different eigenvalues exist. The analysis has been carried out for different Froude numbers and for different ratio between the particles diameter and flow depth d_p/h.

4.5 Complete form of the system: re-arrangement for the time derivatives

In order to compute the eigenvalues of the system, we needed a single time derivative in each equation. The procedure adopted consists in computing the single time derivative as a function of the others and substitute it in the other equations. In the end, we have a system with only

one time derivative for equation. The system will look as follows:

$$\begin{cases} \dfrac{\partial h}{\partial t} + A_{11}\dfrac{\partial h}{\partial x} + A_{12}\dfrac{\partial u}{\partial x} + A_{13}\dfrac{\partial z_b}{\partial x} = S_1 \\ \dfrac{\partial U}{\partial t} + A_{21}\dfrac{\partial h}{\partial x} + A_{22}\dfrac{\partial u}{\partial x} + A_{23}\dfrac{\partial z_b}{\partial x} = S_2 \\ \dfrac{\partial z_b}{\partial t} + A_{31}\dfrac{\partial h}{\partial x} + A_{32}\dfrac{\partial u}{\partial x} + A_{33}\dfrac{\partial z_b}{\partial x} = S_3 \end{cases} \tag{4.5.1}$$

where the primitive variables are h, U and z_b.
We may write the system in tha standard form, with the matrix $\mathbf{A}_Q$ as follows:

$$\mathbf{A}_Q = \begin{bmatrix} A_{11} & A_{12} & A_{13} \\ A_{21} & A_{22} & A_{23} \\ A_{31} & A_{32} & A_{33} \end{bmatrix}$$

Now we compute the determinant of the matrix:

$$\det(\mathbf{A}_Q - \lambda \mathbf{I}) = 0 \tag{4.5.2}$$

where $\mathbf{I}$ is the identity matrix.
So the polynomial equation we obtain is:

$$\begin{aligned} (A_{11} - \lambda)(A_{22} - \lambda)(A_{33} - \lambda) + A_{12}A_{23}A_{31} + A_{13}A_{21}A_{32} \\ - A_{31}(A_{22} - \lambda)A_{13} - A_{32}(A_{11} - \lambda)A_{23} + \\ - A_{21}(A_{33} - \lambda)A_{12} = 0 \end{aligned} \tag{4.5.3}$$

By multiplying the terms:

$$\begin{aligned} &-\lambda^3 + \lambda^2(A_{11} + A_{22} + A_{33}) \\ &+ \lambda(A_{31}A_{13} + A_{32}A_{23} + A_{21}A_{12} - A_{11}A_{22} - A_{11}A_{33} - A_{22}A_{33}) \\ &+ A_{12}A_{23}A_{31} + A_{13}A_{21}A_{32} - A_{31}A_{22}A_{13} - A_{32}A_{23}A_{11} + \\ &- A_{33}A_{21}A_{12} + A_{11}A_{22}A_{33} = 0 \end{aligned} \tag{4.5.4}$$

The dimension of this equation is, for example, that of the product $A_{11}A_{22}A_{33}$:

- $A_{11} = [LT^{-1}]$
- $A_{22} = [LT^{-1}]$
- $A_{33} = [LT^{-1}]$

So the final dimension is L^3T^{-3}.
The eigenvalues have been computed as dimensionless variables, by dividing everything by $(gh)^{1.5}$.
Then, by solving the polynomial dimensionless equation, we may see the evolution of the dimensionless eigenvalues.
In the following, the evolution of the eigenvalues is represented in function of the Froude number Fr, for different ratio d/h, where $\tilde{\lambda}_{i,ad} = \lambda_i/\sqrt{gh}$.

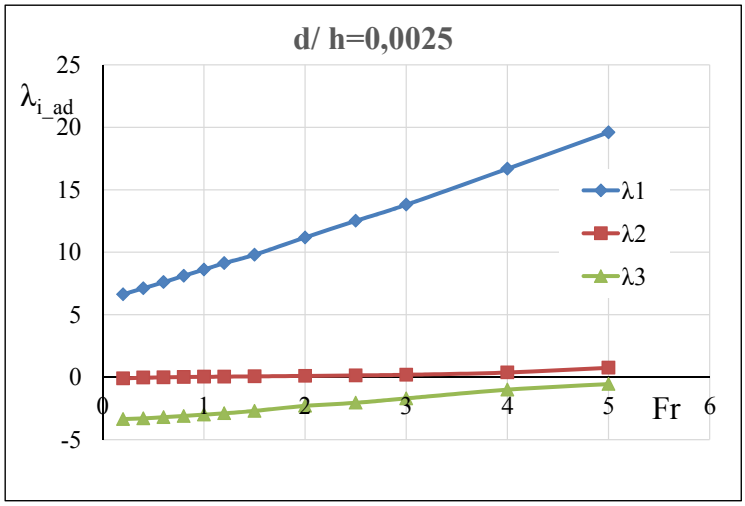

Figure 4.6: *Eigenvalues of the system for* $d/h = 0.0025$

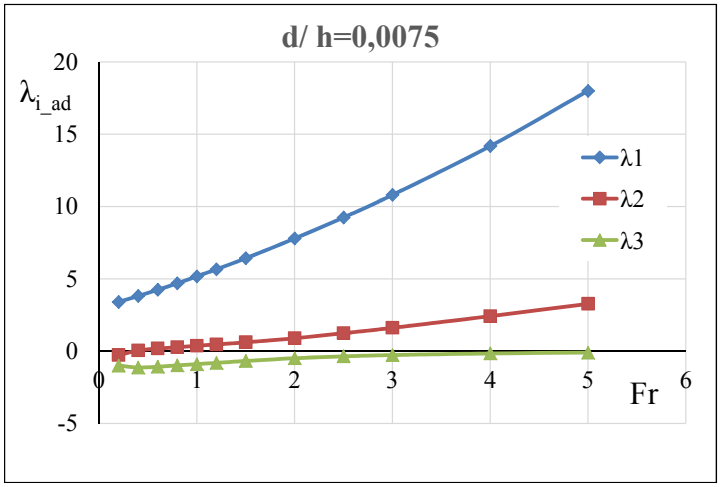

Figure 4.7: *Eigenvalues of the system for* $d/h = 0.0075$

Chapter 5

Closure relations for the mathematical model

The 1DH mathematical model, presented in the previous chapter, is composed by tree partial differential equations (i.e. mass and momentum balances of the solid phase and total mass balance). The system contains the following independent variables:

- U: depth averaged velocity of the flow;
- h: flow depth;
- z_b: mobile bed elevation;
- C: depth averaged concentration of the solid phase;
- τ_0: bed tangential stress;
- α_{cu} and β_{cu}: mass and momentum correction factors.

Since the number of unknowns is greater that the number of the partial differential equations, four further relations are needed.

As is usually the case for the shallow water equations, these equation, called *closure relations*, are derived from the momentum and mass balances in stationary and homogeneous condition. In this chapter we will therefore address the problem of the determination of such closure relation.

5.1 Preliminary considerations on the uniform flow condition

If we consider a uniform flow in a wide channel of a dry granular material, the momentum balances of the solid phase in the longitudinal (x_1) and normal (x_2) directions respectively, reduce to:

$$\frac{\partial \tau_{21}^g}{\partial x_2} = \rho_s\, g\, c\, \sin\alpha \tag{5.1.1}$$

$$\frac{\partial \sigma_{22}^g}{\partial x_2} = \rho_s\, g\, c\, \cos\alpha \tag{5.1.2}$$

where α is the free surface slope angle, which coincides with the bed inclination angle.

By integrating the above equations from the free surface elevation h and the generic elevation x_2, we obtain:

$$\tau_{21}^g = \int_{x_2}^{h} \rho_s\, g\, c\, \sin\alpha\, dx_2 \tag{5.1.3}$$

$$p^g = \int_{x_2}^{h} \rho_s\, g\, c\, \cos\alpha\, dx_2 \tag{5.1.4}$$

and

$$\frac{\tau_{21}^g}{p^g} = \frac{\int_{x_2}^{h} \rho_s\, g\, c\, dx_2 \sin\alpha}{\int_{x_2}^{h} \rho_s\, g\, c\, dx_2 \cos\alpha} = \tan\alpha \tag{5.1.5}$$

where we set $p = \sigma_{22}^g$. The equations state that, in uniform motion and broad channel hypotheses, the tangential stress τ and the normal stress p are balanced respectively by the longitudinal and normal components of the weight force. In addition, the ratio between the tangential and normal stresses results to be the tangent of the slope angle α. If we consider this ratio at the bed of the channel (i.e. at $x_2 = 0$), we obtain:

$$\left.\frac{\tau_{21}}{p}\right|_{y=0} = \tan\varphi \tag{5.1.6}$$

According to Eq. (5.1.6), it follows that $\tan\alpha = \tan\varphi$ everywhere in the flow.
However, it is worth to notice that if the width B of the channel is relatively short (e.g. $h/B <\sim 5 \sim 10$ (Meninno, 2015) Eq. (5.1.1) is not complete, since the effect of τ_{31} should included.

In order to solve the system (5.1.3-5.1.4) we have to assign the proper constitutive equations of the dry granular phase.

5.2 Constitutive equations of the granular phase

As specified in the chapter 4, to date there a complete and exhaustive rheological formulation capable of describing the behavior of a granular fluid does not exist yet. The question particularly focuses on coexistence in granular flows governed by the gravity along a large part of the flow depth of a regime characterized by the intermittent presence of long-lasting contacts (*frictional* or *dense*) and of instantaneous contacts (*collisional*).

It is known that the Bagnoldian (1954) formulation, that takes constant the concentration, for this type of flow entails the indetermination of the concentration itself, in fact:

$$\tau_{21}^{g} = \rho_s c \sin\varphi \left(\lambda d \frac{\partial u_1}{\partial x_2}\right)^2 \tag{5.2.1}$$

$$p^{g} = \rho_s a \cos\varphi \left(\lambda d \frac{\partial u_1}{\partial x_2}\right)^2 \tag{5.2.2}$$

where λ is the particle linear concentration. By coupling Eqs. (5.2.1) and (5.2.2) with Eqs. (5.1.3) and (5.1.4), it is easy to prove that the concentration c remains indeterminate.

The most convincing approach to the solution of this problem seems to be to consider the single component of the stresses tensor as the sum of two contributions (Jenkins and Savage, 1983), of which the first relates to the frictional regime and the second to the collisional. For the collisional component, the similarity with the kinetic theory of gases seems to be quite satisfying in many applications, while for the frictional component the question is still somewhat uncertain. In this regard, we have therefore decided to adopt a rheological formulation similar to the heuristic model proposed by Armanini et al. (2014). Ultimately, with reference to the uniform flow in question, the two rheological relation adopted are:

$$\tau_{21}^{g} = \tau_{21}^{coll} + \tau_{21}^{fric} \tag{5.2.3}$$

$$p^{g} = p^{coll} + p^{fric} \tag{5.2.4}$$

where τ^{fric} and τ^{coll} are the frictional and collisional components of the tangential stresses respectively and analogously for the pressures p.

Collisional component

The collisional contributions are expresses through the kinetic theory, i.e.:

$$\tau_{21}^{coll} = \rho_s \, f_2 \Theta^{0.5} \left(d \, \frac{\partial u_1}{\partial x_2} \right) \tag{5.2.5}$$

$$p^{coll} = \rho_s f_1 \, \Theta \tag{5.2.6}$$

where Θ is the granular temperature, d_p is the particles diameter, ρ_s is the material density of particles. The parameters f_1, f_2 are function of the particle concentration c and of the restitution coefficient e_p, and are defined in the following in Eqs. (5.2.8) and (5.2.9).

Of course the kinetic energy balance equation must be added to the above system:

$$\underbrace{-\frac{\partial}{\partial x_2}\left(f_4 \, \rho_s \, \Theta^{0.5} \, d \, \frac{\partial \Theta}{\partial x_2} \right)}_{Diff.} = \underbrace{\tau_{21}^{g} \frac{\partial u_1}{\partial x_2}}_{Prod.} - \underbrace{f_5 \, \rho_s \, \frac{\Theta^{1.5}}{d}}_{Diss.} \tag{5.2.7}$$

The coefficients f_i defined according to Mitarai and Nakanishi (2004), are reported in the following:

$$f_1 = c(1 + 4c\eta_s \, g_o) \tag{5.2.8}$$

$$f_2 = \frac{5\pi^{0.5}}{96 \, \eta_p \, (2 - \eta_p)} \left(1 + \frac{8}{5} g_o \, c \, \eta_p \right) \left(\frac{1}{g_o} + \frac{8}{5} c \, \eta_p (3\eta_p - 2) \right) + \frac{8}{5\pi^{0.5}} \eta_p \, c^2 \, g_o \tag{5.2.9}$$

$$f_4 = \frac{25\pi^{0.5}}{16 \, \eta_p \, (41 - 33\eta_p)} \left(1 + \frac{12}{5} g_o \, c \, \eta_p \right) \left(\frac{1}{g_o} + \frac{12}{5} c \, \eta_p^2 (4\eta_p - 3) \right) + \frac{4}{\pi^{0.5}} \eta_p \, c^2 \, g_o \tag{5.2.10}$$

$$f_5 = \frac{12}{\pi^{0.5}} \, c^2 \, g_o \left(1 - e_p^2 \right) \tag{5.2.11}$$

Frictional component

According to Armanini et al. (2014) the frictional component of the stress tensors can be expressed as:

$$\tau_{21}^{fric} = \tan\varphi \, p^g \, (1 - f_o) \tag{5.2.12}$$

$$p^{fric} = p^g \, (1 - f_o) \tag{5.2.13}$$

where f_o is a suitable parameter that accounts the intermittency between the two regimes, modulating the frictional contribution. Armanini et al. (2014) assumed that f_o was a function of the Savage number $I_s = \rho_s(\dot{\gamma}d)^2/p^g$ (i.e. the square of the *inertial number* (Ancey and Evesque (2000)).
In this work we have considered two different function f_o, so that the frictional component are modulated differently accordingly as they are tangential or normal stresses:

$$\tau_{21}^{fric} = \tan\varphi\, p^g\,(1 - f_{o\tau}) \tag{5.2.14}$$
$$p^{fric} = p^g\,(1 - f_{op}) \tag{5.2.15}$$

For sake of simplicity we assume $f_{o,i}$ as functions of the particle concentration. The functions $f_{o,i}$ must be such that for $(c \to C^*)$ it is $(f_o \to 0)$, while for $(C \to 0)$ it is $(f_o \to 1)$.

An example of a simple function of this type, which seems to match the experimental data well, could be:

$$f_{o,i} = \frac{(C^* - c)^{m_i}}{\gamma_{o,i} + (C^* - c)^{m_i}} \tag{5.2.16}$$

where m_i and $\gamma_{o,i}$ are two coefficients to be assigned by comparison with experimental data.

Complete set of rheological relations

According to above equations, the complete set of rheological relations is:

$$\tau^g = \tan\varphi\, p^g\,(1 - f_{o\tau}) + \rho_s\, f_2\, \Theta^{0.5} \frac{d}{h} \frac{\partial u_1}{\partial \eta} \tag{5.2.17}$$
$$p^g = p^g\,(1 - f_{op}) + \rho_s\, f_1\, \Theta \tag{5.2.18}$$

where $\eta = x_2/h$.

Complete system of equation

By substituting the rheological relations (5.2.17) and (5.2.18) into the momentum equations (5.1.4) and (5.1.3) we have (for $f_o \neq 0$):

$$g\,h\,\sin\alpha\,f_{o\tau}\left(\int_\eta^h c\,d\eta\right) = f_2\,\Theta^{0.5}\,\frac{d}{h}\frac{\partial u_1}{\partial \eta} \tag{5.2.19}$$

$$g\,h\,\cos\alpha\,f_{op}\left(\int_\eta^h c\,d\eta\right) = f_1\Theta \tag{5.2.20}$$

$$-\frac{\partial}{\partial\eta}\left(f_4\,\Theta^{0.5}\left(\frac{d}{h}\right)^2\frac{\partial\Theta}{\partial\eta}\right) = \frac{f_2}{f_{o\tau}}\,\Theta^{0.5}\left(\frac{d}{h}\frac{\partial u_1}{\partial\eta}\right)^2 - f_5\,\Theta^{1.5} \tag{5.2.21}$$

The functions f_i for $i = 0, 5$ are defined by Eqs. (5.2.8)- (5.2.11) and by Eq. (5.2.16). The system has three unknown variables: u_1, c and Θ.

5.2.1 Approximate solution for uniform channel flow

A solution of the system (5.2.19-5.2.21) in closed form is not known. In alternative we are looking for a possible approximate solution, that will be tuned on the base of the results of the experimental investigation or the Discrete Particle Simulation.

Possible non diffusive solution

Often, in some applications of kinetic theory to granular flows the diffusive term (left term of Eq. (5.2.21)) in the collisional kinetic energy balance is neglected. In this case we obtain:

$$\frac{f_2}{f_{o\tau}}\,\Theta^{0.5}\left(\frac{d}{h}\frac{\partial u_1}{\partial\eta}\right)^2 = f_5\,\Theta^{1.5} \tag{5.2.22}$$

and by substituting Eqs. (5.2.19) and (5.2.20) into Eq. (5.2.22), we have:

$$\frac{f_{o\tau}\,f_2\,f_5}{f_1^2} = \tan^2\alpha \tag{5.2.23}$$

Eq. (5.2.23) admits a solution for a single specific concentration value. Therefore, assuming that the *production* balances the *dissipation*, it is implicitly assumed a constant value of the concentration. In this case the solution derived from the kinetic theories collapses to Bagnold's hypothesis $C = const.$
Anyway, the experimental investigation shows a variation of the concentration along the flow depth. This result leads to the conclusion that in

dry granular flows the *diffusive* component in the energy balance is not negligible.

5.3 Closure relations

Given that an approximate solution in closed form of the system presents considerable difficulties, we decided to use the results of the experimentation

From the dimensional analysis of the system (5.2.19-5.2.21) we deduce that the dimensionless groups involved in the phenomenon are:

$$\frac{U}{\sqrt{gh}} \quad ; \quad C \quad ; \quad \frac{d}{h} \quad ; \quad \tan\varphi \quad ; \quad e_p \tag{5.3.1}$$

where U and C are velocity and concentration respectively, averaged on the cross section.

Since in the experiments we have not been able to modify the particle restitution coefficient e_p and the friction angle φ, these two parameters could be introduced in the closure relations only in an arbitrary manner, so the closure relationships that we will write, will only be valid for the constant value of the two parameters, equal to that of the particles used. In addition, as most of the variables were measured in the experiments by the side wall, it is useful to distinguish between the variables averaged on the cross section and those measured on the wall.
After having performed a series of experiments in uniform flow condition (see Chapter 6), the closure relation obtained are the following.

$$C = C^* \frac{E_1}{E_1 + \alpha_{cu} \dfrac{U}{\sqrt{gh}} \dfrac{d}{h}} \tag{5.3.2}$$

$$\begin{aligned} \tau_o &= \rho_s \, C \, g \, h \, \sin\alpha = \rho_s \, C \, g \, h \, \sin\varphi \\ &= \rho_s \, g \, h \, \sin\varphi \, C^* \frac{E_1}{E_1 + \alpha_{cu} \dfrac{U}{\sqrt{gh}} \dfrac{d}{h}} \end{aligned}$$

where the coefficient E_1 has been defined according to the experimental data (see again Chapter 6).

Chapter 6

Experimental investigation

A substantial part of the thesis was done in the Hydraulic Laboratory of the University of Trento. A first part of the experimental activity was aimed primarily at the determination and calibration of the closure relations described in Chapter 5: the coefficients introduced in those relationships were calibrated on the basis of a campaign of experimental measurements conducted in a closed circuit channel able to recirculate the flow of dry granular material under steady-state conditions.

A second part of the experimental investigation was instead oriented to the verification of the results of the one-dimensional numerical simulation, and in particular the dam-break simulations.

In both situations, particular attention was paid to measuring the velocity and concentration of the solid phase. The kinematics of granular flows were recorded by cameras and at high speed with a techniques based on a new image processing method. Through image analysis, velocity and concentration profiles were measured for different motion conditions.

6.1 Experimental set-up

The experimental set-up consisted of a closed circuit system, composed of an laboratory channel with a weir at its downstream end and a feeding system able to ensure a steady flow rate of dry particles in the channel. High-speed cameras were used to record the movement of single particles in the channel.

Laboratory Channel

The laboratory channel is an free surface channel, made up of transparent perspex plates with a thickness of 1 mm. It is equipped with a piston that allows to give t the channel an adjustable slope up to more than 30°. The width of the channel is 10 cm.
The first set of experiments, conducted under steady and homogeneous flow conditions, was aimed at the calibration of the closure relations. The stationary flow was obtained through a recirculation system consisting of a feed hopper equipped with an opening through which the flow was controlled. The scheme is reproduced in Fig. 6.1.
Regarding the dam break test, performed in order to have a compari-

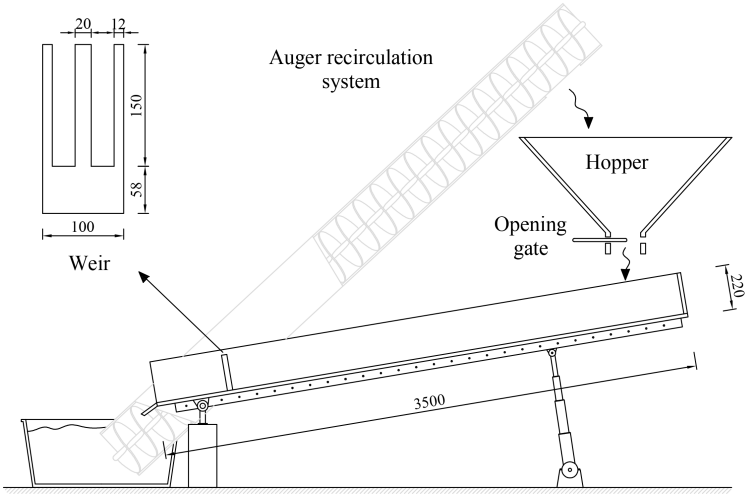

Figure 6.1: *Channel scheme for uniform flow condition*

son with the numerical test (Chapter 7), a volume of particle is retained through a removable gate (Fig. 6.2), positioned upwards in the channel.
The material coming out from the canal is collected in a collecting box with an opening on the bottom, at the end of which was placed an auger, capable of rising the material up to the entrance from the upper hopper.

The auger is 5 m long and has a diameter of 40. The number of the auger laps is adjustable, according to the flow rate desired.

The tests of the dam-break are carried out in the same channel, but in this case a certain volume of granular material was accumulated upstream of a removable gate located normally to the bottom of the channel (Fig. 6.2)

The gate is pulled-up abruptly in such a way as to cause the almost instantaneous collapse of the material heaped upstream of it.

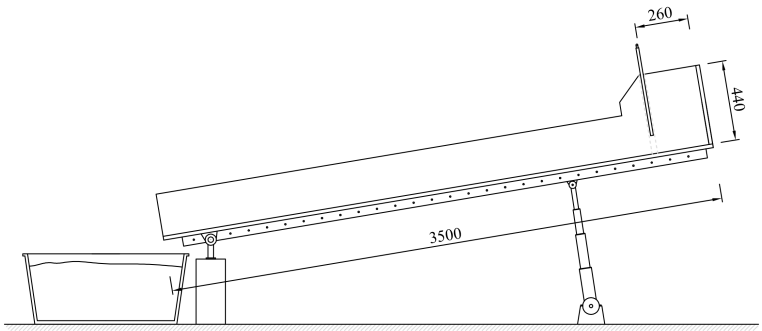

Figure 6.2: *Channel scheme for the dam-break test*

Granular material

The granular material used in the experiments consists of unexpanded polystyrene spheres (Fig. 6.3), with diameter $d_p = 0.075 \pm 0.005$ mm and a density $\rho_s = 1035 \pm 10$ Kg / m^3.

The inelastic coefficient of restitution of the particles is measured experimentally, by dropping a particle from a certain height on a perspex surface and measuring the maximum rebound hight. Thus the value $e_p = 0.91 \pm 0.01$ is obtained.

The measure of the friction angle of the particle is more problematic, since we have observed that it depends on the modalities with which it is obtained (see Chapter 6, section 6.3.2, last paragraph). In general, it ranges around 21 ± 5^o.

Recording method

Once the material is flowing along the channel, the particles displacement and velocities have been recorded through high speed cameras FASTCAM X 1024 PCI by PHOTRON. The cameras are able to record 1000 frames per second at a maximum resolution of 1024x1024 pixels; by reducing the resolution the maximum velocity available is 109000 fps. The frame rate has been chosen so that the particle displacement in two subsequent frames do not exceed the particle radius. This choice is due to the optical method adopted (described in the following sections), that needs a displacement of the particles smaller than a radius to follow their trajectories.
Fig. 6.4 shows the position of the lateral camera, perpendicular to the wall of the channel with a headlight in order to have a good lighting of the particles.

Figure 6.3: *Particles of polystyrene used in the experimental test*

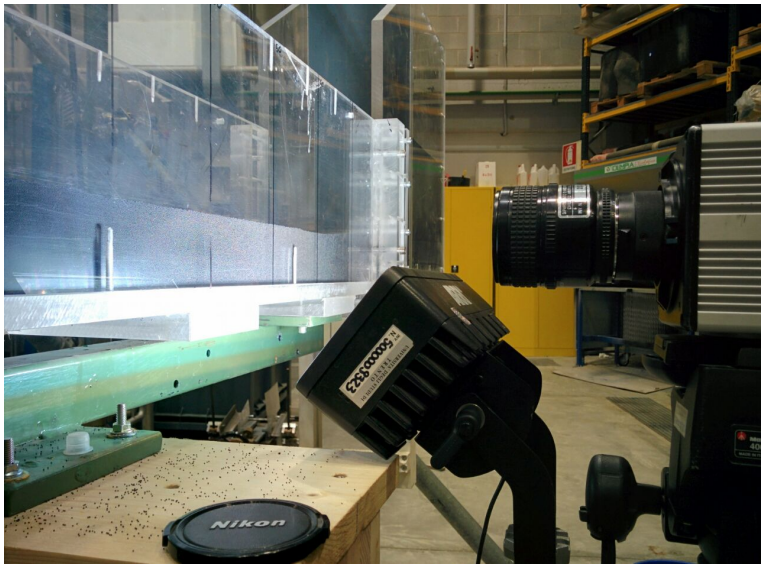

Figure 6.4: *Camera and headlight positioned laterally to the channel*

6.2 Measurements techniques

In the following section, the optical method developed to measure the concentration and velocity of the particles is presented.

6.2.1 Particles detection

The first step to be performed is the identification of the particles. First of all, the Region Of Interest (ROI) of the images is selected, and the image is cropped accordingly. This allow us to exclude non representative zones (e.g. broken particles).
Next, each image should be adaptively equalized, de-noised and filtered. This is performed in three different steps as shown in Fig. 6.5(a,b,c):

- Adaptive histogram equalization is applied to the image. This technique is used to improve contrast in images. It differs from ordinary histogram equalization in the sense that the adaptive method computes several histograms, each corresponding to a distinct section of the image, and uses them to redistribute the lightness values of the image. It is therefore suitable for improving the local contrast and enhancing the definitions of edges in each region of an image. This is performed using the CLAHE technique (Pizer et al., 1987).

- A de-noising operation is applied on the image using the non-local means de-noising technique (Buades et al., 2011).

- A bilateral filter operation is then applied to smooth the image (Tomasi and Manduchi, 1998). A bilateral filter is a non-linear, edge-preserving, and noise-reducing smoothing filter for images. It replaces the intensity of each pixel with a weighted average of intensity values from nearby pixels.

Otsu thresholding (Otsu, 1979) is then applied to obtain a binary mask, as the one shown in Fig. 6.5(d); from this last type of image it will be possible to detect the position of the particles. Otsu thresholding is used to automatically perform clustering-based image thresholding, or, the reduction of a gray level image to a binary image. The algorithm assumes that the image contains two classes of pixels following bi-modal histogram (foreground pixels and background pixels). It then calculates the optimum threshold separating the two classes so that their combined spread (intra-class variance) is minimal, or equivalently (because the sum of pairwise squared distances is constant), so that their inter-class variance is maximal.

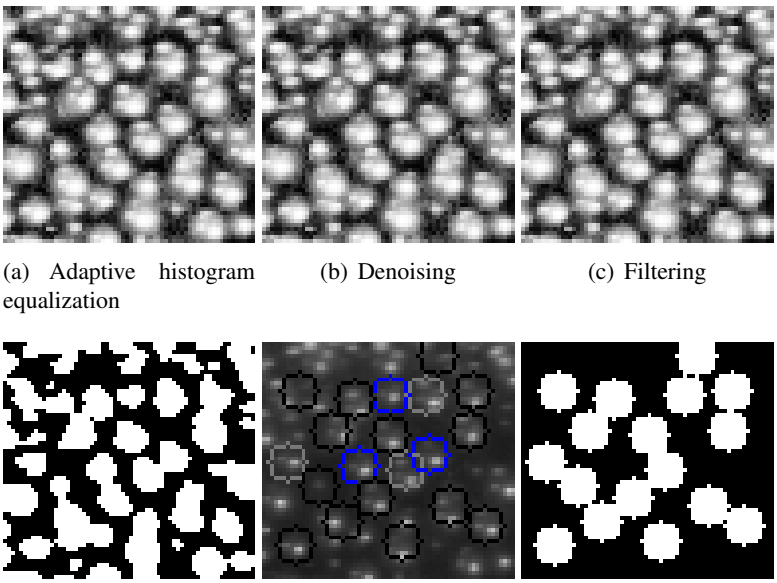

(a) Adaptive histogram equalization (b) Denoising (c) Filtering

(d) Binary mask (e) Detected balls (f) New image

Figure 6.5

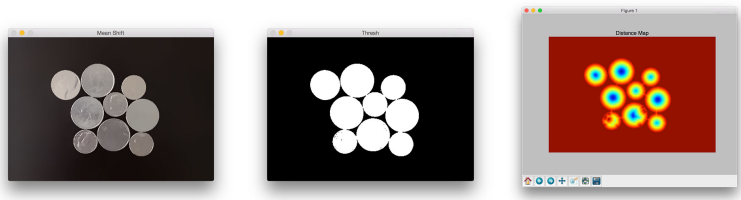

(a) Filtered image (b) Binary mask (c) Watershed visualization

Figure 6.6: *Example of the application of the watershed algorithm to detect coins.*

The watershed algorithm (Meyer, 1992) is then applied on the binary mask obtained. The watershed algorithm is a classic algorithm used for segmentation and is especially useful when extracting touching or overlapping objects in images, such as the particle or the coins in 6.6. The first step in applying the watershed algorithm for segmentation is to compute the Euclidean Distance Transform (EDT). As the name suggests, this function computes the Euclidean distance to the closest zero (i.e., background pixel) for each of the foreground pixels. A peak is defined as a point that maximize the average distance from zeros in the image. The intensity of the peak is defined as the average distance from zeros in the image. The algorithm allows to set the minimum distance between two peaks. If the algorithm detects two or more peaks with the same intensity at a lesser distance with respect to the minimum, it will output both of them. The watershed algorithm returns a matrix of labels, an array with the same width and height as our input image. Each pixel value has a unique label value. Pixels that have the same label value belong to the same object.
Ideally there should be a label for each of the particles in the image. However, this is not the case, since our images are much more noisier and present a much greater deal of occlusions with respect to the coins example.
We define c_1 and c_2 as the centers of two particles, being (x_1, y_1) and (x_2, y_2) their pixel coordinates. We know that the particle are spheres and we know their diameters d and radius r in pixel dimensions in the image. We define the distance between the center of two balls as the Euclidean distance d:

$$d(c_1, c_2) = \sqrt{(x_2 - x_1)^2 + (y_2 - y_1)^2} \tag{6.2.1}$$

If two centers are at a distance lesser than the radius, a new center c_3 will be initialized in the midpoint and the centers c_1 and c_2 will be discarded from the set of centers C_0.

$$d(c_1, c_2) < r, \qquad c_3 = (\frac{(x_2 + x_1)}{2}, \frac{(y_2 + y_1)}{2}) \tag{6.2.2}$$

We check if particles overlap with each other. We define overlapping particles as two particles whose centers c_1 and c_2 respect the following condition

$$r < d(c_1, c_2) < 2r \tag{6.2.3}$$

If a particle overlaps with more than 3 other particles, the particle is discarded. If a particle present overlapping parts with one or two other particles, it is listed as a *weak match*. If a particle doesn't overlap, it is

listed as a *strong match*.
After the detection step has been performed, each image has a set of *weak matches* and a set of *strong matches*. To determine if the *weak matches* are real particles or not, we exploit the correlation between set of consecutive frames. Let's take two consecutive frames, F_1 and F_2, with their sets of *strong matches*, S_1 and S_2, and *weak matches*, W_1 and W_2. Let's take a strong match $s_i \in S_1$ and a weak match $w_j \in W_2$, we move weak matches to strong matches array if they satisfy the following condition:

$$\textit{if } d(s_i, w_j) < r \textit{ then } w_j \in S_2 \tag{6.2.4}$$

At the opposite, we discard weak matches that satisfy the following condition:

$$\textit{if } d(s_i, w_j) > r, \forall s_i \in S_1 \textit{ then } w_j \textit{ is discarded} \tag{6.2.5}$$

After this operation has been performed on all the consecutive frames, we produce an equivalent image for each frame which will be used to compute the density and velocities of balls at later stages.

Set distance method

With this settings we simply plot a circle with radius r centered on each point present in the *strong matches* array.

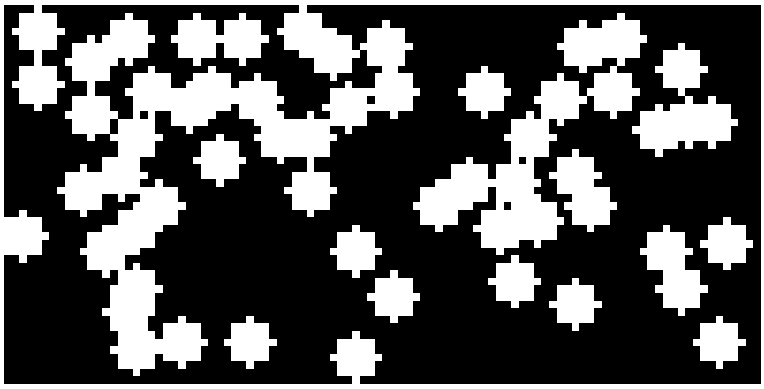

(a)

Figure 6.7: *Example of the application of the "set distance" pipeline.*

Grey balls method

With this settings we plot a circle with radius r centered on each point present in the *strong matches* array, in two possible colors. If two *strong matches*, $s_1 \in S_1$ and $s_2 \in S_1$, satisfy the following condition, they will be represented in grey:

$$d(s_1, s_2) < 2r - offset \tag{6.2.6}$$

where the $offset$ variable can be manually set (recommended value $20\%\, r$). In this way we will be able to assign a different weight to particles of different colors when computing the concentration; in particular the grey balls have a lower contribution to the concentration, since they have a superposition with other particles and could not belong all to the same 2D plane.

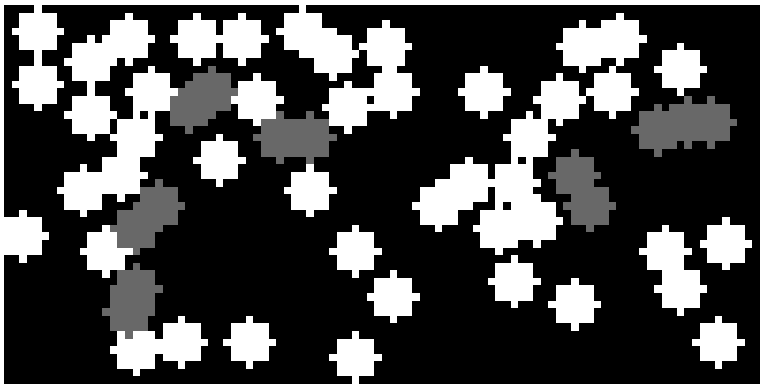

(a)

Figure 6.8: *Example of the application of the "gray balls" pipeline.*

6.2.2 2D concentration

Firstly we are interested in computing both the instantaneous and average 2D concentration of each layer. The user can set how many layers the image will divided in (along the y axis). In order to compute the 2D concentration, the aim is to exclude from the analysis all the particle in the background (considering as background everything distant more than $d/2$ from the wall).

Set distance

Let's define the number of white pixels in a layer n_w, the number of black pixels in a layer n_b and the total number of pixels in a layer $n_{tot} = n_w + n_b$, the concentration C_i of layer i is computed as

$$C_i = n_w / n_{tot} \tag{6.2.7}$$

Grey balls

Let's define the number of white pixels in a layer n_w, the number of black pixels in a layer n_b, the number of grey pixels in a layer n_g and the total number of pixels in a layer $n_{tot} = n_w + n_b + n_g$, the concentration C_i of layer i is computed as

$$C_i = \frac{n_w + W_g * n_g}{n_{tot}} \tag{6.2.8}$$

where W_g is the weight to be given to the gray pixels that can be manually set.

6.2.3 3D concentration

We are then interested in the 3D concentration, which is linked through simple geometrical considerations to the 2D concentration.
Let us assume a mono-dispersed granular material with a diameter d of the particles and s the average distance between particles.
In this conditions, the following relation is valid:

$$C_{2D} = \gamma \frac{d^2}{(d+s)^2} \tag{6.2.9}$$

That is, the 2D concentration is proportional through a coefficient γ to the ratio of the particles area and the area considering the voids among them. When the particles are all at contact ($s = 0$), the concentration assumes the close packing value, here indicated as C^*_{2D}. This means that the coefficient γ is equal to C^*:

$$C^*_{2D} = \gamma \frac{d^2}{d^2} = \gamma \tag{6.2.10}$$

According to Eq. (6.2.10), we may write:

$$C_{2D} = C^*_{2D} \frac{d^2}{(d+s)^2} \tag{6.2.11}$$

That is:

$$\frac{d}{(d+s)} = \left(\frac{C_{2D}}{C^*_{2D}}\right)^{\frac{1}{2}} \tag{6.2.12}$$

If we consider the 3D concentration, similarly for the 2D case, the following relation may be applied:

$$C_{3D} = \gamma_{3D}\frac{d^3}{(d+s)^3} \tag{6.2.13}$$

Now the 3D concentration is proportional through a coefficient γ_{3D} to the ratio of the particles volume to the volumed accounting for the voids. Clearly, as before, when $s = 0$, the concentration assumes the close packing value C^*_{3D}, so that $\gamma_{3D} = C^*_{3D}$. Finally, substituting Eq. (6.2.12) in Eq. (6.2.13), the 3D concentration may be computed, starting from the 2D value, with the following relation:

$$C_{3D} = C^*_{3D}\left[\left(\frac{C_{2D}}{C^*_{2D}}\right)^{\frac{1}{2}}\right]^3 \tag{6.2.14}$$

In our experiments, the particles are spherical, so that the following values may be considered:

$$C^*_{3D} = 0.74 \qquad \text{and} \qquad C^*_{2D} = 0.906 \tag{6.2.15}$$

where the 3D value of close packing is referred to spheres and the 2D value to disks (projection of a sphere in two dimensions).

6.2.4 Velocity: particles detection and optical flow

The second quantity we are interested in is the velocity of the particles. By measuring the velocity directly from the displacement of the particles between one image and the following, the measurement error of the particle center position during the detection procedure is of ± 1 pixel (this is a limit of the method itself). Furthermore, as said before, when there are two neighboring light peaks (their distance minor that a particle diameter), the program consider a *new* particle positioned in the midpoint between the two. However the two peaks may represent two particles, one in the foreground and one in the background; regarding the concentration, this approach may be correct (only one particle is in the foreground). However, the position of the particle is incorrect and leads to a non-negligible mistake in the computation of the velocity. For these reasons the velocity has been computed through another method.
We used the *good features to track* algorithm (Shi et al., 1994) to extract

the features in the image; then the optical flow technique developed by Bouguet (2001) is employed to track the detected features (see Fig. 6.9). Subsequently, the single particle velocity is assumed to be the velocity

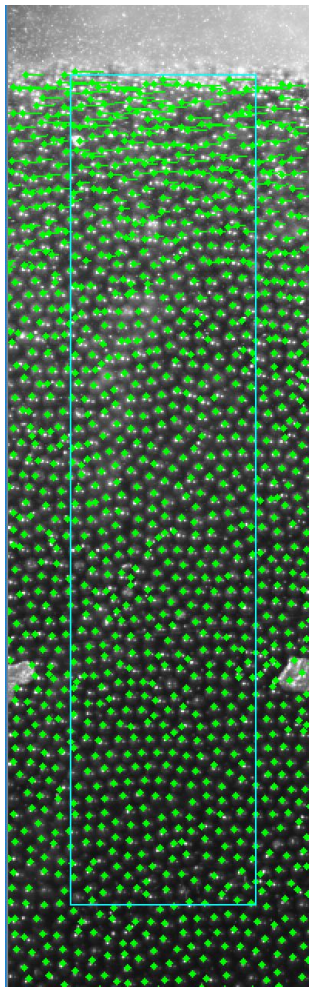

Figure 6.9: *Optical method to measure the velocity: tracking of good feature*

of the features that belong to the pixels constituting that particle.

6.3 Experimental results

We report and interpret in the following the results of the experimental investigation. Firstly, the results of the uniform flow used to calibrate

the closure relations are described in detail. Then the dam break test is described and some flow features have been measured in order to compare the results with the numerical solution (see Chapter 7).

6.3.1 Uniform flow conditions

In this section we present the experiments conducted in a rectangular prismatic open channel in statistically stationary and homogeneous condition (uniform channel flow) on mobile bed. The experimental configuration is represented in Fig. 6.10.
The flow rate is introduced from the hopper (as explained in Fig. 6.1)

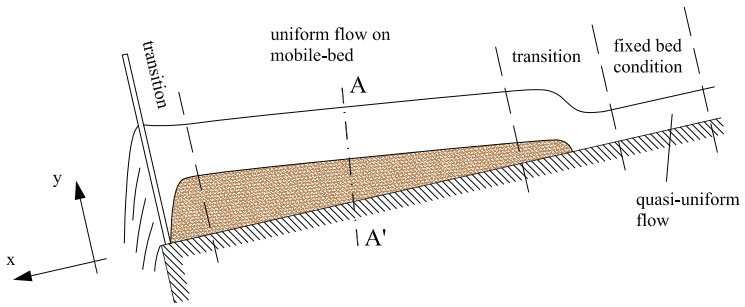

Figure 6.10: *Mobile bed scheme adopted to obtain uniform flow condition*

and in the first part of the channel the granular material flows over a fixed bed. A gate with double slits is posed at the end of the channel in order to slow the flow and to create a deposit behind the gate. So, the particles start to flow on a mobile bed.
In a mobile bed granular flows (both dry and submerged in water) it is possible to demonstrate that in a statistically stationary prismatic channel flow, the only possible solution is the homogeneous one (Armanini, 2015; Jansen et al., 1994). The validity of this condition has been checked in Meninno (2015) and in Meninno et al. (2018). In particular, the homogeneous condition in the configuration of Fig. 6.10 is estabilished for a long part of the channel (Meninno, 2015). Section AA' in Fig. 6.10 is situated at the center of this zone characterized by uniform flow and corresponds to the measurements section.
The double slits gate is shown in Fig. 6.11 The section of the channel is shown in Fig. 6.12; it is 10 cm width and 20 cm height. The wall of perspex is 1.5 cm wide.

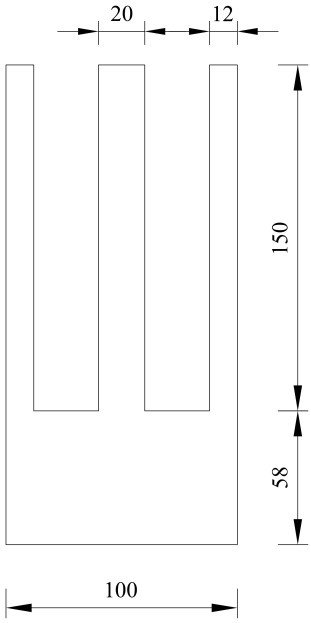

Figure 6.11: *Downstream gate with double slits*

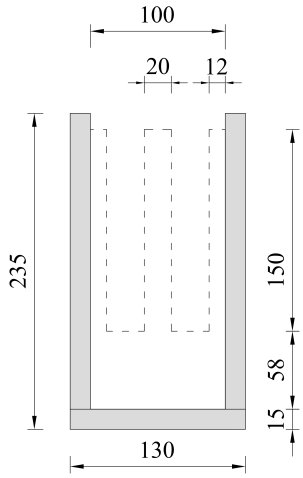

Figure 6.12: *Channel section*

Velocity profiles

The first flow parameter analyzed is the velocity vertical profile, both in the longitudinal and normal direction, with respect to the free surface. The cameras recording frequency has been adjusted according to the different velocity of the flow. As said before, the frame rate should be high enough so that the particles do not move more than a radius in two consecutive frames.
The images recorded have been analyzed through the optical method described in the previous section. In particular each image has been divided in a certain number of layers; the output of the image processing shows the velocity profiles in which each experimental point corresponds to a layer of 2 particles diameters thick.
The instantaneous velocity of each single layer is computed as the average of the velocity of the particles contained in that layer:

$$U_i, t_j = \frac{\sum_1^{n_P} u_p}{n_P} \tag{6.3.1}$$

where i is the i-th layer, t_j the instant in which the velocity is computed (between image $j-1$ and image j), u_P the single particle velocity and n_P the number of particles contained in that layer. Then the final velocity profile is obtained by averaging on all the images (corresponding to about 3 s):

$$U_i = \frac{\sum_1^{n_t} U_i, t_j}{n_t} \tag{6.3.2}$$

where n_t is the number of frames and U_i is the averaged velocity on all frames.
Fig. 6.13 shows the profiles of the longitudinal velocity for different dimensionless flow rates Q^*. The flow rate is made dimensionless according to Eq. (6.3.3) (Taberlet et al., 2003):

$$Q^* = \frac{Q}{B\, d\, \sqrt{gd}} \tag{6.3.3}$$

where B is the channel width, d the particles diameter and g the gravity acceleration. Furthermore, on the vertical axes a dimensionless quantity $(y - y_{surf})/h$ is considered, where y_{surf} is the y coordinate of the free surface and h is the flow depth. In particular, the flow depth has been computed as the height where the flow velocity falls down the 0.1% of the maximum value.
Fig. 6.13 shows the longitudinal velocity profiles, while Fig. 6.14 shows the normal to velocity profiles. Clearly, for higher normalized flow rates, the longitudinal velocity increases and the profile assume a greater

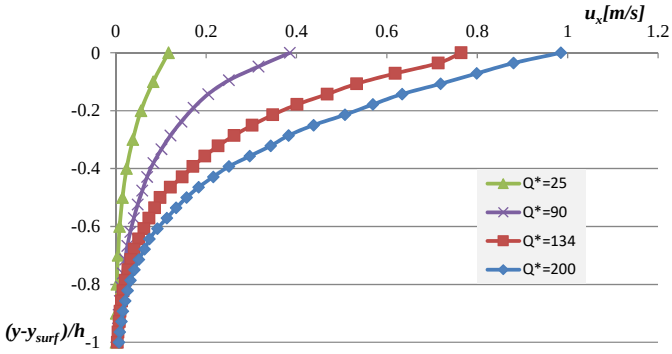

Figure 6.13: *Longitudinal velocity profiles for different dimensionless flow rates*

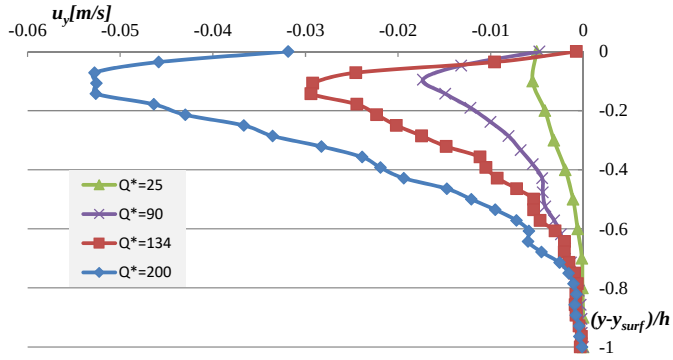

Figure 6.14: *Normal velocity profiles for different dimensionless flow rates*

curvature. Regarding the normal component of velocity, as pointed out in Chapter 2, it is not zero due to possible diffusive terms or secondary circulations. In particular, for higher flow rates this component increases: our hypothesis is that at higher flow rate the collisional component is predominant in the upper layer, and the diffusive term rising from the lack of scale separation increases.
This hypothesis is supported by the granular temperature profile, shown in Fig. 6.15 for different flow rate. It is defined as:

$$T = \frac{u_x'^2 + u_y'^2}{2} \tag{6.3.4}$$

where u' indicates the fluctuating velocity component, that is the difference between the instantaneous value at time t, u_t, and the average velocity U:

$$u' = u_t - U \tag{6.3.5}$$

Fig. 6.15 clearly shows that the fluctuations, reasonably due to collisions

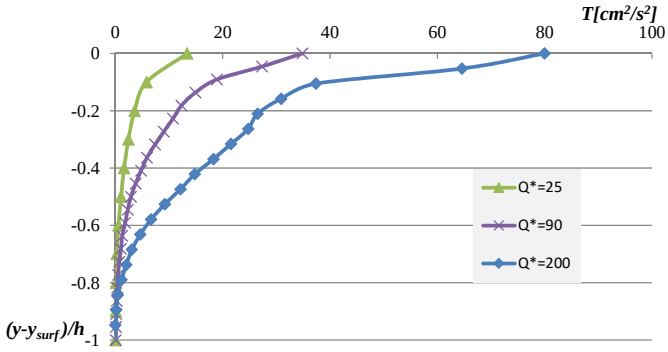

Figure 6.15: *Granular temperature for different dimensionless flow rates*

among particles, increase at increasing flow rates. This indicates that the collisional region becomes wider as the flow rate increases.

Concentration profiles

The concentration has been measured starting from the image processing according to the optical method (grey balls approach in particular). In Fig. 6.16 we represent an example of an image processed with the grey balls method. The grey particles are those over-lied with other particles with more than 3 pixels; their contribution to the concentration reduces with the parameter W_g (see Eq. (6.2.8)), which has been set to 0.8. In the upper part the concentration is lower and it increases towards the lower layers. Clearly in the upper layers we expect more *grey balls*, since the concentration is lower and more particles in the backgrounds become visible and may overlap with those in the foreground.
Starting from this type of images, the profiles presented in Fig. 6.17 are obtained. In particular, we may observe that for higher dimensionless flow rates, the concentration has a different behavior: the layer in which the concentration tends to reach its maximum values is lower for higher concentration. This can be explained through the granular temperature T shown in Fig. 6.15: the region in which the gradient of the concentration is higher correspond to the region of the higher granular temperature. This means that the strong gradient in concentration is reasonably due to the collisional contribution.
The relative dispersion of concentration values in the lower part is reasonably affected by the presence of the wall, which induces contact forces on the particles different than those between particles themselves. It is worth noticing that the flow depth average concentration is changing for different dimensionless flow rates: this aspect has been analyzed in depth in order to calibrate the closure relations.

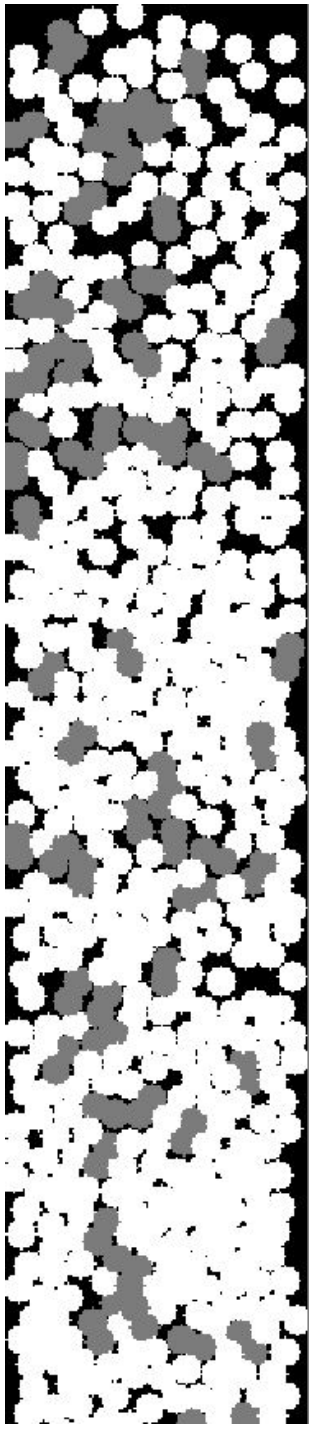

Figure 6.16: *Example of the output of the optical approach for a single frame: grey balls method*

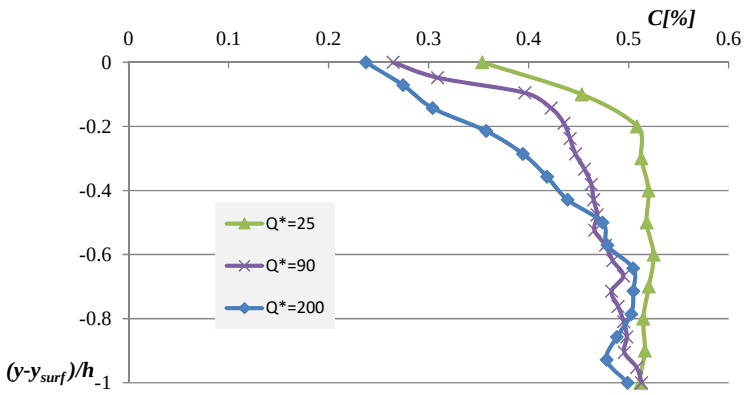

Figure 6.17: *Example of the output of the optical approach for a single frame: grey balls method*

6.3.2 Calibration of the closure relations

In order to proper define the closure relations presented in Chapter 5, a set of experimental data has been analyzed. For 16 tests in uniform channel flow, conducted at different flow rates and with different slopes of the channel, the wall averaged value of the velocity and concentration have been computed, starting from the profiles described in the previous section.
The values computed are defined as *wall* values (h_w and C_w), since they are based on the measurements done on the channel wall (see Chapter 6). In order to obtain the areal average values (h and C), necessary to calibrate the closure relations, the wall values are multiplied by corrective factors that take into account the ratio between the wall values and the areal averaged values. These coefficients have been computed in Chapter 3.

I closure relation

The first closure relation is a formulation of the areal averaged concentration as a function of F_r and d/h. In order to define this relation, two main analysis have been done: first of all it has been evaluated the influence of the ratio h/d on the concentration C (in the graphs we have directly represented the areal averaged values).
A fitting curve (dashed light blu line in Fig. 6.18) has been found in order to impose that for $h/d \to 0$ the average concentration $C \to C_*$ (Fig. 6.18). That is, when the flow stops, it is characterized by the maximum random packing concentration C_*. The fitting curve is defined by the

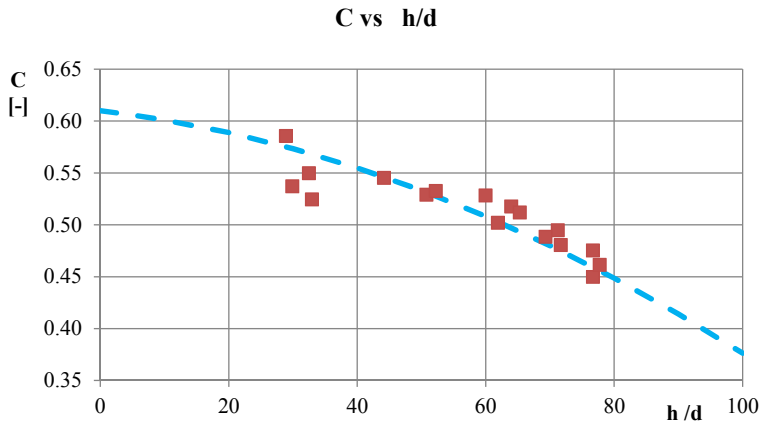

Figure 6.18: *Concentration as a function of h/d: experimental data and fitting curve (dashed blu line)*

following equation:

$$C = 0.61 - 0.00074\frac{h}{d} - 0.000015\left(\frac{h}{d}\right)^2 \tag{6.3.6}$$

The coefficients have been determined in order to obtain the best fitting of the experimental data.

The second empirical relation is between $Q_*\dfrac{d}{h} = Q/(Bh\sqrt{gd})$ and C. The term Q_* stands for the dimensionless flow rate (Eq. (6.3.3)).
Fig. 6.19 shows the experimental results.
So we may write:

$$F_1 = 0.01 - 0.0113\,C \tag{6.3.7}$$

By combining Eq. (6.3.3) and Eq. (6.3.7), we obtain the following expression for the flow rate:

$$Q = F_1 B\,h\sqrt{gh}\frac{h}{d} = 0.0163Bh\sqrt{gh}\frac{h}{d}(C^* - 0.0693\,C) \tag{6.3.8}$$

In the end we want to express C as a function of U and h. We have that:

$$U = \frac{Q}{\alpha_{cu}\,h\,C\,B} = \frac{0.0163\,\sqrt{g\,h}\,B\,h\,\dfrac{h}{d}\,(C^* - 0.693\,C)}{\alpha_{cu}\,h\,C\,B} \tag{6.3.9}$$

and

$$U = \frac{0.0163\,\sqrt{g\,h}\,\dfrac{h}{d}\,(C^* - 0.693\,C)}{\alpha_{cu}\,C} \tag{6.3.10}$$

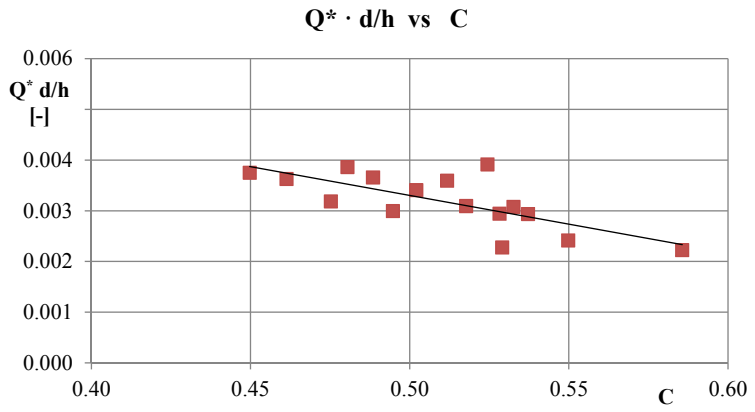

Figure 6.19: *Dimensionless flow rate versus C: experimental data and interpolation*

By explicating C from the previous equation, we obtain:

$$C = C^* \frac{0.0163}{0.0011 + \dfrac{\alpha_{cu}\, U}{\sqrt{gh}} \dfrac{d}{h}} \tag{6.3.11}$$

Since for $U \to 0$, we expect that $C \to C^*$ (and $C \to C^*$), we rewrite Eq. (6.3.11) as follows:

$$C = C^* \frac{E_1}{E_1 + \alpha_{cu} \dfrac{U}{\sqrt{gh}} \dfrac{d}{h}} \tag{6.3.12}$$

Fig. 6.20 show that the value 0.025 for the coefficient E_1 makes Eq. (6.3.12) best fitting the experimental data, which are represented together with the curve derived from the final closure relation. From Eq. (6.3.12) we obtain the following expression for the velocity:

$$U = \frac{1}{\alpha_{cu}} \sqrt{gh} \frac{h}{d} \frac{C^* - C}{C} E_1 \tag{6.3.13}$$

From which the discharge results:

$$\begin{aligned} Q &= \alpha_{cu}\, h\, C\, B\, U \\ &= h\, B\, \sqrt{gh} \frac{h}{d} (C^* - C)\, E_1 \end{aligned} \tag{6.3.14}$$

In order to verify the effectiveness of the closure relation, we have compared the flow rate measured from the experiments (Q_{data}) and that computed according to Eq. (6.3.14) (Q_{cl})in Fig. 6.21. The agreement is quite good since all the points result to be almost on the bisector.

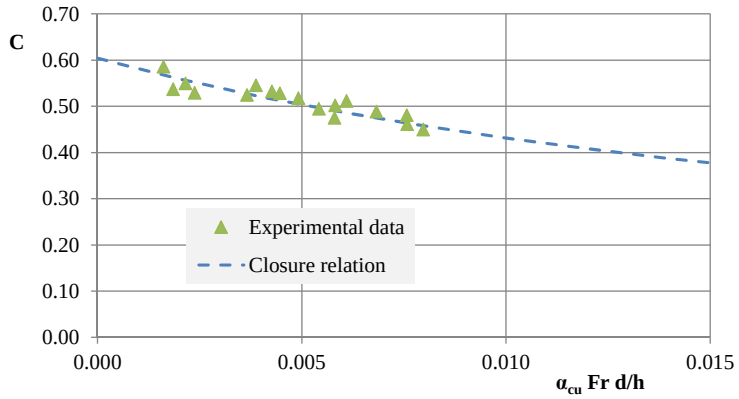

Figure 6.20: *Comparison between C computed with Eq. (6.3.12) and experimental data.*

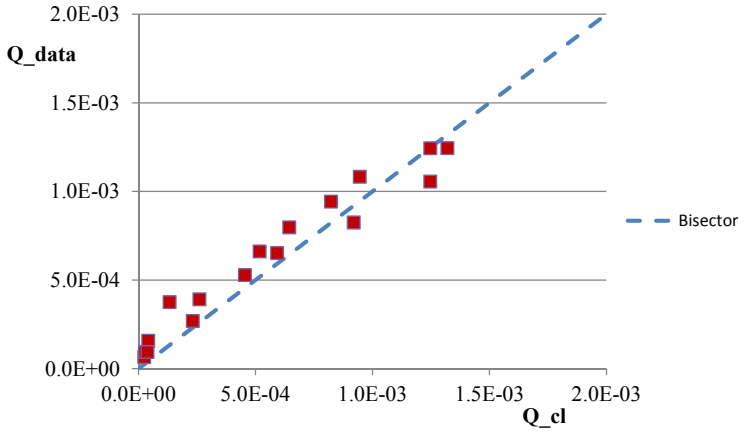

Figure 6.21: *Comparison between Q_{cl} computed through the closure relation* (6.3.14) *and Q_{data} derived experimentally*

II closure relation

Regarding the second closure relation for τ_0, by substituting the relation of the concentration, we obtain:

$$\begin{aligned} \tau_o &= \rho_s\, C\, g\, h\, \sin\alpha = \rho_s\, C\, g\, h\, \sin\varphi \\ &= \rho_s\, g\, h\, \sin\varphi\, C^* \frac{E_1}{E_1 + \alpha_{cu} \dfrac{U}{\sqrt{gh}} \dfrac{d}{h}} \end{aligned}$$

in which we have calculated the concentration according to Eq.(6.3.12).

Closure relation for coefficient α_{cu} and friction angle φ

For each experiment we have computed the coefficient α_{cu}; it varies in a quite small range of values (standard deviation $\sigma = 0.055$), so we have decided to consider it constant and equal to the average value with respect to all the experiments:

$$\alpha_{cu} = 0.663 \tag{6.3.15}$$

Furthermore, for lower Froude number the coefficient tends to 1: when the material is at rest in fact $\alpha_{cu} = 1$, while for higher Froude it tends to the asymptotic value of 0.663 (Fig. 6.22).
Regarding the friction angle φ, it has been measured the repose angle of

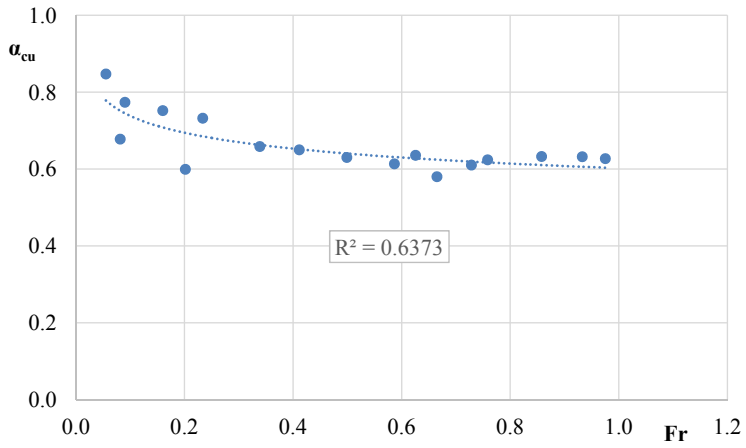

Figure 6.22: *Coefficient α_{cu} VS Fr.*

the material used during the experimental test. It is about 21 ± 5^o. This great variability of the repose angle is due to the fact that it depends on the maximum packing fraction of the material at rest. We observed that if we consider a dam break test, the flow is little agitated, the random packing concentration is not so high and the friction angle reaches 16^o (assuming as the friction angle the slope of the final configuration of the free surface, at the end of the test). Contrary, in a continuous uniform flow where the material is much more agitated and continues to flow, the deposit reaches a very high random packing concentration and the friction angle is about 26^o (in this configuration we assume as the friction angle the slope of the bed elevation). An intermediate situation is when

a bucket of granular material is upset in a confined area: the material is more agitated than in the dam break test but less then in the uniform flow in an inclined channel and assumes a friction angle of 21 ± 1^o.

6.3.3 Dam break test

The dam break test has been conducted according to Fig. 6.2. In the upstream part of the channel a gate has been positioned, so that on the right side a certain volume of material can be stored. Along all the channel it has been placed a mobile bed of dry particles 5 cm height. This allow us to evaluate the possible erosion phenomenon. The slope of the channel has been settled to 0^o (horizontal dam-break).
The variables we have computed during the experiment are the velocity of the flow in the section just after the removable gate, the bed erosion and, finally, the deposit slope. In order to analyze the velocities, a camera has been positioned just after the gate. Anyway, the dimension of the area recorded are not big enough to record the whole experiment: in order to have a good enough resolution, a window of a maximum height of 6 cm has been chosen. For this reason the flow is registered till the flow depth exceeds 6 cm.
The deposit upstream of the gate is 20 cm height and the gate is manually opened from the top. We performed some experiments by extracting the gate from the bottom of the channel, but in this way the particles fall from the top of the deposit on the mobile bed and the dynamic of the phenomenon is not that of a real dam-break.
Fig. 6.23 show the final deposit profile of the material at rest. The de-

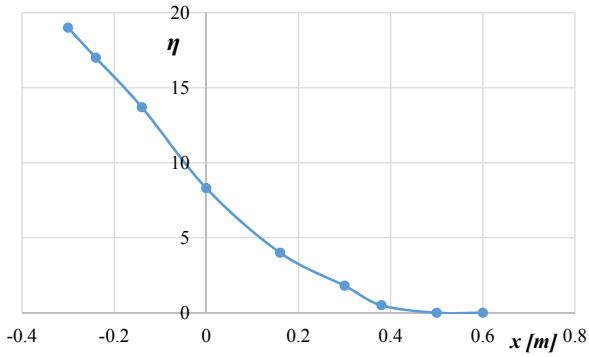

Figure 6.23: *Free surface η of the deposit at the end of the simulation. The zero x-coordinate corresponds to the gate location*

posit starts at 40 cm downstream of the gate and its average slope is about 16^o.
Regarding the velocity just after the gate, in Fig. 6.24 the velocity profile is represented for different instants. Each dt correspond to an interval of $7e^{-3}$ s.

In order to observe the bed erosion, in Fig. 6.25 a zoom of the velocity

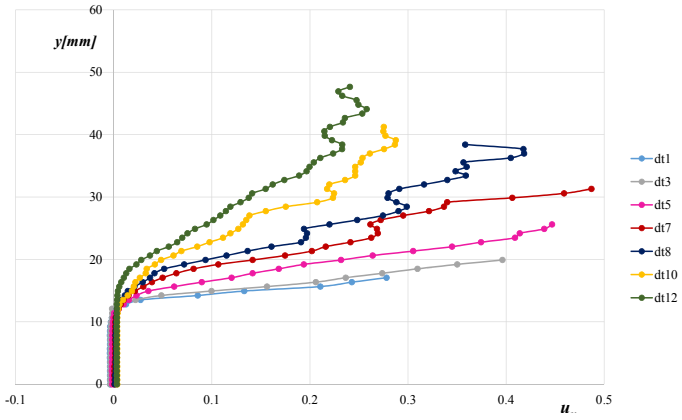

Figure 6.24: *Velocity profiles just after the gate*

profiles near the mobile bed (black continuous line) has been reported. As it can be observed, the velocities under the mobile bed limit are negligible, and a maximum erosion of 1 mm may be considered. Anyway the velocity is not exactly zero, but it tends asymptotically to zero. It is worth noticing that in the 1D model the velocity is a depth integrated velocity. Due to the asymptotic behavior of the velocity towards the bed and to the high gradients of its profiles, the depth averaged experimental value is very sensitive to the definition of the bed location, which consequently is very uncertain. For these reasons the results of the numerical simulations will show even strong differences in the bed erosion process (see Chapter 7).

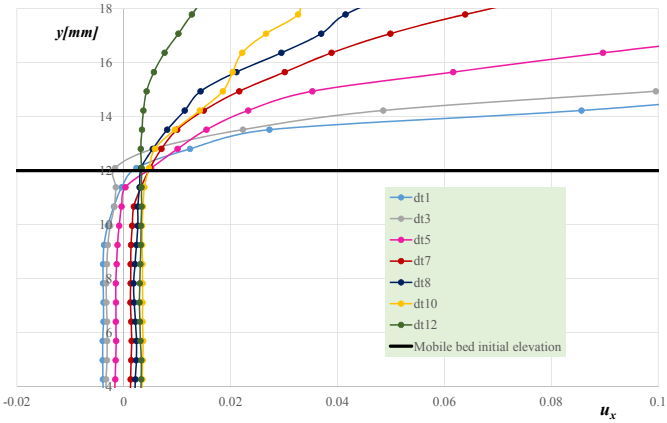

Figure 6.25: *Velocity profiles in different instant (dt=0.01 s). The black line indicates the initial elevation of the mobile bed.*

Chapter 7

Numerical solution

In this chapter a new path-conservative SPH (Smooth particles Hydrodynamic) approach will be presented. It has been developed to solve two-phase mathematical model and its effectiveness has been demonstrated on standard test cases (Riemann problems and a priori known solution of Pitman & Le model or Shallow water equations).
However, this new approach has been not yet applied to the mathematical model developed in the thesis: for simplicity the solution of this model has been developed through a path-conservative Finite Volume Method, with the aim to apply in the future the SPH scheme. Some numerical results obtained with the FVM regarding the mathematical scheme for dry granular flows will be presented too.

7.1 New path-conservative SPH approach

Smoothed Particle Hydrodynamics (SPH) is a meshless Lagrangian method, originally developed by Lucy (1977) and Gingold and Monaghan (1977) for computational astrophysics, and then extended to free surface flows, multiphase problems and solid mechanics. Its meshless particle nature makes it suitable for problems characterized by large deformations and moving boundaries. The SPH approach has been successfully adopted in several fields: for compressible flows (Cummins and Rudman., 1999) and incompressible or weakly compressible flows (J.P. Morris and Zhu, 1997; Monaghan and Gingold, 1989, 1983), free-surface flows (Monaghan, 1994; Colagrossi and Landrini, 2003; Ferrari et al., 2009), multi-phase flows (Welton, 1997; H.A. Posch and Kum, 1995; O. Kum and Posch, 2007; Monaghan and Kocharyan, 1995) and solid mechanics (Campbell, 2000).
In the SPH framework, the continuum is discretized through a finite num-

ber of points called particles; from a mathematical point of view, the particles are interpolation points, while from a physical point of view they are material particles, associated to physical properties such as mass, density, pressure and velocity. The particle nature of SPH also mimics the underlying molecular structure of matter. The standard SPH method (Monaghan, 2005) is usually stabilized with the aid of artificial viscosity, which requires the careful calibration of several parameters.

Many improvements have been applied to the SPH method until now, for example in order to solve the problems related to particle penetration and tensile instability of the original SPH formulation. The latter is an unphysical clustering of the particles, caused by negative pressures. For that purpose, the XSPH method was introduced in Monaghan and Gingold (1989), distinguishing between the velocity of a particle computed from the momentum equation and the one used to update the particle position. This allows to prevent unphysical particle penetration, but does not solve the problem of tensile-instability. Monaghan (2000) proposed the introduction of an artificial stress (artificial pressure) to remove this type of instability; however, all these methods lead to further additional parameters to calibrate.

A more recent approach introduced by Vila and Ben Moussa (B. Ben Moussa and Vila, 1999; Vila, 1999; Moussa, 2006) does not need any artificial viscosity to stabilize the numerical solution: the fluxes between SPH particles are computed at the aid of *Riemann solvers* that are well-known from the finite volume context, so that the intrinsic numerical viscosity of the Riemann solver replaces the artificial viscosity of the original SPH scheme.

We use this last formulation, by introducing two changes: a *flux-difference* form is adopted, by adding a new term that gives no contribution at the continuous level, but which ensures at least zeroth order consistency at the discrete level for constant solutions, as outlined in Avesani et al. (2014); on the other hand a smoothed velocity field is considered, which is based on the ALE interface velocity, so that the final particle velocity is consistent with the ALE interface velocity (Avesani et al., 2014).

Many physically important systems, such as multi-phase or multi-fluid flow, can not be written in a fully conservative form. For that purpose, we use the *path-conservative* approach developed by Castro and Parés and co-workers in the context of finite volume and discontinuous Galerkin finite element schemes, see Parés (2006); Castro et al. (2006); Muñoz and Parés (2007); Dumbser et al. (2010). These path-conservative schemes are formally consistent with the theory of Dal Maso, Le Floch and Murat (DLM) Maso et al. (1995). According to this theory, the extended jump relations across a discontinuity are ruled by a certain *integration*

path, which connects the left and right state of the discontinuity in the phase-space.

The simplest path is the straight line segment path, since it allows to construct *well-balanced* schemes for shallow water systems, which means numerical schemes that exactly preserve flat water at rest for arbitrary bottom topography also at the discrete level. Well-balanced schemes for shallow water systems have been discussed for the first time in the pioneering works of Bermudez and Vázquez-Cendón (1994) and LeVeque (1998), and many other developments have been made in that direction in the context of finite volume schemes (Vázquez-Cendón, 1999; Xing and Shu, 2006; Noelle et al., 2006) for a non-exhaustive overview. While well-balanced finite volume schemes are state of the art, the development of well-balanced SPH schemes for shallow water systems instead is only at its infancy at the moment. To our knowledge up to now there exist no well-balanced SPH schemes based on the use of approximate Riemann solvers and path-conservative methods for non-conservative hyperbolic PDE. It is therefore the aim of this work to produce a new family of *well-balanced SPH schemes* for shallow water systems.

7.2 Governing PDE system

We consider systems of hyperbolic equations with non-conservative products of the following form:

$$\frac{\partial \mathbf{Q}}{\partial t} + \nabla \cdot \mathbf{F}(\mathbf{Q}) + \mathbf{B}(\mathbf{Q}) \cdot \nabla \mathbf{Q} = \mathbf{S}(\mathbf{Q}), \tag{7.2.1}$$

where $\mathbf{Q}$ represents the vector of the unknowns $\mathbf{Q} = \mathbf{Q}(\mathbf{x}, t) = (q_1, q_2, ..., q_m)^T$, $\mathbf{x} = (x, y) \in \Omega(t) \subset \mathbb{R}^2$ is the spatial coordinate vector in two space dimensions, $\Omega(t)$ is the (moving) domain, $t \in \mathbb{R}_0^+$ is time, $\mathbf{F}(\mathbf{Q}) = (\mathbf{f}, \mathbf{g})$ is the non-linear flux tensor and the last term on the left hand side $\mathbf{B}(\mathbf{Q}) \cdot \nabla \mathbf{Q}$ represents the *non-conservative* product. $\mathbf{S}(\mathbf{Q})$ is an algebraic source term, which may contain volume forces like gravity or friction.

We can further rewrite the PDE system (7.2.1) in the following quasi-linear form

$$\frac{\partial \mathbf{Q}}{\partial t} + \mathbf{A}(\mathbf{Q}) \cdot \nabla \mathbf{Q} = \mathbf{S}(\mathbf{Q}), \tag{7.2.2}$$

with the matrix

$$\mathbf{A}(\mathbf{Q}) = \frac{\partial \mathbf{F}}{\partial \mathbf{Q}} + \mathbf{B}(\mathbf{Q}), \tag{7.2.3}$$

which is the Jacobian matrix of the flux tensor plus the matrix $\mathbf{B}(\mathbf{Q})$ of the non conservative terms. The previous system is called **hyperbolic** if the matrix $\mathbf{A}(\mathbf{Q}) \cdot \mathbf{n}$ has *m* real eigenvalues and a corresponding set of *m* linearly independent eigenvectors for all unit normal vectors $\mathbf{n}$ with $\|\mathbf{n}\| = 1$. Furthermore, in this Chapter we will also use the quantity $\mathbf{H}$, which is the flux tensor of the PDE, but referred to a frame moving with a generic velocity $\mathbf{v}$:

$$\mathbf{H}(\mathbf{Q}, \mathbf{v}) = \mathbf{F}(\mathbf{Q}) - \mathbf{Q} \otimes \mathbf{v}, \tag{7.2.4}$$

In the following we briefly describe the PDE systems treated in this work: the Baer-Nunziato model of compressible multi-phase flows, the single- and two-layer shallow water equations and the two-phase Pitman & Le model of debris flow.

7.2.1 Baer-Nunziato model

A seven equation Baer-Nunziato type model for compressible two-phase flow with relaxation terms and gravity force is given by the following system of equations, see Baer and Nunziato (1986):

$$
\begin{cases}
\dfrac{\partial}{\partial t}\left(\phi_1\rho_1\right) + \nabla\cdot\left(\phi_1\rho_1\mathbf{v}_1\right) = 0, \\
\dfrac{\partial}{\partial t}\left(\phi_1\rho_1\mathbf{v}_1\right) + \nabla\cdot\left(\phi_1\rho_1\mathbf{v}_1\otimes\mathbf{v}_1 + \phi_1 p_1\right) - p_I\nabla\phi_1 = \\
\qquad\qquad -\lambda\left(\mathbf{v_1}-\mathbf{v_2}\right) + \phi_1\rho_1\,\boldsymbol{g}, \\
\dfrac{\partial}{\partial t}\left(\phi_1\rho_1 E_1\right) + \nabla\cdot\left(\left(\phi_1\rho_1 E_1 + \phi_1 p_1\right)\mathbf{v}_1\right) - p_I\mathbf{v}_I\cdot\nabla\phi_1 = \\
\qquad\qquad -\lambda\,\mathbf{v_I}\cdot\left(\mathbf{v_1}-\mathbf{v_2}\right) + \nu p_I(p_1-p_2) + \phi_1\rho_1\,\boldsymbol{g}\cdot\mathbf{v}_1, \\
\dfrac{\partial}{\partial t}\left(\phi_2\rho_2\right) + \nabla\cdot\left(\phi_2\rho_2\mathbf{v}_2\right) = 0, \\
\dfrac{\partial}{\partial t}\left(\phi_2\rho_2\mathbf{v}_2\right) + \nabla\cdot\left(\phi_2\rho_2\mathbf{v}_2\otimes\mathbf{v}_2 + \phi_2 p_2\right) - p_I\nabla\phi_2 = \\
\qquad\qquad -\lambda\,\left(\mathbf{v_2}-\mathbf{v_1}\right) + \phi_2\rho_2\,\boldsymbol{g}, \\
\dfrac{\partial}{\partial t}\left(\phi_2\rho_2 E_2\right) + \nabla\cdot\left(\left(\phi_2\rho_2 E_2 + \phi_2 p_2\right)\mathbf{v}_2\right) - p_I\mathbf{v}_I\cdot\nabla\phi_2 = \\
\qquad\qquad -\lambda\,\mathbf{v_I}\cdot\left(\mathbf{v_2}-\mathbf{v_1}\right) + \nu p_I(p_2-p_1) + \phi_2\rho_2\,\boldsymbol{g}\cdot\mathbf{v}_2, \\
\dfrac{\partial}{\partial t}\phi_1 + \mathbf{v}_I\nabla\phi_1 = \nu(p_1-p_2).
\end{cases}
$$

The system is closed by the stiffened equation of state (EOS):

$$e_k = \frac{p_k + \gamma_k\pi_k}{\rho_k(\gamma_k - 1)}. \tag{7.2.5}$$

In the previous equations ϕ_k denotes the volume fraction of phase k, ρ_k the density, $\mathbf{v}_k$ the velocity vector, $E_k = e_k + \frac{1}{2}\mathbf{v}_k^2$ and e_k the phase specific total and internal energies respectively; $\boldsymbol{g}$ is the gravity acceleration. Without loss of generality we call phase 1 the *solid* phase (with underscript s) and phase 2 the *gas* phase (underscript g). Interface velocity and pressure, $\mathbf{u}_I$ and p_I, are part of the modeling and we choose:

$$\mathbf{v}_I = \mathbf{v}_1 \qquad \text{and} \qquad p_I = p_2 \tag{7.2.6}$$

according to Baer and Nunziato (1986). The state vector $\mathbf{Q}$ is given by

$$\mathbf{Q} = \left(\phi_1\rho_1,\ \phi_1\rho_1\mathbf{v}_1,\ \phi_1\rho_1 E_1,\ \phi_2\rho_2,\ \phi_2\rho_2\mathbf{v}_2,\ \phi_2\rho_2 E_2,\ \phi_1\right). \tag{7.2.7}$$

In system (7.2.5) we note the presence of pressure and velocity relaxation terms on the right hand sides, driven by relaxation parameters λ, ν.

Hence system (7.2.5) models non-equilibrium two-phase mixtures in the presence of inter-phase friction. Note that in the case $\lambda \to \infty$ and $\nu \to \infty$ the system instantaneously relaxes to the mechanical equilibrium. Instead, in the following we will neglect pressure relaxation and inter-phase friction by setting $\lambda = \nu = 0$.

7.2.2 Single-layer shallow water equations

The single layer shallow water equations are a hyperbolic PDE system that can be written under the general form (7.2.1). Considering a fixed bottom condition, the equations are the following:

$$\begin{aligned} \frac{\partial h}{\partial t} + \nabla \cdot (h\mathbf{v}) &= 0, \\ \frac{\partial (h\mathbf{v})}{\partial t} + \nabla \cdot \left(h\mathbf{v} \otimes \mathbf{v} + \frac{1}{2} g h^2 \mathbf{I} \right) + gh\nabla b &= 0, \\ \frac{\partial b}{\partial t} &= 0, \end{aligned} \tag{7.2.8}$$

where h is the water depth, $\mathbf{v} = (u, v)$ is the velocity vector, g is the gravity constant, $b = b(\mathbf{x})$ is the bottom topography and $\mathbf{I}$ is the identity matrix.
This system is characterized by two linearly degenerate fields associated with the intermediate eigenvalues. One is a stationary wave due to the bottom jump, the other one is a shear wave associated with the transverse velocity. The system (7.2.8) admits the following important steady state solution (lake at rest) for general bottom topography:

$$\eta = h + b = const. \qquad \text{and} \qquad \mathbf{v} = 0. \tag{7.2.9}$$

The eigenvalues and eigenvectors associated with the linear degenerate fields are given by

$$\mathbf{\Lambda}_* = \begin{pmatrix} 0 & 0 \\ 0 & u \end{pmatrix}, \quad \mathbf{L}_* = \begin{pmatrix} 0 & 0 & 0 & \frac{c^2}{u^2 - c^2} \\ -v & 0 & 1 & 0 \end{pmatrix}, \quad \mathbf{R}_* = \begin{pmatrix} 1 & 0 \\ 0 & 0 \\ 0 & 1 \\ \frac{c^2}{u^2 - c^2} & 0 \end{pmatrix}$$

with $c^2 = gh$.

7.2.3 Two-layer shallow water equations

Another example of a hyperbolic system with non-conservative product are the two layer shallow water equations, which read as follows:

$$\begin{cases} \dfrac{\partial h_1}{\partial t} + \nabla \cdot (h_1 \mathbf{v}_1) = 0, \\ \dfrac{\partial (h_1 \mathbf{v}_1)}{\partial t} + \nabla \cdot \left(h_1 \mathbf{v}_1 \otimes \mathbf{v}_1 + \dfrac{1}{2} g h_1^2 \mathbf{I} \right) + \\ \qquad\qquad + g h_1 \nabla h_2 + g h_1 \nabla b = 0, \\ \dfrac{\partial h_2}{\partial t} + \nabla \cdot (h_2 \mathbf{v}_2) = 0, \\ \dfrac{\partial (h_2 \mathbf{v}_2)}{\partial t} + \nabla \cdot \left(h_2 \mathbf{v}_2 \otimes \mathbf{v}_2 + \dfrac{1}{2} g h_2^2 \mathbf{I} \right) + \\ \qquad\qquad + \rho g h_2 \nabla h_1 + g h_2 \nabla b = 0, \\ \dfrac{\partial b}{\partial t} = 0, \end{cases}$$

where h_k is the water depth, $\mathbf{v}_k = (u_k, v_k)$ is the velocity vector and k indicates the layer that we are referring to (1 is the upper layer and 2 the lower layer); furthermore g is the gravity acceleration, $\rho = \rho_1/\rho_2$ is the density ratio of the two layers and $b = b(\mathbf{x})$ is the bottom topography that depends on $\mathbf{x}$. The lake at rest solution for this PDE system reads:

$$h_1 = const, \qquad \eta = h_1 + h_2 + b = const, \qquad \mathbf{v}_1 = \mathbf{v}_2 = 0. \quad (7.2.10)$$

where $\eta = \eta_1 = b + h_2 + h_1$ is the total elevation of the free surface and $\eta_2 = b + h_2$ is the total elevation of the lower fluid.
Writing these equations in the quasi linear form (7.2.2), with the state vector $\mathbf{Q} = (h_1, h_1 u_1, h_1 v_1, h_2, h_2 u_2, h_2 v_2, b)^T$, the system matrix $\mathbf{A}(\mathbf{Q}) \cdot \mathbf{e}_x$ in x direction ($\mathbf{e}_x = (1, 0)$) reads:

$$\mathbf{A}(\mathbf{Q}) \cdot \mathbf{e}_x = \begin{pmatrix} 0 & 1 & 0 & 0 & 0 & 0 & 0 \\ -u_1^2 + g h_1 & 2u_1 & 0 & g h_1 & 0 & 0 & g h_1 \\ -u_1 v_1 & v_1 & u_1 & 0 & 0 & 0 & 0 \\ 0 & 0 & 0 & 0 & 1 & 0 & 0 \\ \rho g h_2 & 0 & 0 & -u_2^2 + g h_2 & 2u_2 & 0 & g h_2 \\ 0 & 0 & 0 & -u_2 v_2 & v_2 & u_2 & 0 \\ 0 & 0 & 0 & 0 & 0 & 0 & 0 \end{pmatrix}$$

The two-layer shallow water system contains three linearly degenerate fields: a stationary wave associated with the bottom jump and two shear

waves, associated with the transverse flow velocities v_1 and v_2. Below, we list the eigenvalues of these three inner fields, together with the associated left and right eigenvectors:

$$\mathbf{\Lambda}_* = \begin{pmatrix} 0 & 0 & 0 \\ 0 & u_1 & 0 \\ 0 & 0 & u_2 \end{pmatrix}, \quad \mathbf{L}_* = \begin{pmatrix} 0 & 0 & 0 & 0 & 0 & 0 & e_0 \\ -v_1 & 0 & 0 & 0 & 0 & 0 & 0 \\ 0 & 0 & 0 & -v_2 & 0 & 1 & 0 \end{pmatrix}$$

$$\mathbf{R}_* = \begin{pmatrix} e_0 c_1^2 u_2^2 & 0 & 0 \\ 0 & 0 & 0 \\ e_0 v_1 c_1^2 u_2^2 & 1 & 0 \\ e_0 c_2^2 e_2 & 0 & 0 \\ 0 & 0 & 0 \\ e_0 v_2 c_2^2 e_1 & 0 & 1 \\ e_0 e_2 & 0 & 0 \end{pmatrix}$$

where:

$$c_1^2 = g h_1, \quad c_2^2 = g h_2, \quad e_1 = (\rho - 1) c_1^2 + u_1^2, \quad e_2 = -c_2^2 e_1 + u_2^2 (u_1^2 - c_1^2) \tag{7.2.11}$$

and the variable e_0 is a normalization constant given by

$$e_0 = \frac{1}{\sqrt{e_2}} \tag{7.2.12}$$

7.2.4 Pitman & Le multi-phase debris flow model

The last system of equations under consideration is the multi-phase debris flow model of Pitman and Le (2005a), which is again a hyperbolic PDE system with non-conservative products. It can be written as

$$\begin{cases} \dfrac{\partial h_s}{\partial t} + \nabla \cdot (h_s \mathbf{v}_s) = 0, \\ \dfrac{\partial (h_s \mathbf{v}_s)}{\partial t} + \nabla \cdot \left(h_s \mathbf{v}_s \otimes \mathbf{v}_s + \dfrac{1}{2} g (h_s^2 + (1 - \rho) h_s h_f) \mathbf{I} \right) + \\ \qquad + \gamma g h_s \nabla h_f + g h_s \nabla b = 0, \\ \dfrac{\partial h_f}{\partial t} + \nabla \cdot (h_f \mathbf{v}_f) = 0, \\ \dfrac{\partial (h_f \mathbf{v}_f)}{\partial t} + \nabla \cdot \left(h_f \mathbf{v}_f \otimes \mathbf{v}_f + \dfrac{1}{2} g h_f^2 \mathbf{I} \right) + \\ \qquad + g h_f \nabla h_s + g h_f \nabla b = 0, \\ \dfrac{\partial b}{\partial t} = 0 \end{cases}$$

where h_k is the depth and $\mathbf{v}_k = (u_k, v_k)$ is the velocity vector of layer k, where s refers to the solid layer and f to the fluid layer; g is the gravity acceleration and $\rho = \rho_f/\rho_s < 1$ is the density ratio between the fluid and the solid. The state vector is $\mathbf{Q} = (h_s, h_s u_s, h_s v_s, h_f, h_f u_f, h_f v_f, b)^T$. For this system of equations the lake-at-rest condition is represented by:

$$\phi = \frac{h_s}{h_s + h_f} = const., \quad \eta = h_s + h_f + b = const., \quad \mathbf{v}_s = \mathbf{v}_f = 0. \tag{7.2.13}$$

Also in this case the PDE system has three linearly degenerate intermediate fields, a stationary wave (associated to the bottom jump) and two shear waves (associated with the transverse flow velocity v_k). Regarding the inner fields, the eigenvalues and associated left and right eigenvectors are the following:

$$\mathbf{\Lambda}_* = \begin{pmatrix} 0 & 0 & 0 \\ 0 & u_s & 0 \\ 0 & 0 & u_f \end{pmatrix}, \quad \mathbf{L}_* = \begin{pmatrix} 0 & 0 & 0 & 0 & 0 & 0 & e_0 \\ 0 & 0 & 1 & 0 & 0 & 0 & 0 \\ 0 & 0 & 0 & 0 & 0 & 1 & 0 \end{pmatrix}$$

$$\mathbf{R}_* = \begin{pmatrix} e_0 e_1 & -v_s & 0 \\ 0 & 0 & 0 \\ e_0 e_1 v_s & 1 & 0 \\ e_0 e_2 & 0 & -v_f \\ 0 & 0 & 0 \\ e_0 e_2 v_f & 0 & 1 \\ e_0 e_3 & 0 & 0 \end{pmatrix}$$

where:

$$e_1 = \left((2u_f^2 - g h_f) T_1^{xx} + 2u_f^2 \rho g h_s\right), \quad e_2 = g h_f \left(T_1^{xx} - T_2^{xx} + 2u_s^2\right) \tag{7.2.14}$$

$$e_3 = \left((2u_s^2 - 2\rho g h_s - T_1^{xx} - T_2^{xx}) u_f^2 + g h_f (T_2^{xx} - 2u_s^2)\right), \quad e_0 = \frac{1}{\sqrt{e_3}} \tag{7.2.15}$$

7.2.5 SPH formulation of Vila and Ben Moussa

A great improvement of the initial SPH formulation of Gingold and Monaghan has been obtained by Vila and Ben Moussa in Vila (1999);

B. Ben Moussa and Vila (1999); Moussa (2006). Their SPH scheme for the PDE system (7.2.1), with $\mathbf{B}(\mathbf{Q}) = 0$ and $\mathbf{S}(\mathbf{Q}) = 0$, reads

$$\frac{dV_i\mathbf{Q}_i}{dt} = -\sum_j^N V_i V_j 2\mathbf{G}_{ij} \cdot \nabla W_{ij}, \tag{7.2.16}$$

$$\frac{dV_i}{dt} = \sum_j^N V_i V_j (\mathbf{v}_j - \mathbf{v}_i) \nabla W_{ij}, \tag{7.2.17}$$

$$\frac{d\mathbf{r}_i}{dt} = \mathbf{v}_i, \tag{7.2.18}$$

where V_i is the volume pertaining to particle i and evolving according to Eq. (7.2.17); Eq. (7.2.16) represents the interaction between two particles i and j along the normal direction $\mathbf{n}_{ij}$, where $\mathbf{G}_{ij}$ is the numerical flux computed by an exact or approximate Riemann solver. W_{ij} is the kernel centered in $\mathbf{r}_i$ and ∇W_{ij} is the kernel gradient w.r.t. $\mathbf{r}_i$.

7.2.6 Path-conservative SPH schemes

We use the scheme adeopted byAvesani et al. (2014); it consists of the previous formulation with two differences. First, in Eq. (7.2.16) a new term is added:

$$\frac{dV_i\mathbf{Q}_i}{dt} = -\sum_j^N V_i V_j 2(\mathbf{G}_{ij} - \mathbf{H}_i) \cdot \nabla W_{ij}. \tag{7.2.19}$$

This new term $\mathbf{H}_i(\mathbf{Q}_i, \mathbf{v}_i) = \mathbf{F}(\mathbf{Q}_i) - \mathbf{Q}_i \otimes \mathbf{v}_i$ is the Lagrangian flux tensor computed at the state $\mathbf{Q}_i$ of the particle i. This leads to a flux difference formulation, ensuring at least zeroth order consistency for constant solutions. This term has no contribution at the continuous level, since the kernel must satisfy the consistency relations $\int W d\mathbf{x} = 1$ and $\int \nabla W d\mathbf{x} = 0$, but it has a non-zero contribution at a discrete level:

$$\int \mathbf{H}_i \nabla W d\mathbf{x} = \mathbf{H}_i \int \nabla W d\mathbf{x} = 0, \tag{7.2.20}$$

$$\sum_j \mathbf{H}_i \nabla W_{ij} = \mathbf{H}_i \sum_j \nabla W_{ij} \neq 0. \tag{7.2.21}$$

Furthermore, instead of Eq. (7.2.18), a smoothed velocity field is used to evolve the particle positions as follows:

$$\frac{d\mathbf{r}_i}{dt} = \frac{\sum_j^N \bar{\mathbf{v}}_{ij} V_j W_{ij}}{\sum_j^N V_j W_{ij}} \tag{7.2.22}$$

so that the final particle velocity is consistent with the interface velocity $\bar{\mathbf{v}}_{ij} = \frac{1}{2}(\mathbf{v}_i + \mathbf{v}_j)$ used in the numerical flux $\mathbf{G}_{ij}$.
Since Eq. (7.2.19) has a flux difference form, it is now straightforward to extend the Vila and Ben Moussa SPH scheme to a path-conservative method (Castro et al., 2006; Parés, 2006). For this purpose, we introduce a new path-conservative discretization term $\mathbf{D}_{ij}$, defined as follows:

$$\mathbf{D}_{ij} = \frac{1}{2}\int_0^1 \mathbf{B}(\psi(\mathbf{Q}_i, \mathbf{Q}_j, s))\frac{\partial \psi}{\partial s} ds := \frac{1}{2}\tilde{\mathbf{B}}(\mathbf{Q}_i, \mathbf{Q}_j) \cdot (\mathbf{Q}_j - \mathbf{Q}_i), \tag{7.2.23}$$

where $\mathbf{Q}_j$ and $\mathbf{Q}_i$ are the right and the left states, respectively, $\tilde{\mathbf{B}}$ is the generalized *Roe-matrix*, computed via a path integral of the non-conservative terms contained in $\mathbf{B}(\psi(\mathbf{Q}_i, \mathbf{Q}_j, s))$ and ψ is the integration path. We choose the simple straight-line segment path:

$$\psi = \psi(\mathbf{Q}_i, \mathbf{Q}_j, s) = \mathbf{Q}_i + s \cdot (\mathbf{Q}_j - \mathbf{Q}_i), \tag{7.2.24}$$

with $0 \leq s \leq 1$. Introducing the jump term $\mathbf{D}_{ij}$ into Eq.(7.2.16), we obtain the following final scheme:

$$\begin{aligned}\frac{dV_i\mathbf{Q}_i}{dt} =& -\sum_j^N V_i V_j 2\left(\mathbf{G}_{ij}(\mathbf{Q}_i, \mathbf{Q}_j, \bar{\mathbf{v}}_{ij}) - \mathbf{H_i} + \mathbf{D}_{ij}\right) \cdot \nabla W_{ij} \\ &+ V_i \mathbf{S}(\mathbf{Q}_i),\end{aligned} \tag{7.2.25}$$

$$\frac{dV_i}{dt} = \sum_j^N V_i V_j 2(\bar{\mathbf{v}}_{ij} - \mathbf{v}_i)\nabla W_{ij}, \tag{7.2.26}$$

$$\frac{d\mathbf{r}_i}{dt} = \frac{\sum_j^N \bar{\mathbf{v}}_{ij} V_j W_{ij}}{\sum_j^N V_j W_{ij}}. \tag{7.2.27}$$

7.2.7 Riemann-solvers

We use three Riemann solver to compute the flux $\mathbf{G}_{ij}$: the Rusanov flux (Rusanov, 1961), the Osher flux in the variant proposed by Dumbser and Toro (2011a,b) and a new path-conservative formulation of the HLLEM solver (Einfeldt, 2001; Einfeldt et al., 1991; Dumbser and Balsara, 2016).

Rusanov scheme The Rusanov flux has the following form:

$$\mathbf{G}_{ij} = \frac{1}{2}(\mathbf{H}(\mathbf{Q}_j, \bar{\mathbf{v}}_{ij}) + \mathbf{H}(\mathbf{Q}_i, \bar{\mathbf{v}}_{ij})) - \frac{c_{ij}}{2}(\mathbf{Q}_i - \mathbf{Q}_j) \otimes \mathbf{n}_{ij}, \quad (7.2.28)$$

Here, c_{ij} is the maximum absolute eigenvalue of the matrix $\mathbf{C}_\mathbf{n}(\mathbf{Q}, \mathbf{v}) = \left(\frac{\partial \mathbf{H}}{\partial \mathbf{Q}} + \mathbf{B}(\mathbf{Q})\right) \cdot \mathbf{n}_{ij}$, evaluated in the normal direction between the two particles. If $\mathbf{\Lambda}_n$ is the diagonal matrix of the eigenvalues of $\mathbf{C}_\mathbf{n}$, then c_{ij} reads as follows:

$$c_{ij} = \max(|\mathbf{\Lambda}_n(\mathbf{Q}_i)|, |\mathbf{\Lambda}_n(\mathbf{Q}_j)|). \quad (7.2.29)$$

The path-conservative jump term $\mathbf{D}_{ij}$ in the case of the Rusanov scheme simply reads:

$$\mathbf{D}_{ij} = \frac{1}{2}\tilde{\mathbf{B}}_{ij}\,(\mathbf{Q}_j - \mathbf{Q}_i) \otimes \mathbf{n}_{ij}, \quad (7.2.30)$$

with the generalized Roe matrix defined by the path integral

$$\tilde{\mathbf{B}}_{ij} = \int_0^1 \mathbf{B}\left(\psi(\mathbf{Q}_i, \mathbf{Q}_j, s)\right) ds, \quad (7.2.31)$$

where ψ is given by the segment path (7.2.24). The integral is conveniently approximated by a Gauss-Legendre quadrature rule of suitable order of accuracy (typically, we use 3 quadrature points).

Osher scheme The approximate Riemann solver summarized here is the DOT version of the Osher-Solomon scheme recently proposed in Dumbser and Toro (2011a,b); its formulation is the following:

$$\mathbf{G}_{ij} = \frac{1}{2}(\mathbf{H}(\mathbf{Q}_j, \bar{\mathbf{v}}_{ij}) + \mathbf{H}(\mathbf{Q}_i, \bar{\mathbf{v}}_{ij})) - \mathbf{\Theta}(\mathbf{Q}_j - \mathbf{Q}_i) \otimes \mathbf{n}_{ij}, \quad (7.2.32)$$

The term $\mathbf{\Theta}$ is the *dissipation matrix*, which reads:

$$\mathbf{\Theta} = \frac{1}{2}\int_0^1 |\mathbf{C}_\mathbf{n}(\psi(\mathbf{Q}_i, \mathbf{Q}_j, s), \bar{\mathbf{v}}_{ij})|\, ds, \quad (7.2.33)$$

where $\mathbf{C_n}(\mathbf{Q},\mathbf{v}) = \left(\frac{\partial \mathbf{H}}{\partial \mathbf{Q}} + \mathbf{B}(\mathbf{Q})\right) \cdot \mathbf{n}_{ij}$ is evaluated along $\mathbf{n}_{ij}$ and ψ is the integration path connecting the left and right state in phase-space according to (7.2.24) (segment). Following the ideas of Dumbser and Toro (2011a,b), the integral is approximated via a three point Gauss-Legendre quadrature formula. The absolute value operator of the matrix $\mathbf{C_n}$ is computed as usual as:

$$|\mathbf{C_n}| = \mathbf{R_n}|\mathbf{\Lambda_n}|\mathbf{R_n}^{-1} \tag{7.2.34}$$

where $\mathbf{R_n}$ and $\mathbf{R_n}^{-1}$ are the matrices of the right and left eigenvectors, respectively, while $\mathbf{\Lambda_n}$ is the diagonal matrix of eigenvalues. For the Osher solver, the path conservative term $\mathbf{D}_{ij}$ has been computed as for the Rusanov method, i.e. according to (7.2.30) with the generalized Roe matrix (7.2.31).

HLLEM scheme The last numerical flux used is the HLLEM flux, whose formulation is:

$$\begin{aligned}\mathbf{G}_{ij} =& \frac{s_j \mathbf{H}_i - s_i \mathbf{H}_j}{s_j - s_i} + \frac{s_j s_i}{s_j - s_i}(\mathbf{Q}_j - \mathbf{Q}_i) \otimes \mathbf{n}_{ij} + \\ & - \frac{s_j s_i}{s_j - s_i}\mathbf{R}_*(\overline{\mathbf{Q}})\delta_*(\overline{\mathbf{Q}})\mathbf{L}_*(\overline{\mathbf{Q}})(\mathbf{Q}_j - \mathbf{Q}_i) \otimes \mathbf{n}_{ij}\end{aligned} \tag{7.2.35}$$

where $\overline{\mathbf{Q}}$ represents an intermediate state between the left and the right state $\mathbf{Q}_i$ and $\mathbf{Q}_j$, respectively; in Dumbser and Balsara (2016) the simple arithmetic average is used, i.e. $\overline{\mathbf{Q}} = \frac{1}{2}(\mathbf{Q}_i + \mathbf{Q}_j)$. The matrices $\mathbf{R}_*(\overline{\mathbf{Q}})$ and $\mathbf{L}_*(\overline{\mathbf{Q}})$ are the matrices of the right and left eigenvectors that are associated to the intermediate fields that one wants to resolve with the HLLEM Riemann solver. Furthermore, s_i and s_j are the speeds of the left and right moving waves, and they are here chosen as follows:

$$s_i = \min\left(0, \mathbf{\Lambda_n}(\mathbf{Q}_i), \mathbf{\Lambda_n}(\overline{\mathbf{Q}})\right), \quad s_j = \max\left(0, \mathbf{\Lambda_n}(\mathbf{Q}_j), \mathbf{\Lambda_n}(\overline{\mathbf{Q}})\right), \tag{7.2.36}$$

where $\mathbf{\Lambda_n}$ is the diagonal matrix of (all) the eigenvalues of the matrix $\mathbf{C_n}$ of the PDE system, evaluated in direction $\mathbf{n}_{ij}$.
Finally $\delta_*(\overline{\mathbf{Q}})$ is a diagonal matrix that controls the amount of the anti-diffusion, whose formulation has been derived in Dumbser and Balsara (2016), starting from the stability analysis of Einfeldt (2001):

$$\delta_*(\overline{\mathbf{Q}}) = \mathbf{I} - \frac{\mathbf{\Lambda}_*^-}{s_i} - \frac{\mathbf{\Lambda}_*^+}{s_j}. \tag{7.2.37}$$

In this relation, $\mathbf{I}$ is the identity matrix and $\mathbf{\Lambda}_*^{\pm} = \frac{1}{2}(\mathbf{\Lambda}_*(\overline{\mathbf{Q}}) \pm |\mathbf{\Lambda}_*(\overline{\mathbf{Q}})|)$. This means that the anti-diffusion is ruled by the ratio of the internal

eigenvalues compared to the maximum external wave speeds; we note that $0 < \delta_*(\overline{\mathbf{Q}}) \leq 1$, since for all the internal fields $|\mathbf{\Lambda}_*^-| < |s_i|$ and $\mathbf{\Lambda}_*^+ < s_j$.
Finally, the path conservative term $\mathbf{D}_{ij}$ is slightly different from the other two cases. It takes the following form:

$$\mathbf{D}_{ij} = \frac{s_i}{s_j + s_i} \tilde{\mathbf{B}} \left(\mathbf{Q}_j - \mathbf{Q}_i \right) \otimes \mathbf{n}_{ij}, \tag{7.2.38}$$

where $\tilde{\mathbf{B}}$ is again the generalized Roe matrix (7.2.31), computed in same way as for the Rusanov and the Osher method.

7.2.8 Smoothing kernel

The smoothing kernel function W_{ij} considered is the cubic spline kernel:

$$W_{ij} = \frac{k}{h_{ij}^d} \begin{cases} \frac{2}{3} - q_{ij}^2 + \frac{1}{2} q_{ij}^3 & \text{if} \quad 0 \leq q_{ij} < 1, \\ \frac{1}{6}(2 - q_{ij})^3 & \text{if} \quad 1 \leq q_{ij} \leq 2, \\ 0 & \text{if} \quad q_{ij} > 2, \end{cases} \tag{7.2.39}$$

where q_{ij} is defined as :

$$q_{ij} = \| \mathbf{r}_j - \mathbf{r}_i \| / h_{ij} \tag{7.2.40}$$

and d represents the number of space dimensions (in our case $d = 1$ or $d = 2$). k is a normalization constant so that $\int W d\mathbf{x} = 1$. The variable h_{ij} is the so called *smoothing length* and can be defined as follows:

$$h_{ij} = \frac{1}{2}(h_i + h_j), \qquad \text{with} \qquad h_i = \sigma \sqrt[d]{\frac{m_i}{\rho_i}} \tag{7.2.41}$$

with σ a constant, choosen so that the compact support of each kernel includes enough particles; its value ranges between 1.5 and 2.0.

7.3 Numerical results

In this section we show some computational results obtained with the path-conservative SPH scheme (PC-SPH) previously decribed. We compare the results obtained with the three different Riemann solvers with each other and with available reference solutions, both in the one and in the two dimensional case. Furthermore, the computational time required by the different types of solver is pointed out, in order to show the efficiency of each Riemann solver.

7.3.1 One-dimensional test problems

In this first section we show the results of the one-dimensional problems, for all the PDE system of equations previously presented.

Baer-Nunziato model

We have solved five Riemann problems on an initial domain $\Omega(0) = [-0.5; +0.5]$ using our new path-conservative SPH scheme on a computational grid of 500 particles and a CFL number equal to 0.9. For the BN model, the particles are moved with the interface velocity $\mathbf{v} = \mathbf{v}_I = \mathbf{v}_2$. In Table 7.1 the initial conditions for five Riemann problems RP1-RP5 are defined.

	ρ_s	u_s	p_s	ρ_g	u_g	p_g	ϕ_s	t_{end}
RP1:	$\gamma_s = 1.4,$	$\pi_s = 0,$	$\gamma_g = 1.4,$	$\pi_g = 0$				
L	1.0	0.0	1.0	0.5	0.0	1.0	0.4	0.10
R	2.0	0.0	2.0	1.5	0.0	2.0	0.8	
RP2:	$\gamma_s = 3.0,$	$\pi_s = 100,$	$\gamma_g = 1.4,$	$\pi_g = 0$				
L	800.0	0.0	500.0	1.5	0.0	2.0	0.4	0.10
R	1000.0	0.0	600.0	1.0	0.0	1.0	0.3	
RP3:	$\gamma_s = 1.4,$	$\pi_s = 0,$	$\gamma_g = 1.4,$	$\pi_g = 0$				
L	1.0	0.9	2.5	1.0	0.0	1.0	0.9	0.10
R	1.0	0.0	1.0	1.2	1.0	2.0	0.2	
RP4:	$\gamma_s = 3.0,$	$\pi_s = 3400,$	$\gamma_g = 1.35,$	$\pi_g = 0$				
L	1900.0	0.0	10.0	2.0	0.0	3.0	0.2	0.15
R	1950.0	0.0	1000.0	1.0	0.0	1.0	0.9	
RP5:	$\gamma_s = 1.4,$	$\pi_s = 0,$	$\gamma_g = 1.4,$	$\pi_g = 0$				
L	1.0	0.0	1.0	0.2	0.0	0.3	0.8	0.20
R	1.0	0.0	1.0	1.0	0.0	1.0	0.3	

Table 7.1: *Initial condition for the five Riemann problems solved with the PC-SPH scheme.*

Our numerical solutions have been compared to the exact ones; the first exact solution for the Baer-Nunziato system has been found by Adrianov and Warnecke Andrianov and Warnecke (2004). They used a so-called *inverse method*, that is, the initial states were derived from a given wave-pattern of the solution. Later, direct Riemann solvers have been developed by Schwendeman et al. (2006) and by Deledicque and Papalexandris (2007). In Figs. 7.1-7.2 we provide a detailed comparison of the three Riemann solvers for each Riemann problem. In all test cases it can be noted that the Rusanov scheme (which is not able to resolve steady

contact and shear waves) is much more diffusive at the material contact, while the DOT scheme and the HLLEM method are able to capture the material contact almost perfectly well, due to the Lagrangian nature of the SPH method. In all test problems, the HLLEM solver shows the best performance in the context of PC-SPH schemes.

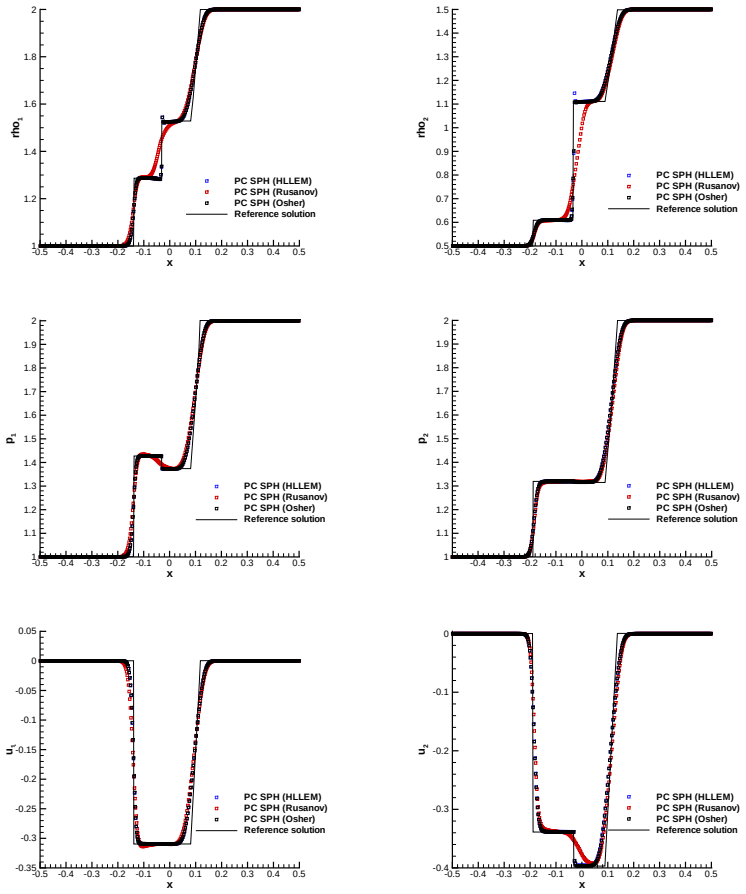

Figure 7.1: *Numerical solutions obtained with three approximate Riemann solvers (Osher, Rusanov and HLLEM) are compared among them and with the exact solution, for the Riemann problem RP1 of the Baer-Nunziato system. First line: densities of the two phases ρ_1 and ρ_2. Second line: pressures of the two phases p_1 and p_2. Third line: velocities of the two phases u_1 and u_2*

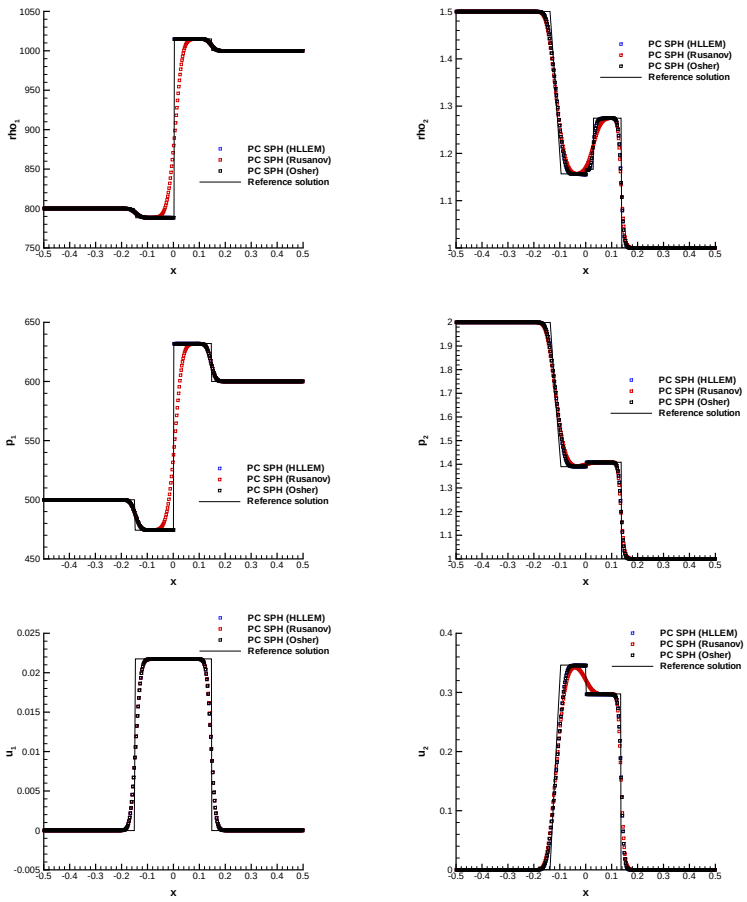

Figure 7.2: *Numerical solutions obtained with three approximate Riemann solvers (Osher, Rusanov and HLLEM) are compared among them and with the exact solution, for the Riemann problem RP2 of the Baer-Nunziato system. First line: densities of the two phases ρ_1 and ρ_2. Second line: pressures of the two phases p_1 and p_2. Third line: velocities of the two phases u_1 and u_2*

Single-layer shallow water equations

First we study the *well-balancing* property of our new PC-SPH schemes: this means that if $\eta = const.$ and $u = 0$, the scheme must maintain this steady state solution exactly. This can be easily checked numerically, for example through the test problem proposed LeVeque (1998).
The computational domain is taken as $\Omega = [0, 2]$ and the initial velocity is $u(x, 0) = 0$; then a small perturbation of the free surface is imposed, as well as a smooth irregularity of the bottom topography. The initial conditions are defined as follows:

$$\eta(x,0) = \begin{cases} 1+\epsilon & \text{if} \quad 1.1 \leq x \leq 1.2, \\ 1 & \text{else.} \end{cases} \tag{7.3.1}$$

and

$$b(x) = \begin{cases} 0.25(cos(10\pi(x-1.5))+1) & \text{if} \quad 1.4 \leq x \leq 1.6, \\ 0 & \text{else.} \end{cases} \tag{7.3.2}$$

The perturbation ϵ has been set to 0.2 (large perturbation) and then to 10^{-3} (small perturbation); we used for the simulations 400 particles and a CFL number of 0.9. In the case of the shallow water system, we set the mesh velocity to $\mathbf{v} = 0$.
In Figure 7.3 the results obtained with our PC-SPH scheme are compared with a fine grid reference solution obtained for the Leveque problem with a second order path-conservative TVD finite volume scheme using the DOT solver Dumbser and Toro (2011b), both for small and large perturbations. We observe a good agreement for both cases. No spurious oscillations in the free surface profile are visible. For the PC-SPH scheme the observed lower amplitudes of the surface waves can be explained with the low order of accuracy of the method. The exact well-balancing has also been checked for different machine precisions using $\epsilon = 0$. The results are listed in Table 7.7. Afterward, we solve four Riemann problems with our new method. We use again 400 cells with a CFL number of 0.9; for each problem the numerical solution is compared to the exact solution provided by E.F.Toro (2001) and by R. Bernetti and Toro. (2008). The initial conditions are summarized in Table 7.2 and Table 7.3, while the numerical solution together with the exact solution are shown in Figure 7.4 and Figure 7.5. We note an excellent agreement with the reference solution in all cases. Only the HLLEM results have been shown for clarity. However, also all the other Riemann solvers work

equally well.

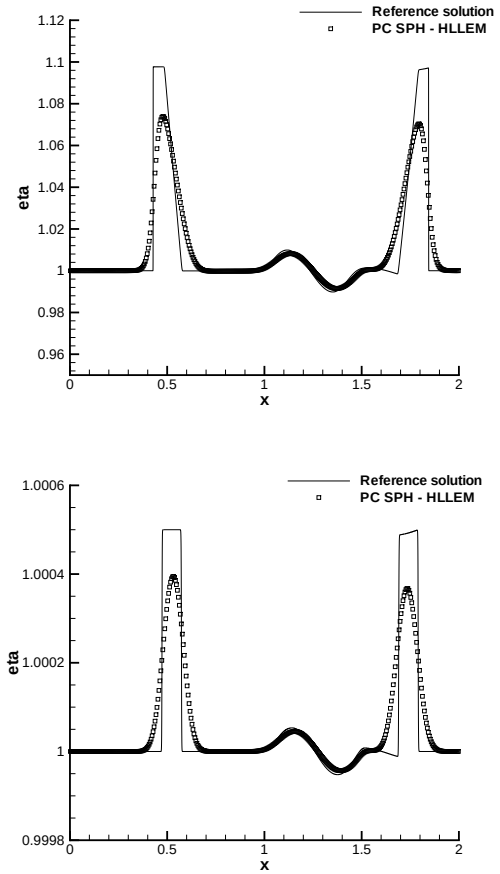

Figure 7.3: *Numerical and reference solution of the problem of LeVeque for the one-layer shallow water equations. Top: large perturbation ($\epsilon = 0.2$). Bottom: small perturbation ($\epsilon = 10^{-3}$).*

Case	h_L	u_L	v_L	b_L	h_R	u_R	v_R
RP0	2.0	0.0	1.0	0.0	1.0	0.0	-1.0
RP1	1.0	0.0	0.0	0.0	10^{-14}	0.0	0.0
RP2	1.46184	0.0	0.0	0.0	0.30873	0.0	0.0
RP3	0.75	-9.49365	0.0	0.0	1.10594	-4.94074	0.0
RP4	0.75	-1.35624	0.0	0.0	1.10594	-4.94074	0.0

Table 7.2: *Single-layer shallow water equations: initial condition for five Riemann problems, where h is the water depth, u and v velocity component, b bottom height, t_end final computational time, x_L and x_R the bounds of the domain and x_c the discontinuity location*

Case	b_R	t_{end}	x_L	x_R	x_c
RP0	1.0	1.0	0.0	1.0	0.5
RP1	0.0	0.075	0.0	1.0	0.5
RP2	0.2	1.0	-5.0	5.0	0.0
RP3	0.2	1.0	-15.0	5.0	0.0
RP4	0.2	1.0	-10.0	4.0	0.0

Table 7.3: *Single-layer shallow water equations: initial condition for five Riemann problems, where h is the water depth, u and v velocity component, b bottom height, t_end final computational time, x_L and x_R the bounds of the domain and x_c the discontinuity location*

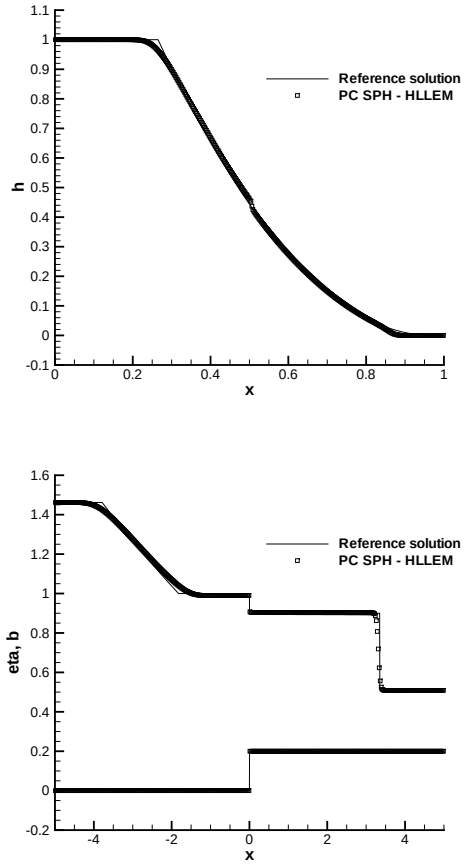

Figure 7.4: *Numerical solution and exact solution for **RP1-RP2** for the one-layer shallow water equations. The variable eta is the elevation of the free surface.*

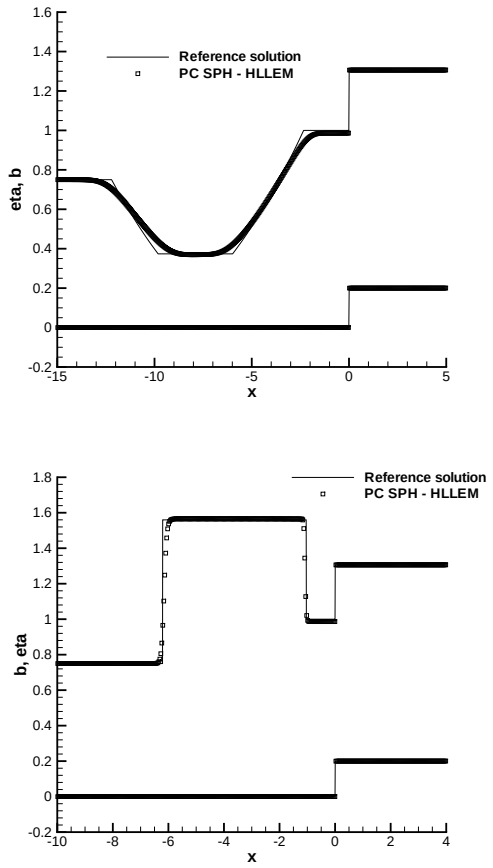

Figure 7.5: *Numerical solution and exact solution for **RP3-RP4** for the one-layer shallow water equations. The variable eta is the elevation of the free surface.*

Two-layer shallow water equations

Also for the two-layer shallow water equations we test the *well-balancing* property of our PC-SPH scheme. We define the initial condition for η and $b(x)$ as for the one-layer shallow water equations case, the velocities of both layers are set to zero, the CFL is chosen as 0.9 and the number of particles is 400. The mesh velocity is set to $\mathbf{v} = 0$. Furthermore, the final computational time is chosen to be $t = 0.2$ and the density ratio of the two fluid is $\rho = 0.8$. The initial height of the second layer is $\eta_2(x, 0) = 0.65$.
The perturbation of the free surface is represented by the value of ϵ: in the first case its value has been set to 0.2 (large perturbation) and in

the second case to 10^{-3} (small perturbation). In Figure 7.6 the numerical results are compared to a fine grid reference solution obtained with a second order path-conservative TVD finite volume scheme using the DOT solver Dumbser and Toro (2011b). The exact well-balancing of the PC-SPH scheme has also been checked for different machine precisions using $\epsilon = 0$. The results are listed in Table 7.7.

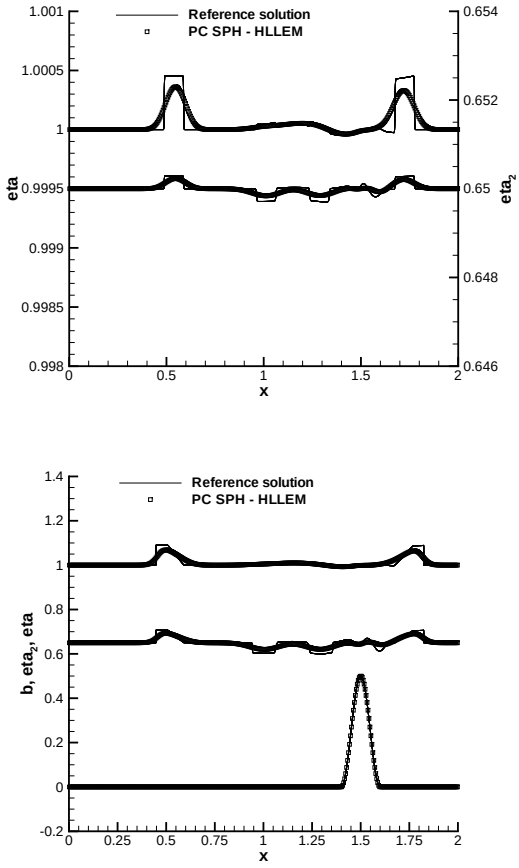

Figure 7.6: *Comparison between numerical and reference solution of the small and large perturbation test problem of LeVeque, at t=0.2. Left: small perturbation ($\epsilon = 10^{-3}$). Right: large perturbation ($\epsilon = 0.2$)*

In the following, we present the comparison between the numerical solution obtained with our PC-SPH scheme with a fine grid reference solution for two different Riemann problems. In all cases we assumed $\rho = 0.8$, and we used 400 particles. The initial conditions for all cases are summarized in Table 7.4.

Case	h_1	u_1	v_1	h_2	u_2	v_2	b	t_{end}	x_L	x_R	x_c
RP0 L:	0.5	0.0	0.5	0.8	0.0	-0.2	0.2	1.0	-5.0	5.0	0.0
R:	0.5	0.0	-0.5	0.2	0.0	0.2	0.8				
RP1 L:	0.4	0.0	0.0	0.6	0.0	0.0	0.0	1.25	-5.0	5.0	0.0
R:	0.6	0.0	0.0	0.4	0.0	0.0	0.0				

Table 7.4: *Two-layer shallow water equations: initial condition for two Riemann problems, where h is the water depth, u and v velocity component, b bottom height, t_end final computational time, x_L and x_R represent the domain and x_c the discontinuity location*

.

The results of RP0 are shown in Figure 7.7; the numerical solution is represented in comparison with the reference solution. For RP0 the HLLEM scheme is able to resolve all steady waves exactly.

Pitman & Le debris flow model

First of all, the *well-balancing* property has been verified, according to the test case of Pelanti et al. (2008). The setup is very similar to the one proposed by LeVeque (1998); in particular the bottom topography is:

$$b(x) = \begin{cases} 0.25(cos(10\pi(x-0.5))+1) & \text{if} \quad |x-0.5| \leq 0.1, \\ 0 & \text{else.} \end{cases} \tag{7.3.3}$$

while the free surface elevation $\eta = \eta_0$ and the solid volume fraction $\phi = \phi_0$, apart from a small region where the following perturbation is applied for $-0.6 \leq x \leq -0.5$:

$$\eta(x,0) = \eta_0 + \epsilon, \qquad \text{and} \qquad \phi(x,0) = \phi_0 - \epsilon \tag{7.3.4}$$

In the following we have set $\eta_0 = 1$, $\phi_0 = 0.6$, $g = 1$ (gravity acceleration constant) and $\rho = 0.5$. Initially, all the velocities are zero; the computational domain is $\Omega = [-1.2, 1.2]$, the number of particles is 400 and the CFL=0.9. The value of ϵ has been set to 10^{-3} (small perturbation); the numerical results are compared with the reference solution provided in Figure 7.8. Due to the low order of accuracy of the present PC-SPH scheme, the waves are visibly damped, but no spurious oscillations in the free surface are visible, thanks to the well-balancedness of the scheme. The exact well-balancing of the PC-SPH scheme has been checked also for the Pitman & Le model for different machine precisions using $\epsilon = 0$. The results are listed in Table 7.7. For the Pitman

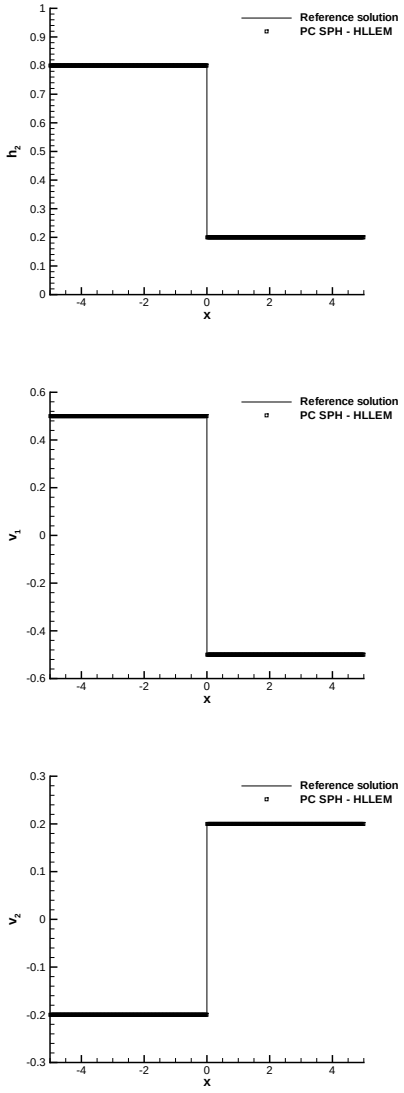

Figure 7.7: *Numerical solution obtained with the PC-SPH scheme presented in this article and exact solution of the Riemann problem RP0. Top: height of the second layer h_2. Middle: transversal velocity of the first layer v_1. Bottom: the transversal velocity of the second layer v_2.*

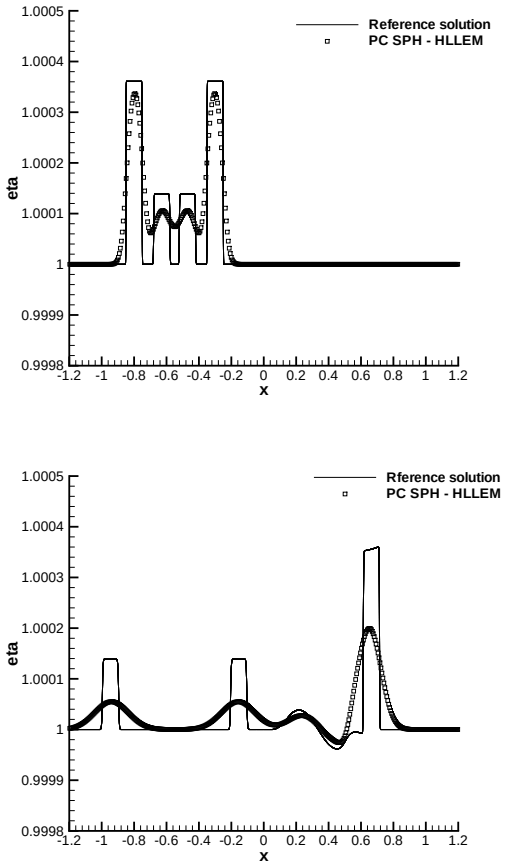

Figure 7.8: *Reference solution and numerical solution derived with our scheme for the LeVeque test problem at* $t = 0,25$ *(left) and* $t = 1,25$ *(right), for Pitman & Le equations.*

& Le equations other three Riemann problem have been solved: the initial condition for all of them have been listed in Table 7.5 and Table 7.6, while the comparison between the numerical solution and the reference solution are provided in Figure 7.9 and Figure 7.10. In all cases we can note a very good agreement with the reference solution.

Case	h_s	u_s	v_s	h_f	u_f	v_f	b
RP0 L:	1.5	0.0	0.2	0.5	0.0	-0.5	0.0
R:	1.125	0.0	-0.2	0.375	0.0	0.5	0.5
RP1 L:	2.1	0.0	0.0	0.9	0.0	0.0	0.0
R:	0.8	0.0	0.0	1.2	0.0	0.0	0.0
RP2 L:	2.1	-1.4	0.0	0.9	0.3	0.0	0.0
R:	0.8	-0.9	0.0	1.2	0.1	0.0	0.0

Table 7.5: *Two-fluid model of Pitman & Le: initial condition for three Riemann problems, where h_s and h_f are the solid and fluid depth, u and v velocity component (s for solid and f for fluid), b bottom height.*

.

Case	t_{end}	x_L	x_R	x_c
RP0 L:	1.0	-5.0	5.0	0.0
RP1 L:	0.5	-5.0	5.0	0.0
RP2 L:	0.5	-5.0	5.0	0.0

Table 7.6: *Two-fluid model of Pitman & Le: initial condition for three Riemann problems, where t_end is the final computational time, x_L and x_R represent the domain and x_c the discontinuity location.*

.

In Table 7.7 and Table 7.8 we summarize the computational results obtained for the exact well-balancing test cases ($\epsilon = 0$) obtained with the PC-SPH scheme for different machine precisions for the single and two-layer shallow water equations and for the Pitman & Le model. The errors refer to the L_∞ norm of the velocity.

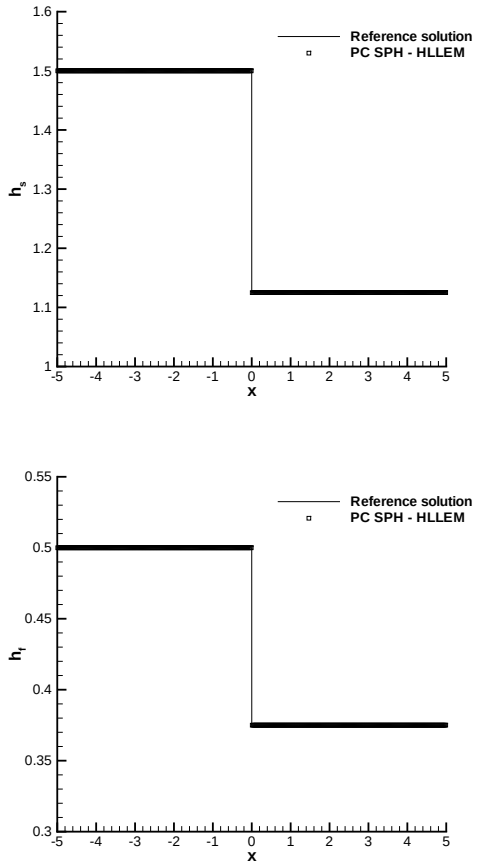

Figure 7.9: *Numerical solution and exact solution of the Pitman & Le equations for RP0. Solid depth h_s, and fluid depth h_f are represented.*

Case	L_∞ single layer SW	L_∞ two-layer SW
Single precision	$3.164952 \cdot 10^{-7}$	$4.1281626 \cdot 10^{-7}$
Double precision	$1.8219689 \cdot 10^{-15}$	$5.9267614 \cdot 10^{-16}$
Quadruple precision	$1.0519463 \cdot 10^{-33}$	$8.1748300 \cdot 10^{-34}$

Table 7.7: *The numerical verification of the exact C-property is reported here for the single layer shallow water equations (left column), for the two-layer shallow water equations (right column). The values of L_∞ refer to the flow velocity vectors $\boldsymbol{v}$ for the one layer SWE and $\boldsymbol{v}_1$ for the two-layer SWE.*

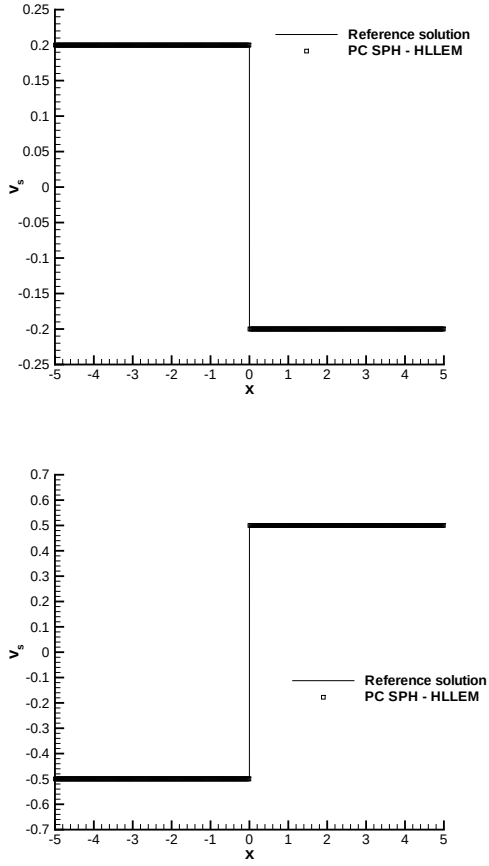

Figure 7.10: *Numerical solution and exact solution of the Pitman & Le equations for RP0. Solid velocity v_s and fluid velocity v_f are represented.*

Case	L_∞ Pitman & Le
Single precision	$1.1130131 \cdot 10^{-7}$
Double precision	$2.0535453 \cdot 10^{-16}$
Quadruple precision	$1.3489190 \cdot 10^{-34}$

Table 7.8: *The numerical verification of the exact C-property is reported here for the Pitman&Le model. The values of L_∞ refer to the flow velocity vector $\boldsymbol{v}_s$ for the Pitman & Le model.*

7.3.2 Two-dimensional test problems

For the two-dimensinal case we tested two circular explosion problems for the Baer-Nunziato model. For the one-layer shallow water equations, we run a two-dimensional version of the test case of LeVeque and a circular dambreak over a bottom step.

Baer-Nunziato model

We solve two circular explosion problems on a circular domain $\Omega = \{\mathbf{x} : \|\mathbf{x}\| \leq R\}$ of radius $R = 1$ and with initial data given by

$$\mathbf{Q}(\mathbf{x}, 0) = \begin{cases} \mathbf{Q}_L & \text{if} \quad r \leq r_0, \\ \mathbf{Q}_R & \text{if} \quad r > r_0, \end{cases} \tag{7.3.5}$$

with $r_0 = 0.5$. The inner and outer states $\mathbf{Q}_L$ and $\mathbf{Q}_R$ are defined in Table 7.10 and the mesh spacing used in this test case was $h = 1/400$. We use again three different types of Riemann solver: Rusanov, Osher (DOT) and HLLEM. In Table 7.9 the CPU times needed by each Riemann solver are listed: we may deduce that the best flux is HLLEM, since it is very good in reproducing the reference solution, like Osher, but it requires less CPU time. On the other side, the Rusanov scheme is associated with the minimum CPU time, but it is too diffusive, especially at the material contact.

	Rusanov	**Osher**	**HLLEM**
BNEP1	11850.00	83405.78	34025.74
BNEP2	17676.85	122386.67	49316.38

Table 7.9: *Comparison of the CPU time in seconds required by the three Riemann solvers.*

	ρ_s	u_s	v_s	p_s	ρ_g	u_g	v_g	p_g	ϕ_s	t_{end}
EP1:	$\gamma_s = 1.4, \quad \pi_s = 0, \quad \gamma_g = 1.4, \quad \pi_g = 0$									
L	1.0	0.0	0.0	1.0	0.5	0.0	0.0	1.0	0.4	0.10
R	2.0	0.0	0.0	2.0	1.5	0.0	0.0	2.0	0.8	
EP2:	$\gamma_s = 3.0, \quad \pi_s = 100, \quad \gamma_g = 1.4, \quad \pi_g = 0$									
L	800.0	0.0	0.0	500.0	1.5	0.0	0.0	2.0	0.4	0.10
R	1000.0	0.0	0.0	600.0	1.0	0.0	0.0	1.0	0.3	

Table 7.10: *Initial condition for the two explosion problems, solved with the PC-SPH scheme.*

In Figures 7.11, the numerical solutions obtained with our new PC-SPH scheme with various Riemann solvers are compared among them and with the reference solution, see Dumbser et al. (2010) for details of how the reference solution can be computed. As we could expect, the Rusanov method is much more diffusive than the other two. Osher and HLLEM produce both results of very similar quality; the advantage of HLLEM over the Osher solver is the CPU time that is required, which is much less with respect to Osher, as shown before in Table 7.9. In Figure **??** there is a 3D representation of the density of phase 1.

One-layer shallow water equations

In this section the numerical results obtained with our PC-SPH scheme applied to the one-layer shallow water equations in two space dimensions are presented.

Well-balancing First, the well-balancedness of our scheme in 2D has been verified through a 2D variant the LeVeque test case (LeVeque, 1998); it consists of a small perturbation of the free surface with a smooth variation of the bottom topography. It is similar to the LeVeque test problem already shown in the 1D case; the domain considered is $\Omega = [-2,1] \times [-0.5,0.5]$ and the initial velocities are set to zero, while the free surface level is:

$$\eta(x,0) = \begin{cases} 1+\epsilon & \text{if} \quad -0.95 \leq x \leq -0.85, \\ 1 & \text{else} \quad . \end{cases} \tag{7.3.6}$$

The bottom topography is defined as follows:

$$b(x,y) = 0.8\text{exp}(-5(x+0.1)^2 - 50y^2). \tag{7.3.7}$$

The simulation has been carried out on a grid of 500 $\times$ 200 particles, with a CFL number of 0.9 and $\epsilon = 0.01$. In Figure 7.12 the numerical solution is presented. We observe no spurious oscillations in the free surface profile, and our simulation agrees qualitatively with other results for this test case that are available in the literature, see e.g. LeVeque (1998); Canestrelli et al. (2010); Tavelli and Dumbser (2014).

We now run this test problem again and set $\epsilon = 0$, i.e. we can verify numerically the exact well-balancing of the scheme. In Table 7.11 the L_∞ errors of the velocity vector are reported for different machine precisions in order to provide numerical evidence that our PC-SPH scheme is exactly well-balanced also in 2D, as expected.

Case	L_∞ single layer shallow water equations
Single precision	$4.110494 \cdot 10^{-7}$
Double precision	$5.628736 \cdot 10^{-15}$
Quadruple precision	$8.122862 \cdot 10^{-34}$

Table 7.11: *The numerical verification of the exact C-property is reported here for the single layer shallow water equations in 2D. The values of L_∞ refer to the flow velocity vector **v**, for different machine precisions.*

Circular dambreak The second test case is a circular dambreak over a bottom step on a circular domain $\Omega = \{\mathbf{x} : \|\mathbf{x}\| \leq R\}$, with $R = 2$. This problem has an initial condition given by (7.3.5), with $\mathbf{v} = 0$ and $\eta_L = 1$, $\eta_R = 0.5$, $b_L = -0.2$ and $b_R = 0$. In Figure 7.13 the numerical results are compared to the reference solution. The reference solution has been obtained by solving an equivalent 1D PDE system with geometry source terms E.F.Toro (2001); Toro (1999) on a very fine grid of 10,000 cells, using a second order path-conservative TVD finite volume scheme based on the DOT solver Dumbser and Toro (2011b). A 3D representation is reported in Figure 7.14.

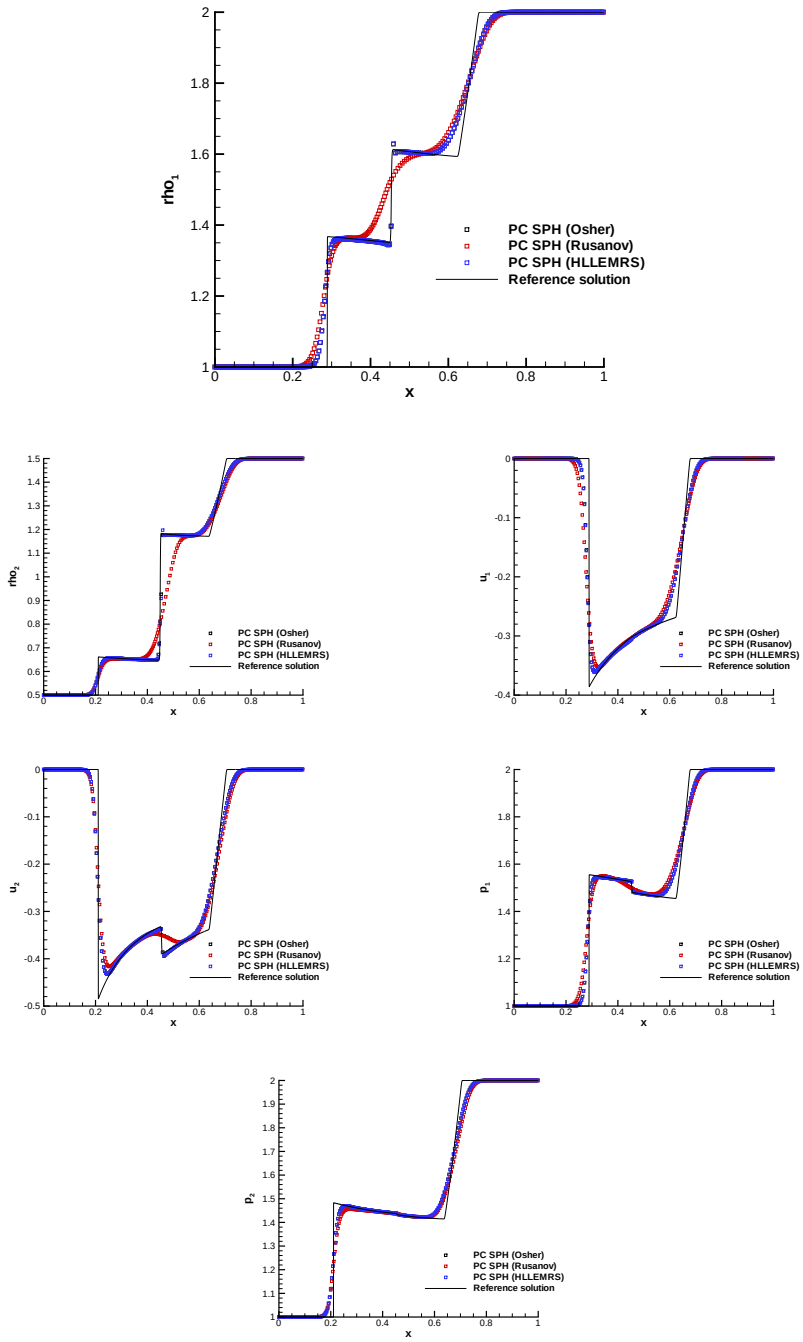

Figure 7.11: *Numerical solution and exact solution of the Baer-Nunziato equations, for the EP1. Starting from the top to the bottom : desity of the fluids ρ_i, fluids velocities u_i and fluids pressure p_i.*

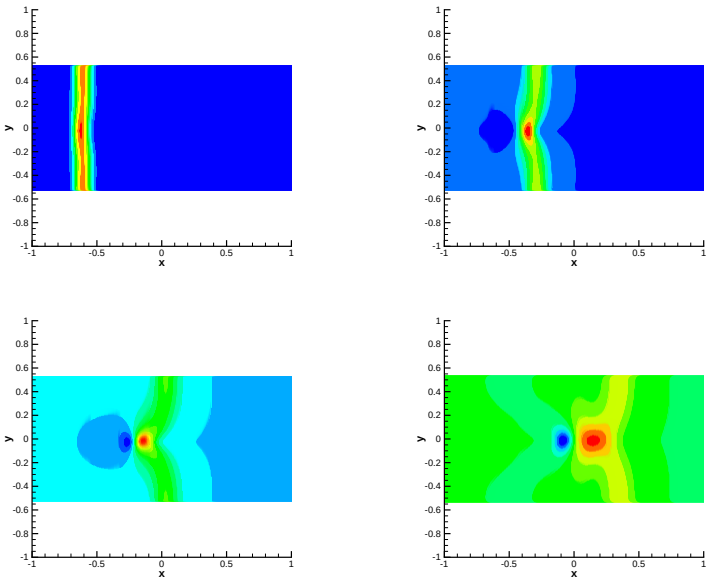

Figure 7.12: *Numerical results for the LeVeque test case in 2D. The different colours represent how the variable η changes in different times. From top to bottom and from left to right, the solution correspond to time $t_1 = 0.12$, $t_1 = 0.24$, $t_1 = 0.36$ and $t_1 = 0.48$.*

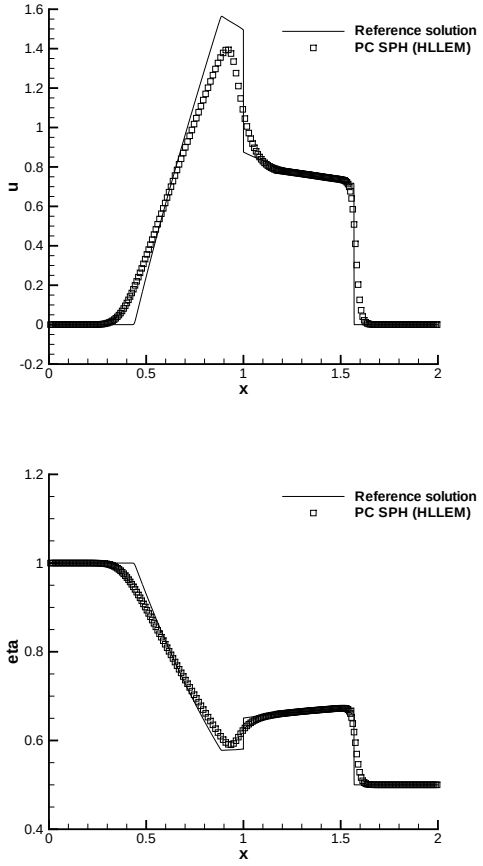

Figure 7.13: *Numerical solution and reference solution for the circular dambreak problem. On the left the fluid velocity u is represented and on the right the elevation of the free surface eta.*

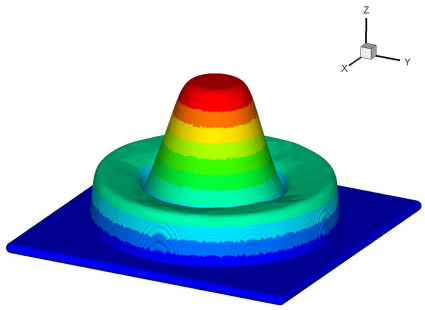

Figure 7.14: *3D representation of the free surface η for the circular dambreak problem.*

7.4 Path-conservative FVM

In order to solve the system presented in Chapter 5, together with the closure relations derived in Chapter 6, a path conservative finite volume method has been adopted.

$$
\begin{cases}
\text{Mass conservation of the solid phase:} \\
\dfrac{\partial}{\partial t}[C\,h + C^*\,z_b] + \dfrac{\partial}{\partial x}[\alpha_{cu}\,U\,C\,h] = 0 \\
\\
\text{Total mass conservation:} \\
\dfrac{\partial}{\partial x}(h + z_b) + \dfrac{\partial}{\partial x}(U\,h) = 0 \\
\\
\text{Momentum balance for the solid phase:} \\
\dfrac{\partial}{\partial t}[\alpha_{cu}\,C\,h\,U] + \dfrac{\partial}{\partial x}[\beta_{cu}\,U^2\,C\,h] + g\dfrac{\partial}{\partial x}\dfrac{Ch^2}{2} + \\
+ g\,C\,h\,\dfrac{\partial z_b}{\partial x} = -\dfrac{\tau_0}{\rho} \\
\\
\text{I closure relation:} \\
C = C^*\dfrac{E_1}{E_1 + \alpha_{cu}\dfrac{U}{\sqrt{gh}}\dfrac{d}{h}} \\
\\
\text{II closure relation:} \\
\tau_0 = \rho_s\,g\,h\,\sin\varphi\,C^*\dfrac{E_1}{E_1 + \alpha_{cu}\dfrac{U}{\sqrt{gh}}\dfrac{d}{h}}
\end{cases}
\tag{7.4.1}
$$

The system (7.4.1) is an hyperbolic system, written in conservative form; it represents the effective form of the system solved in this thesis.
This form of the equations that neglect α_{zb} and α_{fs} correspond to consider the hydrostatic pressure acting on the vertical direction (instead of the direction normal to the free surface) and to neglect the vertical bed friction contribution. This seems to be quite reasonable, since for small slope angle the friction contribution is primarily horizontal, while for a more pronounced slope angle, the motion becomes faster and the frictional contribution with respect to the collisional one is almost negligible. Taking into account the contribution of the two slopes in the conservatives variable may change the eigen-structure of the system and it could become no more hyperbolic. The analysis of this aspect will be

deepened in future work.
Furthermore, in this first applications, the channel width is assumed constant $B(x) = B$. However the introduction of further terms that account for the variation in space of the channel width is straightforward and would be analyzed in future work too.
The system is characterized by three partial differential equation and two algebraic closure relations. Therefore we have solved a three PDE system, inserting for the unknowns C and τ the expression of the two closure relations. If we consider the standard form of the PDE systems as in Eq. (7.2.1), the vector of conservative variables is then:

$$\mathbf{Q} = (C\,h + C^*\,z_b, \quad h + z_b, \quad \alpha_{cu}\,C\,h\,U) \tag{7.4.2}$$

while the vector of the primitive variables is assumed to be:

$$\mathbf{V} = (h,\, z_b,\, U) \tag{7.4.3}$$

In the numerical scheme in order to switch from conservative variables to primitive variables, the following relations have been derived exactly:

$$h = \left(\left(\frac{k_c\,Q(3)}{\alpha_{cu}(Q(1) - C^* Q(2))} \right)^2 \right)^{1/3} - d \tag{7.4.4}$$

$$u = Q(3) / \left(\alpha_{cu}\,h\,C^* - \frac{Q(3)\,k_c}{(h)^{1.5}} \right) \tag{7.4.5}$$

$$zb = Q(2) - h \tag{7.4.6}$$

where the coefficient k_c is:

$$kc = \frac{\alpha_{cu} d}{E_1 \sqrt{g}} \tag{7.4.7}$$

Furthermore the only non conservative term is $g\,C\,h\,\partial z_b/\partial x$ in the momentum balance for the solid phase, so that the only term of the **B(Q)** matrix is $g\,C\,h$. Finally we have only one source term **S(Q)**, that is the bed friction component τ_0/ρ.
There is no terms modeling the entrainment contribution, since it is contained directly in the equations through the mobile bed condition ($\partial z_b/\partial t \neq 0$).
We adopted a first order finite volume scheme in space and time; the general discretized form is the following:

$$\mathbf{Q}_i^{n+1} = \mathbf{Q}_i^n - \frac{\Delta t}{\Delta x}\left(\mathbf{f}_{i+\frac{1}{2}} - \mathbf{f}_{i-\frac{1}{2}}\right) - \frac{\Delta t}{\Delta x}\left(\mathbf{D}_{i+\frac{1}{2}} + \mathbf{D}_{i-\frac{1}{2}}\right) + \Delta t \mathbf{S}_i \tag{7.4.8}$$

where D_i contains the contribution of the non-conservative term and it is treated as explained in the previous section for the SPH approach; S indicates the source term and f are the fluxes.

7.4.1 Dambreak problem

The dambreak test is a Riemann problem, characterized by a discontinuity of the free surface of the flow. The initial condition are characterized by a free surface 1.20 m hight on the left of the discontinuity and 1 m on the left.
This type of test is crucial for our system of equations: when all the dry particles are at rest, so that the velocity $U = 0$, $h = 0$ and $C = C^*$, the first two equations of the system collapses on a single one and this gives rise to numerical instabilities. For this reason, as initial condition, we imposed an initial velocity of 1 mm/s instead of zero and the flow depth on the right equal to 1 mm instead of zero too. Fig. 7.15-7.19 show the results of the numerical simulation. First of all, in Fig. 7.15 it is reported the evolution in time of the free surface η: from the initial discontinuity, located at $x = 0$, the material starts to flow downstream, while upstream even more material is mobilized. Finally, the material becomes at rest; at this moment the deposit assumes the slope of the friction angle. This is a good results since it represents a physically based behavior.
Fig. 7.16 shows the bed elevations represented for different instants(the same as the free surface eta). It may be observed that the material when starts to flow creates a deep erosion just after the discontinuity; in few instant however it reduces till $t = 0.25$ s in which starts the deposition of the material.
Clearly the big initial erosion consists of infinitesimal displacement, and do not consist in a real dig. Indeed, the limit between the erodible layer and the moving layer is physically uncertain, so that the great erosion predicted by the model corresponds to an high layer which is moving. If the bed elevation would be defined in a slightly different way, we could obtain a much smaller erosion without a great difference in the flow field. The next Fig. 7.17 shows the instant $t = 0.25$ s, in which the bed elevation starts to correspond to the free surface elevation (that means deposition is taking place). The next variable analyzed is the flow depth h, that is the difference between the free surface and the bed elevation. Clearly, in the first instant it grows till 0.2 m, almost the height of the discontinuity. Then it reduces till zero when the material stops. A similar behavior is shown in Fig. 7.19 for the velocity U: it has a peak in the first instant then it reduces to zero as the material start to deposit. The last variable in Fig. 7.21 is the concentration of the solid phase. There are two main

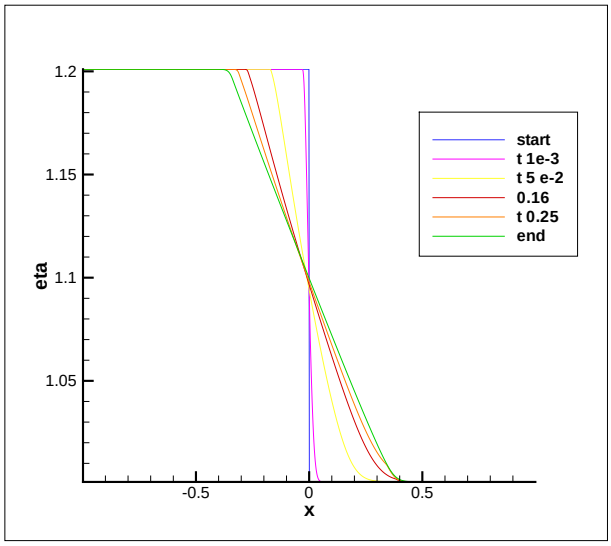

Figure 7.15: *Evolution of the free surface eta [m] of the dam break test.*

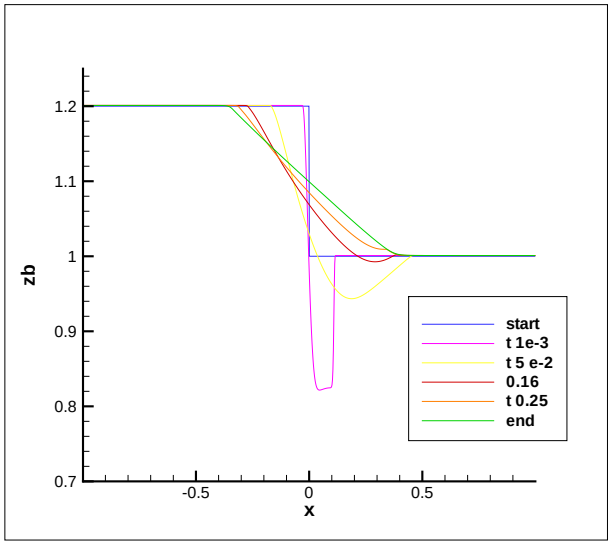

Figure 7.16: *Evolution of bed elevation z_b [m] of the dam break test.*

physical interpretation, which correspond to two main numerical solution, explained in the following. There may be two possible stopping mechanisms: the first one correspond to all the material at rest except for a single layer one diameter depth, moving with velocity almost zero. This means that $h \to d$, $U \to 0$ and in these conditions $C \to 0$.

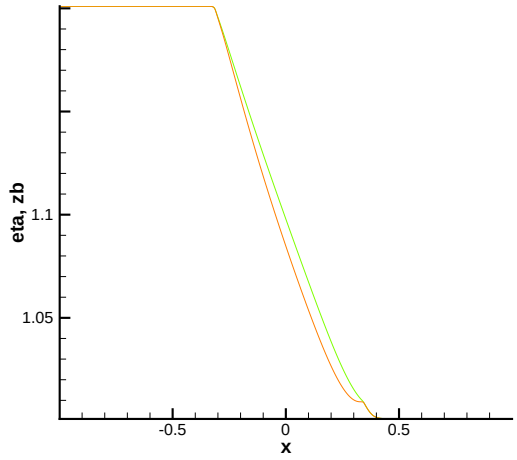

Figure 7.17: *Comparison between the free surface η and bed elevation z_b [m].*

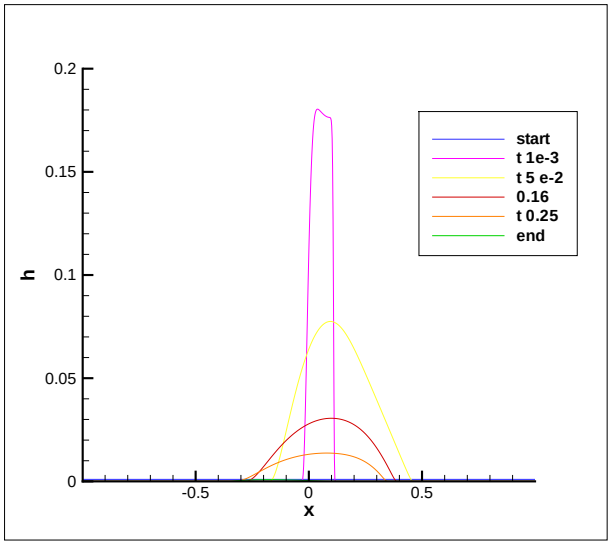

Figure 7.18: *Evolution of the flow depth h [m] of the dam break test.*

From a numerical point of view we have set this condition, by imposing that for $h < d$ the flow stops with $F_r d/h \to 0$ and according to the closure relation the concentration $C \to C^*$. Fig. 7.21 shows the evolution of the concentration for this case: the sharp zone in which C turns into C^* correspond to a flow depth minor that a particle diameter. In the

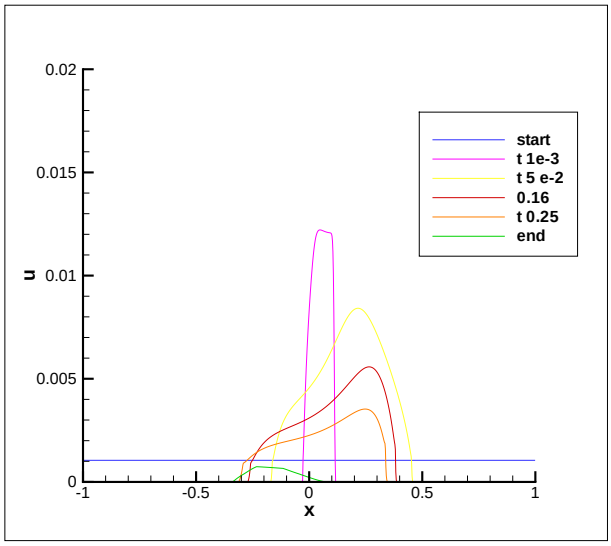

Figure 7.19: *Evolution of the velocity U [m/s] in the dam break test.*

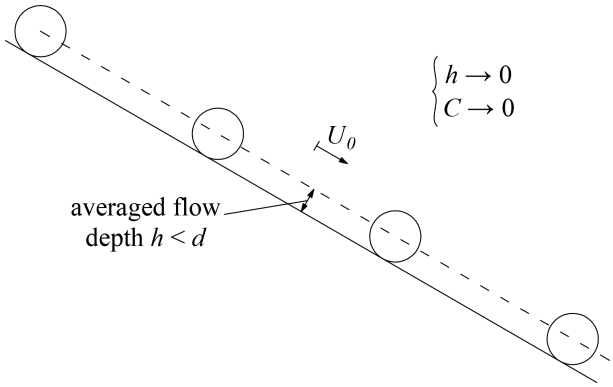

Figure 7.20: *First physical interpretation of the arrest system.*

second scenario, we may consider a flow which is going to stop as an ensemble of particles at rest except for only some of them, far from each other but that are moving with a finite velocity U_0, while the flow depth tends to zero ($h \to 0$).

According to this mechanism, the ratio $F_r\, d/h \to \infty$ and according to the closure relation, $C \to 0$. From a numerical point of view, we have imposed that h tends to zero before the velocity U. This behavior is shown in Fig. 7.23, where the concentration diminishes till zero.

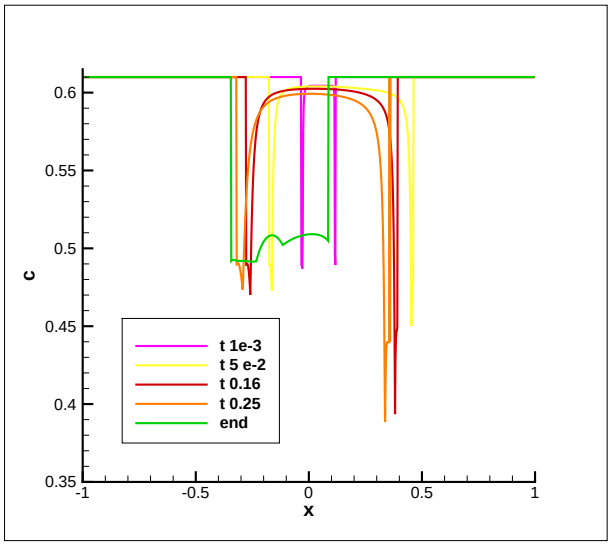

Figure 7.21: *Evolution of the concentration C [%] in the dam break test.*

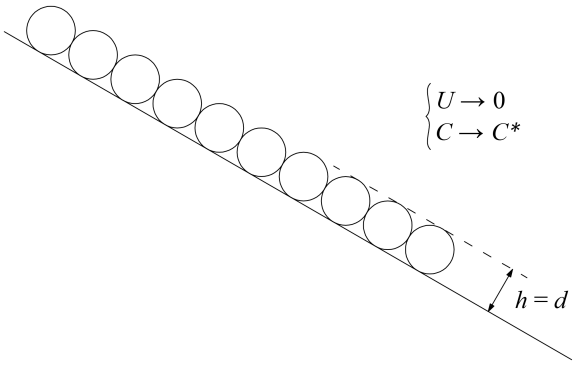

Figure 7.22: *Second physical interpretation of the arrest system.*

Comparison with the experimental results

The numerical solution for the dam break test has been compared to the experimental test described in Chapter 6.
The first good result is the slope of the deposit at the end of test, which is quite the same in the two cases. Fig. 7.24 shows a comparison between the two: the agreement is quite good. The experimental free surface presents a little curvature not reproduced by the numerical solution, but this may due to the wall effect or three dimensional effects, not taken into account in the 1D depth integrated model.

Regarding the velocity, we have compared the numerical result with

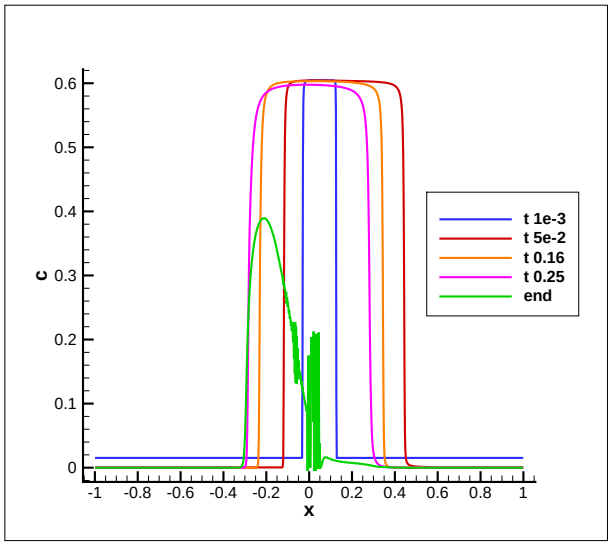

Figure 7.23: *Evolution of the concentration C [%] in the dam break test.*

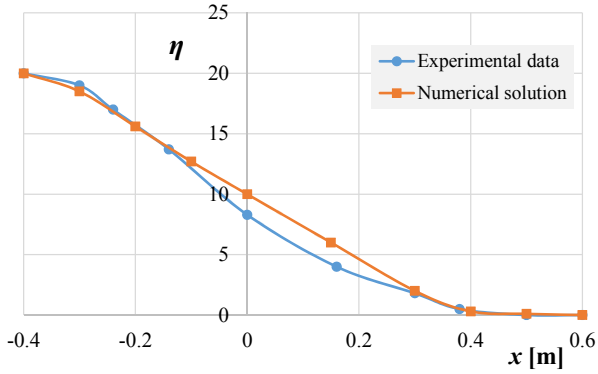

Figure 7.24: *Free surface η at the end of the test: comparison between experimental data and numerical solution*

the experimental data in a section 4 cm downstream the gate. Fig. 7.25 shows the velocity evolutions; the experimental trend has been obtained computing the depth integrated velocity on the flow depth, which is the distance between the free surface and the point where the velocity is 1% of the maximum velocity on the free surface.

The Figure shows a great difference between the maximum velocity experimentally measured and that obtained through the numerical simulation. This is reasonably due to the uncertainties in determining the bed elevation: as previously observed and explained, the numerical solution

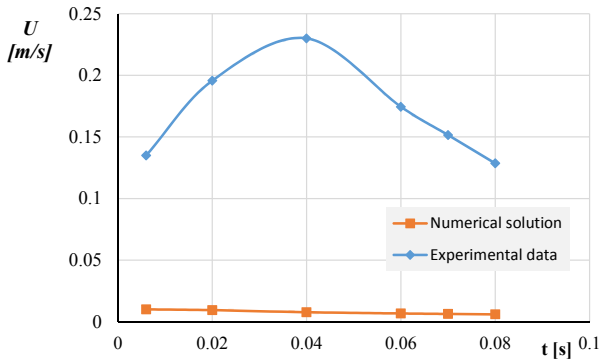

Figure 7.25: *Depth integrated velocity U at 4 cm from the gate: numerical solution and experimental data*

considers, in the first instants, a bed elevation much lower with respect to the experimental data.
If we assume that the conventional bed elevation is that predicted by the numerical model, we should recalculate the depth-average velocity, averaging it on a depth equal to that of the numerical model (which is major then the experimental one), by assuming that in the added depth, the velocity has values close to 1 % of the measured maximum velocity.In such a way, we obtain values of the depth-averaged velocity similar to those predicted by the numerical model, as reported in Fig. 7.26.
Anyway, there is still a difference in the shape of the velocity evolution;

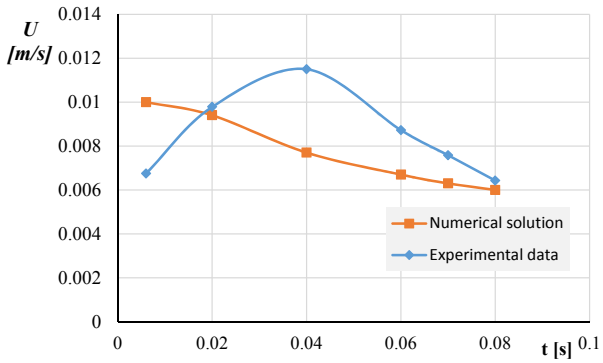

Figure 7.26: *Depth integrated velocity U at 4 cm from the gate: numerical solution and experimental data*

this is reasonably due to the fact that in the real dam break the gate is removed not instantaneously as occur in the numerical simulation. For this reason in the experiments the velocity starts from a lower value, then reaches a maximum and then decreases, while in the numerical simula-

tion the maximum is reached in the first instant and then the velocity gradually decreases.

7.4.2 Uniform flow with upstreams perturbation of the flow rate

The second test case we analyzed is the uniform flow condition in an inclined channel, inserting a periodic perturbation in the upstreams flow rate. In other words, the upstreams boundary condition consists of a flow rate (that corresponds to the third conservative variable Q(3)) defined as follow:

$$Q(3,t) = Q(3,0) + a\sin(\omega\, t) \tag{7.4.9}$$

with $a = 2e-3$ and $\omega = 2\pi/0.1$; t stands for time of the simulation. Figs. 7.27-7.30 show the results. All the variable are characterized by a periodic fluctuation, due to the boundary condition imposed for the flow rate. Near the left boundary the perturbation is greater, while going to the right it is damped and tends to the equilibrium. Regarding the

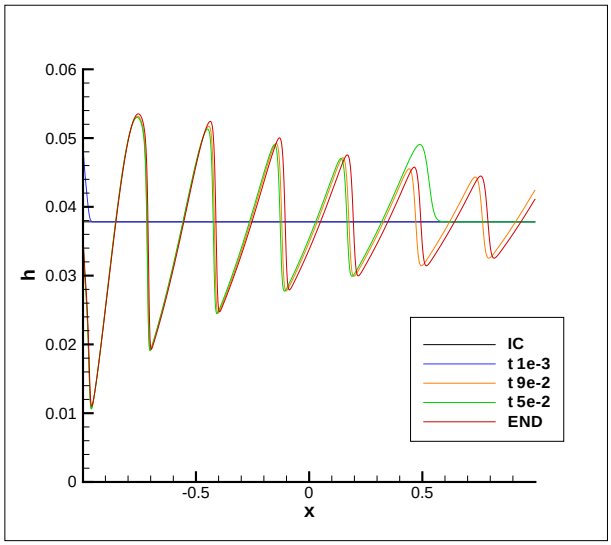

Figure 7.27: *Flow depth h[m] along a channel fed with periodic flow rate.*

bed elevation z_b, it is affected by fluctuations too. In particular it is characterized by the formation of dunes, which tend to disappear far from the left boundary.

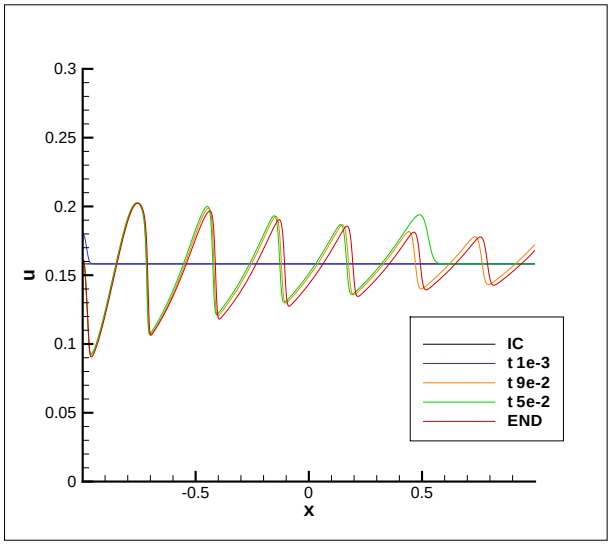

Figure 7.28: *Velocity U [m/s] along a channel fed with periodic flow rate.*

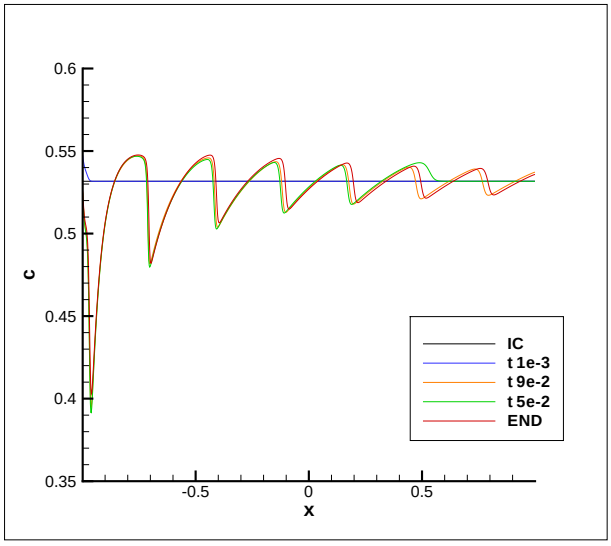

Figure 7.29: *Concentration evolution along a channel fed with periodic flow rate.*

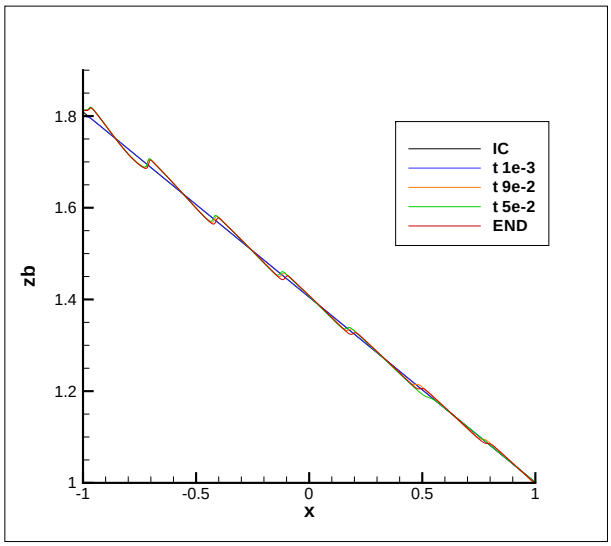

Figure 7.30: *Bed elevation z_b [m] along a channel fed with periodic flow rate.*

Conclusions and future developments

The thesis has been focused on the mechanics of dry granular flows: different aspects of these phenomenon have been analyzed, both through experimental investigation and numerical simulations.
The most diffused theory applied to study the mechanics of dry granular flows is that derived from kinetic theory of gases: the particles of granular material are assimilated to molecules in a gas. However we observed that some hypotheses of this approach do not hold for the granular case, e.g. in macroscopic granular flows the particles dimensions are comparable to that of the control volume and the system is not ergodic as for gases. The ergodicity property means that the average of a process variable made over time, over space and over the whole statistical ensemble coincides: due to the lack of strong scale separation, the number of particles in the control volume can not be considered constant (few particles may change significantly velocity and concentration in the control volume). This means that different results may be obtained, according as the average is done over time, space or statistical ensemble. For these reasons the averaging process becomes crucial: we have shown that by applying an averaging process that takes into account the lack of scale separation, the continuity equation (in uniform channel flow condition) show a vertical velocity gradient different from zero. This result seems to be proved from the experimental data, that shows vertical velocity profile with an average value different from zero. Anyway, since in our experiments the transversal gradients can not be neglected, this aspect should be investigated deeply in order to exclude possible secondary circulation.
A second aspect analyzed is the possibility to write a system of equations integrated over an area or over the depth, capable of simulating, through the mass and momentum balances, the erosion and deposition processes. Several mathematical models are present in literature to study dry granular flows: they are all based on the integration of the mass and

momentum balance. Each model is then characterized by proper closure relation or further terms accounting for the entrainment phenomenon.
A 1D depth integrated model has been developed within this thesis: it is based on the integration of the mass balance (for solid phase and for the total mass, air and solid) and of the momentum balance, assuming the iso-kinetic hypothesis (the air velocity is the same of the solid velocity). In this way, a mobile bed condition has been introduced so that the bed elevation may change in time: this is a very innovative aspect, that allows to account for the entrainment without further ad-hoc empirical assumptions.
In order to close the system of equations, two closure relations are needed. These relations have been derived from kinetic theories, but inserting the frictional contribution too (long-lasting and multiple contacts among particles at high concentrations): we have inserted a modulating function f_0 that allow the coexistence and intermittency between the two regimes. Through this analysis we found that the concentration depends on two main parameters: the Froude number and the ratio d/h (with d the particles diameter and h the flow depth). Accordingly, we performed a series of experiments in uniform channel flow condition in order to calibrate the closure relations, together with some molecular dynamic simulations that allowed us to have some 3D view of the flow. Then, we derived the second closure relation by considering the bed shear stress balanced by the parallel to the bed component of the pressure.
Finally, we developed a finite volume numerical scheme to solve our mathematical model. In particular we solve our system of equations through a path conservative finite volume scheme and the numerical results are quite good. Two main test cases have been analyzed: the dam break test and the uniform channel flow condition with upstreams periodic fluctuation of the flow rate. In particular the dam break test has been compared with experimental data: the free surface profile at the end of the simulation is in agreement with the experimental one, that is it assumes the slope corresponding to the repose angle. Regarding the velocity, the difference is quite large: this is due to the fact that in the first instants (near flow field) the phenomenon is strongly 3D while the numerical model is depth integrated in 1D. Furthermore, in the experiments the definition of the bed elevation is very uncertain, since the velocity tends asymptotically to zero. A small variation of the velocity that we usually consider negligible implies a great change in the value of the bed elevation.

Starting from the work developed in this thesis, further experimental investigation should be carried out in order to verify the problem of lack of scale separation pointed out in this works. In particular, the correla-

tion between the velocity fluctuations and concentration fluctuations is of major interest to verify this problem.
Regarding the mathematical and numerical model, we have derived the system of equations accounting for the free surface and bed slopes; the next step would be inserting this contribution into the numerical model. Furthermore, it will be straightforward the insertion of a variable width of the channel, by adding the variable $B(x)$ in the system. Once these two aspect have been introduced, the further improvement will be the extension to the 2D depth integrated modeling.
Finally, we have inserted a function f_0 to model the coexistence of the collisional and frictional regime: it would be interesting to deepen the behavior and formulation of this function. We think that this could be done both through the experimental investigation and the molecular dynamics simulations.

Appendices

Appendix A

Eigenvalues of the system

The eigenvalues of the mathematical model have been analyzed, in order to verify that the system is hyperbolic and that three real and different eigenvalues exist. The analysis has been carried out for different Froude numbers and for different ratio between the particles diameter and flow depth d_p/h.

A.1 Complete form of the system: re-arrangement for the time derivatives

In order to have a single time derivative in each equation, the idea is to compute the single time derivative as a function of the other and substitute it in the other equations. In the end, we have a system with only one time derivative for equation. The system will look as follows:

$$\begin{cases} \dfrac{\partial h}{\partial t} + A_{11}\dfrac{\partial h}{\partial x} + A_{12}\dfrac{\partial u}{\partial x} + A_{13}\dfrac{\partial z_b}{\partial x} = B_1 \\ \dfrac{\partial U}{\partial t} + A_{21}\dfrac{\partial h}{\partial x} + A_{22}\dfrac{\partial u}{\partial x} + A_{23}\dfrac{\partial z_b}{\partial x} = B_2 \\ \dfrac{\partial z_b}{\partial t} + A_{31}\dfrac{\partial h}{\partial x} + A_{32}\dfrac{\partial u}{\partial x} + A_{33}\dfrac{\partial z_b}{\partial x} = B_3 \end{cases} \tag{A.1.1}$$

The coefficient are the following:

$$A_{11} = +\frac{1}{C_h}\left(\alpha U^2 C^* + \frac{\alpha U C C^*}{\partial C/\partial U} - \frac{\alpha^2 U C^2}{\partial C/\partial U} - \alpha^2 U^2 C - \frac{\alpha^2 C U h}{\partial C/\partial U}\frac{\partial C}{\partial h}\right.$$
$$\left. - \alpha^2 U^2 h\frac{\partial C}{\partial h} + C U^2 \beta_2 + U^2 h \beta_2 \frac{\partial C}{\partial h} + \frac{g h^2}{2}\frac{\partial C}{\partial h} + g C h\right) \tag{A.1.2}$$

with C_h defined here below:

$$C_h = -\frac{\partial C}{\partial h}\frac{\alpha C h}{\partial C/\partial U} - (C - C^*)\left[\frac{\alpha C}{\partial C/\partial U} + \alpha U\right] + \alpha U C \tag{A.1.3}$$

By simplifying it, we obtain:

$$C_h = -\frac{\partial C/\partial h}{\partial C/\partial U}\alpha_{cu} C h - (C - C^*)\left[\frac{\alpha C}{\partial C/\partial U}\right] + \alpha_{cu} U C^* \tag{A.1.4}$$

$$A_{12} = +\frac{1}{C_h}\left(\frac{C^* \alpha C h}{\partial C/\partial U} + C^* \alpha U h - \alpha^2 C U h - \alpha^2 U^2 h\frac{\partial C}{\partial U} - \frac{\alpha C^2 h}{\partial C/\partial U}\right.$$
$$\left. - \alpha^2 C U h + 2 C h U \beta_2 + U^2 h \beta_2 \frac{\partial C}{\partial U} + \frac{g h^2}{2}\frac{\partial C}{\partial U}\right) \tag{A.1.5}$$

$$A_{13} = +\frac{h g C}{C_h} \tag{A.1.6}$$

$$A_S = -\frac{\tau}{\rho C_h} \tag{A.1.7}$$

$$A_{21} = -\frac{U C^*}{h\partial C/\partial U} + \frac{\alpha U \partial C/\partial h}{\partial C/\partial U} + \frac{\alpha U C}{h\partial C/\partial U} +$$
$$- \frac{1}{C_h}\left(\frac{(C - C^*) + h\partial C/\partial h}{h\partial C/\partial U}\right)\left(\frac{\alpha U C C^*}{\partial C/\partial U} + \alpha U^2 C^* - \frac{\alpha^2 C^2 U}{\partial C/\partial U} + \right.$$
$$- \alpha^2 U^2 C - \frac{\alpha^2 C U h}{\partial C/\partial U}\frac{\partial C}{\partial h} - \alpha^2 U^2 h\frac{\partial C}{\partial h} + C U^2 \beta_2 + U^2 h \beta_2 \frac{\partial C}{\partial h} +$$
$$\left. + \frac{g h^2}{2}\frac{\partial C}{\partial h} + g C h\right) \tag{A.1.8}$$

$$A_{22} = -\frac{C^*}{\partial C/\partial U} + \alpha U + \frac{\alpha C}{\partial C/\partial U} + \\ -\frac{1}{C_h}\left(\frac{(C-C^*)+h\partial C/\partial h}{h\partial C/\partial U}\right)\left(\frac{\alpha h C C^*}{\partial C/\partial U} + \alpha U h C^* - \alpha^2 U h C + \right. \\ -\alpha^2 U^2 h\frac{\partial C}{\partial U} - \frac{\alpha^2 C^2 h}{\partial C/\partial U} - \alpha^2 C U h + 2ChU\beta_2 \\ \left. + U^2 h\beta_2\frac{\partial C}{\partial U} + \frac{gh^2}{2}\frac{\partial C}{\partial U}\right) \tag{A.1.9}$$

$$A_{23} = -\frac{gC}{C_h}\left(\frac{(C-C^*)+h\partial C/\partial h}{\partial C/\partial U}\right) \tag{A.1.10}$$

$$B_S = +\frac{\tau_0}{\rho C_h}\left(\frac{(C-C^*)+h\partial C/\partial h}{h\partial C/\partial U}\right) \tag{A.1.11}$$

$$A_{31} = -\frac{1}{C_h}\left(\alpha U^2 C^* + \frac{\alpha U C C^*}{\partial C/\partial U} - \frac{\alpha^2 U C^2}{\partial C/\partial U} - \alpha^2 U^2 C - \frac{\alpha^2 C U h}{\partial C/\partial U}\frac{\partial C}{\partial h}\right. \\ \left. - \alpha^2 U^2 h\frac{\partial C}{\partial h} + C U^2\beta_2 + U^2 h\beta_2\frac{\partial C}{\partial h} + \frac{gh^2}{2}\frac{\partial C}{\partial h} + gCh\right) + U \tag{A.1.12}$$

$$A_{32} = -\frac{1}{C_h}\left(\frac{C^*\alpha C h}{\partial C/\partial U} + C^*\alpha U h - \alpha^2 C U h - \alpha^2 U^2 h\frac{\partial C}{\partial U} - \frac{\alpha C^2 h}{\partial C/\partial U}\right. \\ \left. - \alpha^2 C U h + 2ChU\beta_2 + U^2 h\beta_2\frac{\partial C}{\partial U} + \frac{gh^2}{2}\frac{\partial C}{\partial U}\right) + h \tag{A.1.13}$$

$$A_{33} = -\frac{hgC}{C_h} \tag{A.1.14}$$

$$D_S = +\frac{\tau}{\rho C_h} \tag{A.1.15}$$

We may write the system in the standard form, with $\mathbf{A}_Q$ as follows:

$$\mathbf{A}_Q = \begin{bmatrix} A_h & A_U & A_z \\ B_h & B_U & B_z \\ D_h & D_U & D_z \end{bmatrix} = \begin{bmatrix} A_{11} & A_{12} & A_{13} \\ A_{21} & A_{22} & A_{23} \\ A_{31} & A_{32} & A_{33} \end{bmatrix}$$

Now we compute the determinant of the matrix:

$$\det(\mathbf{A}_Q - \lambda\mathbf{I}) = 0 \tag{A.1.16}$$

So the polynomial equation we obtain is:

$$\begin{aligned}(A_{11}-\lambda)(A_{22}-\lambda)(A_{33}-\lambda) + A_{12}A_{23}A_{31} + A_{13}A_{21}A_{32} \\ - A_{31}(A_{22}-\lambda)A_{13} - A_{32}(A_{11}-\lambda)A_{23} - A_{21}(A_{33}-\lambda)A_{12} = 0\end{aligned} \tag{A.1.17}$$

By multiplying the terms:

$$\begin{aligned}&-\lambda^3 + \lambda^2(A_{11}+A_{22}+A_{33}) \\ &+ \lambda(A_{31}A_{13} + A_{32}A_{23} + A_{21}A_{12} - A_{11}A_{22} - A_{11}A_{33} - A_{22}A_{33}) \\ &+ A_{12}A_{23}A_{31} + A_{13}A_{21}A_{32} - A_{31}A_{22}A_{13} - A_{32}A_{23}A_{11} - A_{33}A_{21}A_{12} \\ &+ A_{11}A_{22}A_{33} = 0\end{aligned} \tag{A.1.18}$$

The dimension of this equation is, for example, that of the product $A_{11}A_{22}A_{33}$:

- $A_{11} = A_h = [m/s]$
- $A_{22} = B_U = [m/s]$
- $A_{33} = D_z = [m/s]$

So the final dimension is m^3/s^3. In order to make dimensionless this equation we may divide everything by $(gh)^{1.5}$. Anyway, in the following procedure, I have decided to make dimensionless each single coefficient first; for this reason each coefficient is divided for a different quantity. Then, by solving the polynomial dimensionless equation, we may see the evolution of the dimensionless eigenvalues.

The closure relation of C, expressing it as a function of the areal average values U and h, is:

$$C = C^* \frac{E_1}{E_1 + \alpha_{cu} \frac{U}{\sqrt{gh}} \frac{d}{h}} \tag{A.1.19}$$

It follows that the expression for the partial derivative of C with respect to U is:

$$\frac{\partial C}{\partial U} = -\frac{\frac{\alpha_{cu}}{\sqrt{gh}} \frac{d}{h} C^* E_1}{(E_1 + \frac{\alpha_{cu}}{\sqrt{gh}} \frac{d}{h} U)^2} \tag{A.1.20}$$

and the expression for the partial derivative of C with respect to h is:

$$\frac{\partial C}{\partial h} = \frac{1.5\, C^*\, E_1 \frac{\alpha_{cu} U d}{\sqrt{g}} \frac{1}{h^{2.5}}}{\left(E_1 + \frac{\alpha_{cu} U d}{\sqrt{g}} \frac{1}{h^{1.5}}\right)^2} \tag{A.1.21}$$

So we may simplify the previous expressions in the following form:

$$E_1 + \alpha_{cu} \frac{U}{\sqrt{gh}} \frac{d}{h} = \frac{C^*}{C} E_1 \tag{A.1.22}$$

By substituting this term in Eqs. (A.1.20) and (A.1.21), the new formulations are:

$$\frac{\partial C}{\partial U} = -\frac{\frac{\alpha_{cu}}{\sqrt{gh}} \frac{d}{h} C^* E_1}{\left(\frac{C^*}{C} E_1\right)^2} = -\frac{C^2}{C^*} \frac{\alpha_{cu}}{E_1 \sqrt{gh}} \frac{d}{h} \tag{A.1.23}$$

$$\frac{\partial C}{\partial h} = \frac{1.5\, C^* E_1 \frac{\alpha_{cu} U d}{\sqrt{g}} \frac{1}{h^{2.5}}}{\left(\frac{C^*}{C} E_1\right)^2} = 1.5 \frac{C^2}{C^*} \frac{\alpha_{cu}}{E_1 h} \frac{d}{h} \frac{U}{\sqrt{gh}} \tag{A.1.24}$$

The ratio between the two derivatives is:

$$\frac{\partial C / \partial h}{\partial C / \partial U} = \frac{1.5 \frac{C^2}{C^*} \frac{\alpha_{cu}}{E_1 h} \frac{d}{h} \frac{U}{\sqrt{gh}}}{-\frac{C^2}{C^*} \frac{\alpha_{cu}}{E_1 \sqrt{gh}} \frac{d}{h}} = -\frac{3}{2} \frac{U}{h} \tag{A.1.25}$$

First of all we start to make dimensionless the term C_h. Simplifying the term introducing th expressions (A.1.23) and (A.1.24), the following coefficient is obtained:

$$\widetilde{C_h} = F_r \alpha_{cu} (1.5C + C^*) + (C - C^*) \frac{C^*}{C} E_1 \frac{h}{d} \tag{A.1.26}$$

The second term analyzed is A_{11}. I divided the term in 10 sub-term, all made dimensionless by dividing by gh and using Eq. (A.1.23) and Eq. (A.1.24) :

$$\begin{cases} 1. \\ \frac{\alpha_{cu}U^2C^*}{gh} = \alpha_{cu}C^*F_r^2 \\ 2. \\ \frac{\alpha_{cu}UCC^*}{-C^2\alpha_{cu}d}C^*E_1\sqrt{gh}\,h\frac{1}{gh} = -E_1\frac{C^{*2}}{C}\frac{h}{d}F_r \\ 3. \\ -\frac{\alpha_{cu}^2UC^2}{-C^2\alpha_{cu}d}C^*E_1\sqrt{gh}\,h\frac{1}{gh} = +\alpha_{cu}E_1\,C^*\frac{h}{d}\,F_r \\ 4. \\ -\alpha_{cu}^2U^2C\frac{1}{gh} = -\alpha_{cu}^2F_r^2C \\ 5. \\ -\frac{\alpha_{cu}^2CUh}{-C^2\alpha_{cu}d}C^*E_1\sqrt{gh}\,h\,1.5\frac{C^2}{C^*}\frac{\alpha_{cu}}{E_1\,h}\frac{d}{h}\frac{U}{\sqrt{gh}}\frac{1}{gh} = 1.5\alpha_{cu}^2CF_r^2 \\ 6. \\ \alpha_{cu}^2U^2h\,1.5\frac{C^2}{C^*}\frac{1}{E_1}\frac{\alpha_{cu}}{h}\frac{d}{h}\frac{U}{\sqrt{gh}}\frac{1}{gh} = -1.5\,\frac{C^2}{C^*}\frac{\alpha_{cu}^3}{E_1}\frac{d}{h}F_r^3 \\ 7. \\ CU^2\beta_2\frac{1}{gh} = \beta_2CF_r^2 \\ 8. \\ U^2h\beta_2 1.5\frac{C^2}{C^*}\frac{1}{E_1}\frac{\alpha_{cu}}{h}\frac{d}{h}\frac{U}{\sqrt{gh}}\frac{1}{gh} = 1.5\beta_2\frac{C^2}{C^*}\frac{\alpha_{cu}}{E_1}\frac{d}{h}F_r^3 \\ 9. \\ \frac{gh^2}{2}1.5\frac{C^2}{C^*}\frac{1}{E_1}\frac{\alpha_{cu}}{h}\frac{d}{h}\frac{U}{\sqrt{gh}}\frac{1}{gh} = \frac{3}{4}\frac{C^2}{C^*}\frac{\alpha_{cu}}{E_1}\frac{d}{h}F_r \\ 10. \\ ghC\frac{1}{gh} = C \end{cases} \tag{A.1.27}$$

The final formulation of A_{11} is:

$$A_{11} = \frac{1}{\tilde{C}_h}\Bigg[\alpha_{cu}C^*F_r^2 - E_1\frac{C^{*2}}{C}\frac{h}{d}F_r + \alpha_{cu}E_1\,C^*\frac{h}{d}\,F_r - \alpha_{cu}^2F_r^2C + \\ + 1.5\alpha_{cu}^2CF_r^2 - 1.5\,\frac{C^2}{C^*}\frac{\alpha_{cu}^3}{E_1}\frac{d}{h}F_r^3 + \beta_2CF_r^2 + 1.5\beta_2\frac{C^2}{C^*}\frac{\alpha_{cu}}{E_1}\frac{d}{h}F_r^3 + \\ + \frac{3}{4}\frac{C^2}{C^*}\frac{\alpha_{cu}}{E_1}\frac{d}{h}F_r + C\Bigg] \tag{A.1.28}$$

$$A_{11} = \frac{1}{\tilde{C}_h}\Bigg[F_r^2(\alpha_{cu}C^* + [\frac{1}{2}\alpha_{cu}^2 + \beta_2]C) + F_r^3\frac{3}{2}\frac{C^2}{C^*}\frac{\alpha_{cu}}{E_1}\frac{d}{h}(\beta_2 - \alpha_{cu}^2) + \\ + F_r\,E_1\,C^*\frac{h}{d}\left(\alpha_{cu} - \frac{C^*}{C} + \frac{3}{4}\frac{C^2}{(C^*)^2}\frac{\alpha_{cu}}{E_1^2}\left(\frac{d}{h}\right)^2\right) + C\Bigg] \tag{A.1.29}$$

The third term analyzed is $A_{12} = A_U$. I divided the term in 9 subterms, all made dimensionless by dividing by $\sqrt{gh}\,h$ and always using

Eq. (A.1.23) and Eq. (A.1.24) :

$$\begin{cases} 1. \\ \dfrac{\alpha_{cu}C^*Ch}{-C^2\alpha_{cu}d}C^*E_1\sqrt{gh}\,h\dfrac{1}{\sqrt{gh}\,h} = -E_1\dfrac{C^{*2}}{C}\dfrac{h}{d} \\ 2. \\ C^*\alpha_{cu}Uh\dfrac{1}{\sqrt{gh}\,h} = C^*\alpha_{cu}F_r \\ 3. \\ -C\alpha_{cu}^2Uh\dfrac{1}{\sqrt{gh}\,h} = -C\alpha_{cu}^2F_r \\ 4. \\ -\alpha_{cu}^2U^2h\left(-\dfrac{C^2\alpha_{cu}d}{C^*E_1\sqrt{gh}\,h}\right)\dfrac{1}{\sqrt{gh}\,h} = +\dfrac{\alpha_{cu}^3}{E_1}\dfrac{C^2}{C^*}\dfrac{d}{h}F_r^2 \\ 5. \\ -\dfrac{\alpha_{cu}C^2h}{-C^2\alpha_{cu}d}C^*E_1\sqrt{gh}\,h\dfrac{1}{\sqrt{gh}\,h} = +C^*\,E_1\dfrac{h}{d} \\ 6. \\ -\alpha_{cu}^2CUh\dfrac{1}{\sqrt{gh}\,h} = -\alpha_{cu}^2CF_r \\ 7. \\ 2ChU\beta_2\dfrac{1}{\sqrt{gh}\,h} = 2C\beta_2F_r \\ 8. \\ \beta_2U^2h\left(-\dfrac{C^2\alpha_{cu}d}{C^*E_1\sqrt{gh}\,h}\right)\dfrac{1}{\sqrt{gh}\,h} = -\dfrac{\alpha_{cu}\beta_2}{E_1}\dfrac{C^2}{C^*}\dfrac{d}{h}F_r^2 \\ 9. \\ \dfrac{gh^2}{2}\left(-\dfrac{C^2\alpha_{cu}d}{C^*E_1\sqrt{gh}\,h}\right)\dfrac{1}{\sqrt{gh}\,h} = -\dfrac{\alpha_{cu}}{2}\dfrac{C^2}{C^*}\dfrac{1}{E_1}\dfrac{d}{h} \end{cases} \tag{A.1.30}$$

So finally we obtain:

$$\begin{aligned} A_{12} = \frac{1}{\tilde{C}_h}\Bigg[& -E_1\frac{C^{*2}}{C}\frac{h}{d} + C^*\alpha_{cu}F_r - C\alpha_{cu}^2F_r + \frac{\alpha_{cu}^3}{E_1}\frac{C^2}{C^*}\frac{d}{h}F_r^2 + \\ & + C^*\,E_1\frac{h}{d} - \alpha_{cu}^2CF_r + 2C\beta_2F_r - \frac{\alpha_{cu}\beta_2}{E_1}\frac{C^2}{C^*}\frac{d}{h}F_r^2 - \frac{\alpha_{cu}}{2}\frac{C^2}{C^*}\frac{1}{E_1}\frac{d}{h}\Bigg] \end{aligned} \tag{A.1.31}$$

By simplifying the expression:

$$A_{12} = \frac{1}{\tilde{C}_h}\left[F_r(\alpha_{cu}(C^* - 2\alpha_{cu}C) + 2C\beta_2) + F_r^2\frac{\alpha_{cu}}{E_1}\frac{d}{h}\frac{C^2}{C^*}(\alpha_{cu}^2 - \beta_2) + \right.$$
$$\left. + \frac{h}{d}E_1C^*\left(1 - \frac{C^*}{C}\right) - \frac{\alpha_{cu}}{2}\frac{C^2}{C^*}\frac{1}{E_1}\frac{d}{h}\right] \tag{A.1.32}$$

The last coefficient for the first equation is A_{13}, which is simply made dimensionless by dividing by gh, obtaining $A_{13} = C/\tilde{C}_h$.

Now the second equation coefficients: we may start from A_{21}, that has been split into 15 sub-terms. The first three terms has dimension m/s^2, so they has been divided by g; the following two has been divided by $\sqrt{gh}/h$ and finally the last 10 terms are made dimensionless through gh.

$$
\begin{cases}
1. \\
-\dfrac{\alpha_{cu}UC^*}{h(-C^2\alpha_{cu}d)}C^*E_1\sqrt{gh}\,h\dfrac{1}{g} = +\dfrac{E_1}{\alpha_{cu}}\left(\dfrac{C^*}{C}\right)^2\dfrac{h}{d}F_r \\
2. \\
\alpha_{cu}U\left(-\dfrac{3}{2}\dfrac{U}{h}\right)\dfrac{1}{g} = -1.5\,\alpha_{cu}F_r^2 \\
3. \\
\dfrac{+\alpha_{cu}UC}{h\left(-\frac{C^2}{C^*}\frac{1}{E_1}\frac{\alpha_{cu}}{\sqrt{gh}}\frac{d}{h}\right)}\dfrac{1}{g} = -\dfrac{C^*}{C}E_1\dfrac{h}{d}F_r \\
4. \\
\dfrac{(C-C^*)}{h}\dfrac{C^*E_1\sqrt{gh}\,h}{-C^2\alpha_{cu}d}\dfrac{h}{\sqrt{gh}} = \dfrac{E_1}{\alpha_{cu}}\dfrac{h}{d}\dfrac{C^*}{C}\left(\dfrac{C^*}{C}-1\right) \\
5. \\
h\left(-\dfrac{3}{2}\dfrac{U}{h}\right)\dfrac{h}{\sqrt{gh}} = -1.5F_r \\
6. \\
\dfrac{\alpha_{cu}UCC^*}{-C^2\alpha_{cu}d}C^*E_1\sqrt{gh}\,h\dfrac{1}{gh} = -E_1\dfrac{C^{*2}}{C}\dfrac{h}{d}F_r \\
7. \\
\alpha_{cu}U^2C^*\dfrac{1}{gh} = \alpha_{cu}C^*F_r^2 \\
8. \\
\dfrac{-\alpha_{cu}^2UC^2}{-C^2\alpha_{cu}d}C^*E_1\sqrt{gh}\,h\dfrac{1}{gh} = +\alpha_{cu}\,E_1\,C^*\dfrac{h}{d}F_r \\
9. \\
-\alpha_{cu}^2U^2C\dfrac{1}{gh} = -\alpha_{cu}^2CF_r^2 \\
10. \\
-\alpha_{cu}^2CUh\left(-\dfrac{3}{2}\dfrac{U}{h}\right)\dfrac{1}{gh} = 1.5\alpha_{cu}^2C\,F_r^2 \\
11. \\
-\alpha_{cu}^2U^2h\,1.5\dfrac{C^2}{C^*}\dfrac{\alpha_{cu}}{E_1\,h}\dfrac{d}{h}\dfrac{U}{\sqrt{gh}}\dfrac{1}{gh} = -1.5\dfrac{\alpha_{cu}^3}{E_1}\dfrac{C^2}{C^*}\dfrac{d}{h}F_r^3
\end{cases}
\tag{A.1.33}
$$

$$\begin{cases} 12. \\ \beta_2 U^2 C \dfrac{1}{gh} = \beta_2 C F_r^2 \\ 13. \\ \beta_2 U^2 h\, 1.5 \dfrac{C^2}{C^*} \dfrac{\alpha_{cu}}{E_1} \dfrac{h}{h} \dfrac{d}{h} \dfrac{U}{\sqrt{gh}} \dfrac{1}{gh} = 1.5 \dfrac{\beta_2 \alpha_{cu}}{E_1} \dfrac{C^2}{C^*} \dfrac{d}{h} F_r^3 \\ 14. \\ \dfrac{gh^2}{2} 1.5 \dfrac{C^2}{C^*} \dfrac{\alpha_{cu}}{E_1} \dfrac{h}{h} \dfrac{d}{h} \dfrac{U}{\sqrt{gh}} \dfrac{1}{gh} = \dfrac{3}{4} \dfrac{\alpha_{cu}}{E_1} \dfrac{C^2}{C^*} \dfrac{d}{h} F_r \\ 15. \\ gCh \dfrac{1}{gh} = C \end{cases} \tag{A.1.34}$$

The sum of all terms is:

$$\begin{aligned} A_{21} =& \frac{E_1}{\alpha_{cu}} \left(\frac{C^*}{C} \right)^2 \frac{h}{d} F_r - 1.5\, \alpha_{cu} F_r^2 - \frac{C^*}{C} E_1 \frac{h}{d} F_r + \\ & - \frac{1}{\tilde{C_h}} \left(\frac{E_1}{\alpha_{cu}} \frac{h}{d} \frac{C^*}{C} \left(\frac{C^*}{C} - 1 \right) - 1.5 F_r \right) \Bigg[- E_1 \frac{C^{*2}}{C} \frac{h}{d} F_r + \\ & + \alpha_{cu} C^* F_r^2 + \alpha_{cu}\, E_1\, C^* \frac{h}{d} F_r - \alpha_{cu}^2 C F_r^2 + 1.5 \alpha_{cu}^2 C\, F_r^2 + \\ & - 1.5 \frac{\alpha_{cu}^3}{E_1} \frac{C^2}{C^*} \frac{d}{h} F_r^3 + \beta_2\, C\, F_r^2 + 1.5 \frac{\beta_2 \alpha_{cu}}{E_1} \frac{C^2}{C^*} \frac{d}{h} F_r^3 + \frac{3}{4} \frac{\alpha_{cu}}{E_1} \frac{C^2}{C^*} \frac{d}{h} F_r + \\ & + C \Bigg] \end{aligned} \tag{A.1.35}$$

Finally:

$$\begin{aligned} A_{21} =& F_r \frac{C^*}{C} E_1 \frac{h}{d} \left(\frac{1}{\alpha_{cu}} \frac{C^*}{C} - 1 \right) - 1.5\, \alpha_{cu} F_r^2 - \frac{1}{\tilde{C_h}} \left(\frac{E_1}{\alpha_{cu}} \frac{h}{d} \frac{C^*}{C} \left(\frac{C^*}{C} - 1 \right) + \right. \\ & \left. - 1.5 F_r \right) \Bigg[F_r \frac{h}{d} C^* E_1 \left(\alpha_{cu} - \frac{C^*}{C} + \frac{3}{4} \left(\frac{C}{C^*} \right)^2 \frac{\alpha_{cu}}{E_1^2} \left(\frac{d}{h} \right)^2 \right) + \\ & + F_r^2 (\alpha_{cu} C^* + C(1/2 \alpha_{cu}^2 + \beta_2)) + F_r^3 \frac{3}{2} \frac{\alpha_{cu}}{E_1} \frac{C^2}{C^*} \frac{d}{h} (\beta_2 - \alpha_{cu}^2) + C \Bigg] \end{aligned} \tag{A.1.36}$$

The second term of the second equation is A_{22}. The first three terms have dimension m/s, so they have been divided by $\sqrt{gh}$; the following

two terms have been divided by $\sqrt{gh}/h$ and finally the last 10 terms are made dimensionless through $\sqrt{gh}\,h$.

$$
\begin{cases}
1. \\
-C^* \dfrac{C^* E_1 \sqrt{gh}\,h}{-C^2 \alpha_{cu} d} \dfrac{1}{\sqrt{gh}} = + \left(\dfrac{C^*}{C}\right)^2 \dfrac{h}{d} \dfrac{E_1}{\alpha_{cu}} \\
2. \\
\alpha_{cu} U \dfrac{1}{\sqrt{gh}} = \alpha_{cu} F_r \\
3. \\
\alpha_{cu} C \dfrac{C^* E_1 \sqrt{gh}\,h}{-C^2 \alpha_{cu} d} \dfrac{1}{\sqrt{gh}} = - \left(\dfrac{C^*}{C}\right) E_1 \dfrac{h}{d} \\
4. and 5. \\
See \quad A_{21} \qquad and \quad A_{21} \\
6. \\
\alpha_{cu} h C C^* \dfrac{C^* E_1 \sqrt{gh}\,h}{-C^2 \alpha_{cu} d} \dfrac{1}{\sqrt{gh}\,h} = -E_1 \left(\dfrac{C^{*2}}{C}\right) \dfrac{h}{d} \\
7. \\
\alpha_{cu} U h C^* \dfrac{1}{\sqrt{gh}\,h} = \alpha_{cu} C^* F_r \\
8. \\
-\alpha_{cu}^2 U h C \dfrac{1}{\sqrt{gh}\,h} = -\alpha_{cu}^2 C\, F_r \\
9. \\
-\alpha_{cu}^2 U^2 h \left(-\dfrac{C^2}{C^*} \dfrac{\alpha_{cu}}{E_1} \dfrac{1}{\sqrt{gh}} \dfrac{d}{h}\right) \dfrac{1}{\sqrt{gh}\,h} = + \dfrac{\alpha_{cu}^3}{E_1} \dfrac{C^2}{C^*} \dfrac{d}{h} F_r^2 \\
10. \\
-\alpha_{cu}^2 C^2 h \dfrac{1}{\left(-\frac{C^2}{C^*} \frac{\alpha_{cu}}{E_1} \frac{1}{\sqrt{gh}} \frac{d}{h}\right)} \dfrac{1}{\sqrt{gh}\,h} = + \alpha_{cu}\, E_1\, C^* \dfrac{h}{d} \\
11. \\
-\alpha_{cu}^2 U h C \dfrac{1}{\sqrt{gh}\,h} = -\alpha_{cu}^2 C\, F_r \\
12. \\
2 C h U \beta_2 \dfrac{1}{\sqrt{gh}\,h} = 2 \beta_2 C F_r
\end{cases}
\tag{A.1.37}
$$

$$\begin{cases} 13. \\ U^2 h \beta_2 \left(-\dfrac{C^2}{C^*} \dfrac{\alpha_{cu}}{E_1} \dfrac{1}{\sqrt{gh}} \dfrac{d}{h} \right) \dfrac{1}{\sqrt{gh}\, h} = -\dfrac{\beta_2 \alpha_{cu}}{E_1} \dfrac{C^2}{C^*} \dfrac{d}{h} F_r^2 \\ 14. \\ \dfrac{gh^2}{2} \left(-\dfrac{C^2}{C^*} \dfrac{\alpha_{cu}}{E_1} \dfrac{1}{\sqrt{gh}} \dfrac{d}{h} \right) \dfrac{1}{\sqrt{gh}\, h} = -\dfrac{\alpha_{cu}}{2\, E_1} \dfrac{C^2}{C^*} \dfrac{d}{h} \end{cases} \tag{A.1.38}$$

By summing all the terms:

$$\begin{aligned} A_{22} = &+ \left(\frac{C^*}{C} \right)^2 \frac{h}{d} \frac{E_1}{\alpha_{cu}} + \alpha_{cu} F_r - \left(\frac{C^*}{C} \right) E_1 \frac{h}{d} + \\ &- \frac{1}{\tilde{C}_h} \left(\frac{E_1}{\alpha_{cu}} \frac{h}{d} \frac{C^*}{C} \left(\frac{C^*}{C} - 1 \right) - 1.5 F_r \right) \Bigg[- E_1 \left(\frac{C^{*2}}{C} \right) \frac{h}{d} + \\ &+ \alpha_{cu} C^* F_r - \alpha_{cu}^2 C\, F_r + \frac{\alpha_{cu}^3}{E_1} \frac{C^2}{C^*} \frac{d}{h} F_r^2 + \alpha_{cu}\, E_1\, C^* \frac{h}{d} + \\ &- \alpha_{cu}^2 C\, F_r + 2 \beta_2 C F_r - \frac{\beta_2 \alpha_{cu}}{E_1} \frac{C^2}{C^*} \frac{d}{h} F_r^2 - \frac{\alpha_{cu}}{2\, E_1} \frac{C^2}{C^*} \frac{d}{h} \Bigg] \end{aligned} \tag{A.1.39}$$

Finally:

$$\begin{aligned} A_{22} = &\left(\frac{C^*}{C} \right) E_1 \frac{h}{d} \left(\frac{1}{\alpha_{cu}} \frac{C^*}{C} - 1 \right) + \alpha_{cu} F_r + \\ &- \frac{1}{\tilde{C}_h} \left(\frac{E_1}{\alpha_{cu}} \frac{h}{d} \frac{C^*}{C} \left(\frac{C^*}{C} - 1 \right) - 1.5 F_r \right) \Bigg[F_r (\alpha_{cu} C^* + \\ &- 2 \alpha_{cu}^2 C + 2 \beta_2 C) + F_r^2 \frac{\alpha_{cu}}{E_1} \frac{C^2}{C^*} \frac{d}{h} (\alpha_{cu}^2 - \beta_2) + \\ &+ E_1\, C^* \frac{h}{d} \left(\alpha_{cu} - \frac{C^*}{C} - \frac{\alpha_{cu}}{2\, E_1^2} \left(\frac{C}{C^*} \right)^2 \left(\frac{d}{h} \right)^2 \right) \Bigg] \end{aligned} \tag{A.1.40}$$

Finally the last term of the second equation: A_{23}. It is made dimension-

less dividing by $g\sqrt{gh}$.

$$\begin{cases} 1. \\ -gC(C-C^*)\dfrac{C^*E_1\sqrt{gh}\,h}{-C^2\alpha_{cu}d}\dfrac{1}{g\sqrt{gh}} = +\dfrac{E_1}{\alpha_{cu}}\dfrac{h}{d}\dfrac{C^*}{C}(C-C^*) \\ 2. \\ -gCh\left(-\dfrac{3}{2}\dfrac{U}{h}\right)\dfrac{1}{g\sqrt{gh}} = \dfrac{3}{2}C\,F_r \end{cases} \tag{A.1.41}$$

So finally:

$$A_{23} = \frac{1}{\tilde{C}_h}\left[\frac{E_1}{\alpha_{cu}}\frac{h}{d}\frac{C^*}{C}(C-C^*) + \frac{3}{2}C\,F_r\right] \tag{A.1.42}$$

Now the last 3 coefficients. The first one A_{31} is made dimensionless dividing by $\sqrt{gh}$ all the terms except for the last one (which is not

divided by C_h) that should be divided by $\sqrt{gh}$.

$$
\begin{cases}
1. \\
\alpha_{cu} U^2 C^* \dfrac{1}{gh} = \alpha_{cu} F_r^2 C^* \\
2. \\
\alpha_{cu} U C C^* \dfrac{C^* E_1 \sqrt{gh}\, h}{-C^2 \alpha_{cu} d} \dfrac{1}{gh} = -E_1 \left(\dfrac{C^{*2}}{C} \right) \dfrac{h}{d} F_r \\
3. \\
-\alpha_{cu}^2 U C^2 \dfrac{C^* E_1 \sqrt{gh}\, h}{-C^2 \alpha_{cu} d} \dfrac{1}{gh} = +\alpha_{cu} E_1\, C^* \dfrac{h}{d} F_r \\
4. \\
-\alpha_{cu}^2 U^2 C \dfrac{1}{gh} = -\alpha_{cu}^2\, C\, F_r^2 \\
5. \\
-\alpha_{cu}^2 C U h \left(-\dfrac{3}{2} \dfrac{U}{h} \right) \dfrac{1}{gh} = 1.5 \alpha_{cu}^2 C\, F_r^2 \\
6. \\
-\alpha_{cu}^2 U^2 h\, 1.5 \dfrac{C^2}{C^*} \dfrac{\alpha_{cu}}{E_1\, h} \dfrac{d}{h} \dfrac{U}{\sqrt{gh}} \dfrac{1}{gh} = -\dfrac{1.5\, \alpha_{cu}^3}{E_1} \left(\dfrac{C^2}{C^*} \right) \dfrac{d}{h} F_r^3 \\
7. \\
\beta_2 U^2 C \dfrac{1}{gh} = \beta_2\, C\, F_r^2 \\
8. \\
\beta_2 h U^2\, 1.5 \dfrac{C^2}{C^*} \dfrac{\alpha_{cu}}{E_1\, h} \dfrac{d}{h} \dfrac{U}{\sqrt{gh}} \dfrac{1}{gh} = \dfrac{1.5\, \beta_2 \alpha_{cu}}{E_1} \left(\dfrac{C^2}{C^*} \right) \dfrac{d}{h} F_r^3 \\
9. \\
\dfrac{gh^2}{2}\, 1.5 \dfrac{C^2}{C^*} \dfrac{\alpha_{cu}}{E_1\, h} \dfrac{d}{h} \dfrac{U}{\sqrt{gh}} \dfrac{1}{gh} = \dfrac{3}{4} \dfrac{\alpha_{cu}}{E_1} \left(\dfrac{C^2}{C^*} \right) \dfrac{d}{h} F_r \\
10. \\
gCh \dfrac{1}{gh} = C \\
11. \\
U \dfrac{1}{\sqrt{gh}} = F_r
\end{cases}
\tag{A.1.43}
$$

Finally we obtain:

$$A_{31} = -\frac{1}{\tilde{C}_h}\left[\alpha_{cu}F_r^2C^* - E_1\left(\frac{C^{*2}}{C}\right)\frac{h}{d}F_r + \alpha_{cu}E_1\,C^*\frac{h}{d}F_r + \right.$$
$$- \alpha_{cu}^2\,C\,F_r^2 + 1.5\alpha_{cu}^2 C\,F_r^2 - \frac{1.5\,\alpha_{cu}^3}{E_1}\left(\frac{C^2}{C^*}\right)\frac{d}{h}F_r^3 + \beta_2\,C\,F_r^2 +$$
$$\left. + \frac{1.5\,\beta_2\alpha_{cu}}{E_1}\left(\frac{C^2}{C^*}\right)\frac{d}{h}F_r^3 + \frac{3}{4}\frac{\alpha_{cu}}{E_1}\left(\frac{C^2}{C^*}\right)\frac{d}{h}F_r + C\right] + F_r \tag{A.1.44}$$

$$A_{31} = -\frac{1}{\tilde{C}_h}\left[E_1\,C^*\frac{h}{d}F_r\left(\alpha_{cu} - \frac{C^*}{C} + \frac{3}{4}\frac{\alpha_{cu}}{E_1^2}\left(\frac{C^2}{C^*}\right)^2\left(\frac{d}{h}\right)^2\right) + \right.$$
$$+ F_r^2(\alpha_{cu}C^* + C(\beta_2 + \alpha_{cu}^2/2)) + F_r^3\frac{3}{2}\frac{\alpha_{cu}}{E_1}\left(\frac{C^2}{C^*}\right)\frac{d}{h}(\beta_2 - \alpha_{cu}^2) +$$
$$\left. + C\right] + F_r \tag{A.1.45}$$

The second term is A_{32}. It is split into 10 sub-terms, each made dimensionless through $\sqrt{ghh}$, except for the last which is divided by h.

$$
\begin{cases}
1. \\
\alpha_{cu} C C^* h \dfrac{C^* E_1 \sqrt{gh}\, h}{-C^2 \alpha_{cu} d} \dfrac{1}{\sqrt{gh}\, h} = -E_1 \left(\dfrac{C^{*2}}{C} \right) \dfrac{h}{d} \\
2. \\
\alpha_{cu} U h C^* \dfrac{1}{\sqrt{gh}\, h} = \alpha_{cu} C^* F_r \\
3. \\
-\alpha_{cu}^2 U h C \dfrac{1}{\sqrt{gh}\, h} = -\alpha_{cu}^2 C F_r \\
\\
4. \\
-\alpha_{cu}^2 U^2 h \dfrac{1}{\frac{C^* E_1 \sqrt{gh}\, h}{-C^2 \alpha_{cu} d}} \dfrac{1}{\sqrt{gh}\, h} = + \dfrac{\alpha_{cu}^3}{E_1} \dfrac{C^2}{C^*} \dfrac{d}{h} F_r^2 \\
5. \\
-\alpha_{cu} h C^2 \dfrac{C^* E_1 \sqrt{gh}\, h}{-C^2 \alpha_{cu} d} \dfrac{1}{\sqrt{gh}\, h} = C^* E_1 \dfrac{h}{d} \\
6. \\
-\alpha_{cu}^2 C U h \dfrac{1}{\sqrt{gh}\, h} = -\alpha_{cu}^2 C F_r \\
7. \\
2\beta_2 U h C \dfrac{1}{\sqrt{gh}\, h} = 2\beta_2\, C\, F_r \\
8. \\
\beta_2 U^2 h \dfrac{1}{\frac{C^* E_1 \sqrt{gh}\, h}{-C^2 \alpha_{cu} d}} \dfrac{1}{\sqrt{gh}\, h} = -\dfrac{\beta_2 \alpha_{cu}}{E_1} \dfrac{C^2}{C^*} \dfrac{d}{h} F_r^2 \\
9. \\
\dfrac{gh^2}{2} \dfrac{1}{\frac{C^* E_1 \sqrt{gh}\, h}{-C^2 \alpha_{cu} d}} \dfrac{1}{\sqrt{gh}\, h} = -\dfrac{\alpha_{cu}}{2E_1} \dfrac{C^2}{C^*} \dfrac{d}{h} \\
10. \\
h \dfrac{1}{h} = 1
\end{cases}
\tag{A.1.46}
$$

Finally we sum up the terms:

$$A_{32} = -\frac{1}{\tilde{C}_h}\Bigg[-E_1\left(\frac{C^{*2}}{C}\right)\frac{h}{d} + \alpha_{cu}C^*F_r - \alpha_{cu}^2 CF_r + \frac{\alpha_{cu}^3}{E_1}\frac{C^2}{C^*}\frac{d}{h}F_r^2 + \\ + C^*E_1\frac{h}{d} - \alpha_{cu}^2 CF_r + 2\beta_2\, C\, F_r - \frac{\beta_2\alpha_{cu}}{E_1}\frac{C^2}{C^*}\frac{d}{h}F_r^2 - \frac{\alpha_{cu}}{2E_1}\frac{C^2}{C^*}\frac{d}{h}\Bigg] + \\ + 1 \tag{A.1.47}$$

And:

$$A_{32} = -\frac{1}{\tilde{C}_h}\Bigg[F_r(\alpha_{cu}C^* + 2C(\beta_2 - \alpha_{cu}^2)) + F_r^2\frac{\alpha_{cu}}{E_1}\frac{C^2}{C^*}\frac{d}{h}(\alpha_{cu}^2 - \beta_2) + \\ + C^*E_1\frac{h}{d}\left(1 - \frac{C^*}{C} - \frac{\alpha_{cu}}{2E_1^2}\left(\frac{C^2}{C^*}\right)^2\left(\frac{d}{h}\right)^2\right)\Bigg] + 1 \tag{A.1.48}$$

The last term A_{33} is the following:

$$A_{33} = -\frac{1}{\tilde{C}_h}\frac{hgC}{hg} = -\frac{C}{\tilde{C}_h} \tag{A.1.49}$$

Bibliography

Aguirre, M. A., De Schant, R., and Géminard, J.-C. (2014). Granular flow through an aperture: influence of the packing fraction. *Physical Review E*, 90(1):012203.

Ancey, C. and Evesque, P. (2000). Frictional-collisional regime for granular suspension flows down an inclined channel. *Physical Review E*, 62(6):8349.

Andrianov, N. and Warnecke, G. (2004). The riemann problem for the baer-nunziato two-phase flow model. *Journal of Computational Physics*, 212:434–464.

Aranson, I. S. and Tsimring, L. S. (2002). Continuum theory of partially fluidized granular flows. *Physical Review E*, 65(6):061303.

Armanini, A. (2015). Closure relations for mobile bed debris flows in a wide range of slopes and concentrations. *Advances in Water Resources*, 81:75–83.

Armanini, A., Capart, H., Fraccarollo, L., and Larcher, M. (2005). Rheological stratification in experimental free-surface flows of granular–liquid mixtures. *Journal of Fluid Mechanics*, 532:269–319.

Armanini, A., Larcher, M., and Fraccarollo, L. (2009). Intermittency of rheological regimes in uniform liquid-granular flows. *Physical Review E*, 79(5):051306.

Armanini, A., Larcher, M., Nucci, E., and Dumbser, M. (2014). Submerged granular channel flows driven by gravity. *Advances in Water Resources*, 63:1–10.

Avesani, D., Dumbser, M., and Bellin, A. (2014). A new class of moving-least-squares weno-sph schemes. *J. Comput. Phys.*, 270(0):278–299.

B. Ben Moussa, N. L. and Vila, J. (1999). Convergence of meshless methods for conservation laws: applications to euler equations. *Int. Ser. Numer. Math.*, 129:31–40.

Baer, M. and Nunziato, J. (1986). A two-phase mixture theory for the deflagration-to-detonation transition (DDT) in reactive granular materials. *J. Multiphase Flow*, 12:861–889.

Bagnold, R. A. (1954). Experiments on a gravity-free dispersion of large solid spheres in a newtonian fluid under shear. In *Proceedings of the Royal Society of London A: Mathematical, Physical and Engineering Sciences*, volume 225, pages 49–63. The Royal Society.

Bartelt, P., Salm, B., and Gruber, U. (1999). Calculating dense-snow avalanche runout using a voellmy-fluid model with active/passive longitudinal straining. *Journal of Glaciology*, 45(150):242–254.

Bermudez, A. and Vázquez-Cendón, M. (1994). Upwind methods for hyperbolic conservation laws with source terms. *Computers and Fluids*, 23:1049–1071.

Bouguet, J.-Y. (2001). Pyramidal implementation of the affine lucas kanade feature tracker description of the algorithm. *Intel Corporation*, 5(1-10):4.

Brockbank, R., Huntley, J., and Ball, R. (1997). Contact force distribution beneath a three-dimensional granular pile. *Journal de Physique II*, 7(10):1521–1532.

Buades, A., Coll, B., and Morel, J.-M. (2011). Non-local means denoising. *Image Processing On Line*, 1:208–212.

Buser, O. and Bartelt, P. (2009). Production and decay of random kinetic energy in granular snow avalanches. *Journal of Glaciology*, 55(189):3–12.

Campbell, C. S. (1990). Rapid granular flows. *Annual Review of Fluid Mechanics*, 22(1):57–90.

Campbell, J. (2000). A contact algorithm for smoothed particle hydrodynamics. *Comput. Methods Appl. Mech. Engrg.*, 184:49–65.

Canestrelli, A., Dumbser, M., Siviglia, A., and Toro, E. (2010). Well-balanced high-order centered schemes on unstructured meshes for shallow water equations with fixed and mobile bed. *Advances in Water Resources*, 33:291–303.

Castro, M., Gallardo, J., and Parés, C. (2006). High-order finite volume schemes based on reconstruction of states for solving hyperbolic systems with nonconservative products. applications to shallow-water systems. *Mathematics of Computation*, 75:1103–1134.

Chapman, S. and Cowling, T. G. (1970). *The mathematical theory of non-uniform gases: an account of the kinetic theory of viscosity, thermal conduction and diffusion in gases*. Cambridge university press.

Christen, M., Bartelt, P., and Gruber, U. (2002). Aval-1d: An avalanche dynamics program for the practice. In *International congress interpraevent*, pages 715–725.

Christen, M., Kowalski, J., and Bartelt, P. (2010). Ramms: Numerical simulation of dense snow avalanches in three-dimensional terrain. *Cold Regions Science and Technology*, 63(1):1–14.

Colagrossi, A. and Landrini, M. (2003). Numerical simulation of interfacial flows by smoothed particle hydrodynamics. *J. Comput. Phys.*, 191:448–475.

Cummins, S. and Rudman., M. (1999). An sph projection method. *J. Comput. Phys.*, 152:584–607.

Dantu, P. (1968). Etude statistique des forces intergranulaires dans un milieu pulvérulent. *Géotechnique*, 18(1):50–55.

Deledicque, V. and Papalexandris, M. (2007). An exact riemann solver for compressible two-phase flow models containing non-conservative products. *Journal of Computational Physics*, 222:217–245.

Drew, D. (1983). Mathematical modelling of two-phase flow. *Annual Review of Fluid Mechanics*, 15:261–291.

Dumbser, M. and Balsara, D. (2016). A new, efficient formulation of the HLLEM Riemann solver for general conservative and non-conservative hyperbolic systems. *Journal of Computational Physics*, 304:275–319.

Dumbser, M., Hidalgo, A., Castro, M., Parés, C., and Toro, E. (2010). FORCE schemes on unstructured meshes II: Non–conservative hyperbolic systems. *Computer Methods in Applied Mechanics and Engineering*, 199:625–647.

Dumbser, M. and Toro, E. F. (2011a). On universal Osher–type schemes for general nonlinear hyperbolic conservation laws. *Communications in Computational Physics*, 10:635–671.

Dumbser, M. and Toro, E. F. (2011b). A simple extension of the Osher Riemann solver to non-conservative hyperbolic systems. *Journal of Scientific Computing*, 48:70–88.

E.F.Toro (2001). Shock-capturing methods for free-surface shallow flows. *John Wiley & Sons*.

Eglit, M. (1998). Mathematical and physical modelling of powder snow avalanches in russia. *Annals of Glaciology*, 26:281–284.

Einfeldt, B. (2001). On godunov-type methods for gas dynamics. *J. Plasma Phys.*, 65:29–58.

Einfeldt, B., Munz, C. D., Roe, P. L., and Sjögreen, B. (1991). On godunov-type methods near low densities. *Journal of Computational Physics*, 92:273–295.

Favre, A. (1965). *The quations of compressible turbulent gases*. Aix-Marseille Universite, Institute de Mecanique Statistique de la Turbulence, Marseille, France.

Ferrari, A., Dumbser, M., Toro, E., and Armanini, A. (2009). A new 3d parallel sph scheme for free surface flows. *Computers and Fluids*, 38(6):1203–1217.

Gingold, R. and Monaghan, J. (1977). Smooth particle hydrodynamics:theory and application to non-spherical stars. *Mon. Not. R. Astr. Soc.*, 181:375–389.

Goldhirsch, I. (2003). Rapid granular flow. *Annual Review of Fluid Mechanics*, 35:267–293.

Goldhirsch, I. (2008). Introduction to granular temperature. *Powder Technology*, 182:130–136.

H.A. Posch, W. H. and Kum, O. (1995). Steady-state shear flows via non-equilibrium molecular dynamics and smooth-particle applied mechanics. *Phys. Rev. E.*, 52:1711–1719.

Huang, K. (1928). *Statistical Mechanics*. Ed: John Wiley & Sons., Massachussetts Institute of Technology.

Issler, D. (1998). Modelling of snow entrainment and deposition in powder-snow avalanches. *Annals of Glaciology*, 26:253–258.

Jaeger, H. M., Nagel, S. R., and Behringer, R. P. (1996). Granular solids, liquids, and gases. *Reviews of modern physics*, 68(4):1259.

Jansen, P. P., Van Bendegom, L., Van den Berg, J., De Vries, M., and Zanen, A. (1994). Principles of river engineering: The non-tidal alluvial river.

Jenkins, J. and Mancini, F. (1987). Balance laws and constitutive relations for plane flows of a dense, binary mixture of smooth, nearly elastic, circular disks. *Journal of Applied Mechanics*, 54(1):27–34.

Jenkins, J. and Richman, M. (1985). Kinetic theory for plane flows of a dense gas of identical, rough, inelastic, circular disks. *Physics Fluids*, 28:3485–94.

Jenkins, J. and Richman, M. (1986). Boundary conditions for plane flows of smooth, nearly elastic, circular disks. *Journal of Fluid Mechanics*, 171:53–69.

Jenkins, J. T. (2007). Dense inclined flows of inelastic spheres. *Granular matter*, 10(1):47–52.

Jenkins, J. T. and Hanes, D. M. (1998). Collisional sheet flows of sediment driven by a turbulent fluid. *Journal of Fluid Mechanics*, 370:29–52.

Jenkins, J. T. and Savage, S. B. (1983). A theory for the rapid flow of identical, smooth, nearly elastic, spherical particles. *Journal of fluid mechanics*, 130:187–202.

Jop, P. (2008). Hydrodynamic modeling of granular flows in a modified couette cell. *Physical Review E*, 77(3):032301.

Jop, P., Forterre, Y., and Pouliquen, O. (2006). A constitutive law for dense granular flows. *arXiv preprint cond-mat/0612110*.

J.P. Morris, P. F. and Zhu, Y. (1997). Modeling low reynolds number incompressible flows using sph. *J. Comput. Phys.*, 136:214–226.

LeVeque, R. J. (1998). Balancing source terms and flux gradients in high-resolution godunov methods: The quasi-steady wavepropagation algorithm. *Journal of Computational Physics*, 146:346–365.

Lois, G., Lemaitre, A., and Carlson, J. (2006). Emergence of multicontact interactions in contact dynamics simulations of granular shear flows. *EPL (Europhysics Letters)*, 76(2):318.

Lucy, L. (1977). A numerical approach to the testing of the fission hypothesis. *Astr. J.*, 82:1013–1024.

Lun, C. (1991). Kinetic theory for granular flow of dense, slightly inelastic, slightly rough spheres. *Journal of Fluid Mechanics*, 233:539–559.

Lun, C. and Savage, S. (1986). The effects of an impact velocity dependent coefficient of restitution on stresses developed by sheared granular materials. *Acta Mechanica*, 63(1-4):15–44.

Lun, C. and Savage, S. (1987). A simple kinetic theory for granular flow of rough, inelastic, spherical particles. *J. Appl. Mech*, 54(1):47–53.

Lun, C., Savage, S. B., Jeffrey, D., and Chepurniy, N. (1984). Kinetic theories for granular flow: inelastic particles in couette flow and slightly inelastic particles in a general flowfield. *Journal of fluid mechanics*, 140:223–256.

Maso, G. D., LeFloch, P., and Murat, F. (1995). Definition and weak stability of nonconservative products. *J. Math. Pures Appl.*, 74:483–548.

Meninno, S. (2015). *Mechanics of dry granular flows driven by gravity*. Phd thesis, University of Trento.

Meninno, S., Armanini, A., and Larcher, M. (2018). Gravity-driven, dry granular flows over a loose bed in stationary and homogeneous conditions. *Phys. Rev. Fluids*, 3:024301.

Meyer, F. (1992). Color image segmentation. In *Image Processing and its Applications, 1992., International Conference on*, pages 303–306. IET.

MiDi, G. (2004). On dense granular flows. *European Physical Journal E–Soft Matter*, 14(4).

Mitarai, N. and Nakanishi, H. (2004). Density profile of dense granular flow down a rough slope. *Phys. Rev. Lett.*, 94(cond-mat/0407651):128001.

Monaghan, J. (1994). Simulating free surface flows with sph. *J. Comput. Phys.*, 110:399–406.

Monaghan, J. (2000). Sph without a tensile instability. *J. Comput. Phys.*, 159:290–311.

Monaghan, J. (2005). Smoothed particle hydrodynamics. *Rep Progr Phys*, 68:1703–1759.

Monaghan, J. and Gingold, R. (1983). Shock simulation by the particle method sph. *J. Comput. Phys.*, 52:374–389.

Monaghan, J. and Gingold, R. (1989). On the problem of penetration in particle methods. *J. Comput. Phys.*, 82:1–15.

Monaghan, J. and Kocharyan, A. (1995). Sph simulation of multiphase flow. *Comput. Phys. Commun.*, 87:225–235.

Moussa, B. B. (2006). On the convergence of sph method for scalar conservation laws with boundary conditions. *Methos Appl. Analysis*, 13:29–62.

Muñoz, M. and Parés, C. (2007). Godunov method for nonconservative hyperbolic systems. *Mathematical Modelling and Numerical Analysis*, 41:169–185.

Noelle, S., Pankratz, N., Puppo, G., and Natvig, J. (2006). Well-balanced finite volume schemes of arbitrary order of accuracy for shallow water flows. *Journal of Computational Physics*, 213:474–499.

Norem, H., Irgens, F., and Schieldrop, B. (1987). A continuum model for calculating snow avalanche velocities. *IAHS Publ*, 162:363–379.

Norem, H., Irgens, F., and Schieldrop, B. (1989). Simulation of snow-avalanche flow in run-out zones. *Annals of Glaciology*, 13:218–225.

O. Kum, W. H. and Posch, H. (2007). Viscous conducting flows with smooth-particle applied mechanics. *Comput. Geosci.*, 11:297–306.

Otsu, N. (1979). A threshold selection method from gray-level histograms. *IEEE transactions on systems, man, and cybernetics*, 9(1):62–66.

Parés, C. (2006). Numerical methods for nonconservative hyperbolic systems: a theoretical framework. *SIAM Journal on Numerical Analysis*, 44:300–321.

Pelanti, M., Bouchut, F., and Mangeney, A. (2008). A Roe-Type scheme for two-phase shallow granular flows over variable topography. *Mathematical Modelling and Numerical Analysis*, 42:851–885.

Pitman, E. and Le, L. (2005a). A two-fluid model for avalanche and debris flows. *Phil. Trans. R. Soc. A*, 363:1573–1601.

Pitman, E. B. and Le, L. (2005b). A two-fluid model for avalanche and debris flows. *Philosophical Transactions of the Royal Society of London A: Mathematical, Physical and Engineering Sciences*, 363(1832):1573–1601.

Pizer, S. M., Amburn, E. P., Austin, J. D., Cromartie, R., Geselowitz, A., Greer, T., ter Haar Romeny, B., Zimmerman, J. B., and Zuiderveld, K. (1987). Adaptive histogram equalization and its variations. *Computer vision, graphics, and image processing*, 39(3):355–368.

Plimpton, S. (1995). Fast parallel algorithms for short-range molecular dynamics. *Journal of computational physics*, 117(1):1–19.

Pudasaini, S. P. (2012). A general two-phase debris flow model. *Journal of Geophysical Research: Earth Surface*, 117(F3).

R. Bernetti, V. T. and Toro., E. (2008). Exact solution of the riemann problemfor the shallow water equations with discontinuous bottom geometry. *Journal of Computational Physics*, 227:3212–3243.

Reif, F. (1965). *Statistical thermal physics*. Mcgraw-Hill Kogakusha.

Roux, S. and Radjai, F. (1998). Texture-dependent rigid-plastic behavior. In *Physics of dry granular media*, pages 229–236. Springer.

Rusanov, V. V. (1961). Calculation of Interaction of Non–Steady Shock Waves with Obstacles. *J. Comput. Math. Phys. USSR*, 1:267–279.

Salm, B. (1966). Contribution to avalanche dynamics. *IASH-AIHS Pub.*, 69:199–214.

Salm, B. (1967). *On nonuniform, steady flow of avalanching snow*. Ceuterick.

Sartoris, G. and Bartelt, P. (2000). Upwinded finite difference schemes for dense snow avalanche modeling. *International Journal for Numerical Methods in Fluids*, 32(7):799–821.

Savage, S. and Hutter, K. (1991). The dynamics of avalanches of granular materials from initiation to runout. part i: Analysis. *Acta Mechanica*, 86(1):201–223.

Savage, S. and Jeffrey, D. (1981). The stress tensor in a granular flow at high shear rates. *Journal of Fluid Mechanics*, 110:255–272.

Savage, S. B. (1984). The mechanics of rapid granular flows. *Advances in applied mechanics*, 24:289–366.

Savage, S. B. and Hutter, K. (1989). The motion of a finite mass of granular material down a rough incline. *Journal of fluid mechanics*, 199:177–215.

Schwendeman, D., Wahle, C., and Kapila, A. (2006). The riemann problem and a high-resolution godunov method for a model of compressible two-phase flow. *Journal of Computational Physics*, 212:490–526.

Shen, H. H. (1984). Stresses in a rapid flow of spherical solid with two sizes. *Particulate Science and Technology*, 2(1):37–56.

Shen, H. H. and Hopkins, M. A. (1988). Stresses in a rapid, simple shear flow of granular materials with multiple grain sizes. *Particulate science and technology*, 6(1):1–15.

Shi, J. et al. (1994). Good features to track. In *Computer Vision and Pattern Recognition, 1994. Proceedings CVPR'94., 1994 IEEE Computer Society Conference on*, pages 593–600. IEEE.

Taberlet, N., Richard, P., Valance, A., Losert, W., Pasini, J. M., Jenkins, J. T., and Delannay, R. (2003). Superstable granular heap in a thin channel. *Physical review letters*, 91(26):264301.

Tavelli, M. and Dumbser, M. (2014). A high order semi-implicit discontinuous Galerkin method for the two dimensional shallow water equations on staggered unstructured meshes. *Applied Mathematics and Computation*, 234:623–644.

To, K., Lai, P.-Y., and Pak, H. (2001). Jamming of granular flow in a two-dimensional hopper. *Physical review letters*, 86(1):71.

Tomasi, C. and Manduchi, R. (1998). Bilateral filtering for gray and color images. In *Computer Vision, 1998. Sixth International Conference on*, pages 839–846. IEEE.

Toro, E. (1999). *Riemann Solvers and Numerical Methods for Fluid Dynamics*. Springer, second edition.

Vanel, L., Howell, D., Clark, D., Behringer, R., and Clément, E. (1999). Memories in sand: Experimental tests of construction history on stress distributions under sandpiles. *Physical Review E*, 60(5):R5040.

Vázquez-Cendón, M. (1999). Improved treatment of source terms in upwind schemes for the shallow water equations in channels with irregular geometry. *Journal of Computational Physics*, 148:497–526.

Vila, J. (1999). On particle weighted methods and smooth particle hydrodynamics. *Math. Models Methods Appl. Sci.*, 9:161–209.

Voellmy, A. (1955). Ueber die zerstoeerunskraft von lawinen schweizerische bauzeitung. english version "on the destructive force of avalanches" translated by tate re (1964), ed. *US Department of Agriculture Forest Service. Cerca con Google*.

Welton, W. (1997). Two-dimensional pdf/sph simulations of compressible turbulent flows. *J. Comput. Phys.*, 134:150–168.

Xing, Y. and Shu, C. (2006). High-order well-balanced finite difference WENO schemes for a class of hyperbolic systems with source terms. *Journal of Scientific Computing*, 27:477–494.